

**IN-SITU ENERGY DISPERSIVE X-RAY DIFFRACTION STUDY OF
PRESSURE AND ELECTRIC FIELD EFFECTS IN THE DENSIFICATION
OF
CERAMIC OXIDE NANOPARTICLES**

By

Ilyas Savkliydiz

A Dissertation submitted to the
Graduate School-New Brunswick
Rutgers, The State University of New Jersey

In partial fulfillment of the requirements

For the degree of

Doctor of Philosophy

Graduate Program in Materials Science and Engineering

Written under the direction of

Professor Thomas Tsakalakos

And approved by

New Brunswick, New Jersey

May, 2015

ABSTRACT OF THE DISSERTATION
IN-SITU ENERGY DISPERSIVE X-RAY DIFFRACTION STUDY OF
PRESSURE AND ELECTRIC FIELD EFFECTS IN THE DENSIFICATION
OF
CERAMIC OXIDE NANOPARTICLES

By Ilyas Savkliyildiz

Dissertation Advisor: Prof. Thomas Tsakalakos

Dissertation Co-Advisor: Dr. Enver K. Akdoğan

Of current interest are dense polycrystalline ceramics with <100 nm grain size. The densification of such ceramics requires additional driving forces such as pressure or electricity to suppress grain growth while promoting high density. In this study, we use a ultrahigh energy polychromatic synchrotron radiation with superb temporal resolution to study the time evolution of prototype multicomponent ceramic oxide as a function of hydrostatic pressure and electric field.

Firstly, we study the temperature and pressure dependence of phase evolution in 0.5MgO-0.5Y₂O₃ and 0.8MgO-0.2Y₂O₃ IR nanocomposites using a diamond anvil apparatus in conjunction with in situ synchrotron energy dispersive x-ray diffraction at 1000 °C with 5.5-7.0 GPa hydrostatic pressure . Isothermal and isobaric hold at (1273 K, 5.5-7 GPa) for 60 min, the macroscopic shrinkage due to densification is 3% by volume which endorses densification. Furthermore, volumetric expansion around 1%, on MgO site is observed due to Y₂O₃ dissolving in cubic MgO despite the large differences in the ionic radii of the cations during isobaric and isothermal hold. The release of pressure at room temperature preserves the MgO lattice expansion and results in a metastable

composite the cubic phase of MgO, and the cubic, hexagonal and monoclinic phases of Y_2O_3 . Aging up to 240 h did not destroy the 4-phase co-existence. A crystallographic model is proposed due to observed volumetric expansion of the MgO unit cell based on Coulomb repulsion among O^{2-} ions in the vicinity of Mg^{+2} vacancies, and misfit strain due to differences in ionic radii. Secondly, we study the densification of 8% yttria doped zirconia (8YSZ) under superimposed thermal and electric field using time-resolved in-situ high temperature EDXRD method with a polychromatic 200 keV synchrotron probe as a function of applied electric field. Nonisothermal densification occurred in the 790–930 °C range with 3 Amps maximum current draw, resulting in 95-98 % density. No local melting at particle-particle contacts was observed in pertaining electron microscopy analysis. The onset of densification scales inversely with the applied field. Densification is accompanied by transients of high current draw, anomalous anelastic volume expansion ranging from 1% to 3%. No phase transformations are observed. We attribute the reduction in densification temperature and time to ultrafast ambipolar diffusion of species arising from the superposition of mass fluxes due to Fickian diffusion, thermodiffusion (Soret effect), and electromigration, which in turn are a consequence of a superposition of chemical, temperature, and electrical potential gradients. This densification mode is named field assisted sintering or “burst-mode” due to its discontinuous nature.

Acknowledgments

This Scientific research was made feasible through the guidance and direction accommodated by my advisor Prof. Thomas Tsakalakos and co-advisor Dr. Koray Akdogan. I would like to thank Prof. Lisa Klein and Dr. Nicholas Simos for contribution to this research through their valuable experience. I would like to extend my appreciation to Turkish Ministry of Education, which make possible this scientific research by covering whole my graduation education expenses. I would like express my appreciation to my group members for their technical support.

I would like to acknowledge my family for their love, encouragement, motivation, and most of all, for their patience during my graduate education;

My Mother, Emine; My Father, Mehmet; My sister, Seher; My brother, Salih.

Table of Contents

ABSTRACT OF THE DISSERTATION	ii
Acknowledgements	iv
Table of Contents	v
List of Tables	vii
List of Figures	viii
1. Introduction	1
2. Scientific Background and Systems of Interest.....	3
2.1. High Pressure Sintering	3
2.2. The MgO-Y ₂ O ₃ Nano Composite System	4
2.2.1. Optical Properties of Multiphase MgO-Y ₂ O ₃ Composites	6
2.2.2. Grain Size Effect on Phase Transition	8
2.2.3. Solid Solubility and Grain Growth in Composite Systems.....	8
2.3. Electric Field Assisted Sintering	9
2.3.1. Flash Sintering	11
2.4. The 8% Y ₂ O ₃ - ZrO ₂ System	13
3. Method of Attack and Experimental Methods	16
3.1. Energy Dispersive X-Ray Diffraction Method (EDXRD)	17
3.2. Diffraction work at X17-B1 Beamline at Brookhaven National Labs	20
3.3. X17-B2 Beamline at Brookhaven National Labs	22
3.4. Data Analysis of EDXRD Experiments	24
3.5. Energy Calibration for EDXRD	27
4. Experimental Setup	30
4.1. Diamond Anvil Apparatus Setup for High Pressure and Temperature Study (X17-B2 beamline)	30
4.2. Setup in Parallel Plate Capacitor Geometry for High Temperature and Electric Field Studies (X17-B1 beamline)	31
5. Experiments and Results	33

5.1. High Pressure and Temperature Densification Study	33
5.1.1. Preamble	33
5.1.2. Experimental Results	35
5.1.2.1. Thermokinetic Densification	35
5.1.2.2. Phase Evolution of MgO-Y ₂ O ₃ System	40
5.1.2.3. Theoretical Discussion of Thermokinetic Densification Results	46
5.2. Electric Field Assisted Densification Study	51
5.2.1. Electric Field Effect on Burst mode Densification Temperature and Process	59
5.2.2. Line Profile Analysis of Flash Sintering	64
5.2.3. Electric Field Effect on Sintered Specimens	72
6. Conclusions	81
REFERENCES	84

List of Tables

Table 5.1 Tabulated data calculated by considering cubic MgO(200) peak of first virgin sample as a reference point [7-9]	40
Table 5.2 Tabulated data of flash sintered 8YSZ samples, showing experimental parameters and results.....	64

List of Figures

Figure 2.1 Volume-pressure curves of Y_2O_3 with polyphormic phase transition at room temperature [24].....	5
Figure 2.2 a) Strength and hardness of values and b) Transmittance of $MgO-Y_2O_3$ composite systems in different content values [17].....	6
Figure 2.3 The $MgO-Y_2O_3$ phase diagram showing no solid solubility at $<\sim 1700^\circ C$ [30].....	9
Figure 2.4 The schematic of a FAST/SPS process for the sintering of ceramics [31].....	10
Figure 2.5 Linear shrinkage at different runaway temperatures under varied electric field [35]	12
Figure 2.6 X-ray spectrum of tetragonal 8% $Y_2O_3-ZrO_2$	15
Figure 3.1 Model showing the principle behind Bragg's law: Two photon waves AA' are scattered by the electron density of atomic planes (h k l) and (2h 2k 2l) and exhibit constructive interference at CC' whenever the path difference $AB'+B'C$ is an integral multiple of the wavelength λ resulting in the relation $n\lambda = 2d\sin\theta$. (Figure courtesy of E. K. Akdoğan).....	17
Figure 3.2 Transmission (Laue) mode diffraction with a stationary diffraction volume in space makes the Rutgers approach very suitable for in-situ studies [10, 72, 73].....	21
Figure 3.3 The experimental setup in X17-B2 beamline is based on the Laue method. The hydrostatic pressure is imposed on the sample by a diamond anvil apparatus that can also be heated. A CCD camera provides x-ray tomographic capability in tandem to the in situ temperature and pressure X-ray diffraction capability [7-9, 74, 75].....	23
Figure 3.4 Typical EDXRD spectrum, collected in X17-B1 and X17-B2 [7-10]	24
Figure 3.5 a) EDXRD of LaB_6 standard and b) linear regression for obtaining the energy calibration for EDXRD experiments [10].....	29
Figure 4.1 Schematic of the sample holder setup used in X17-B2 for high pressure and high temperature experiments [82, 83].....	31
Figure 4.2 The schematic of the hot stage used in X17-B1 for high temperature and low electric field experiments [10, 84].....	32
Figure 5.1 Particle size distribution of $MgO-Y_2O_3$ powder used in high pressure studies.....	33
Figure 5.2 Schematic of thermal cycle used in studying pressure effects on the phase stability in the $MgO-Y_2O_3$ binary nanocomposite system [7-9].....	34

Figure 5.3 a) Microscopic shrinkage during isothermal and isobaric soak, b) Variation of cubic MgO lattice with time for 50/50 MgO-Y ₂ O ₃ sample [7].....	36
Figure 5.4 a) Microscopic shrinkage during isothermal and isobaric soak b) Increase in cubic MgO lattice parameter for 50/50 MgO-Y ₂ O ₃ sample under 7 GPa and 1273 K [8].....	37
Figure 5.5 a) Microscopic shrinkage b) Volumetric expansion in cubic MgO unit cell under 5.5 GPa and 1273 K for 80/20 MgO-Y ₂ O ₃ sample [9].....	39
Figure 5.6 a) Initial spectrum from pure MgO-Y ₂ O ₃ at ambient condition b) x-ray spectrum after applying 7 GPa at 298 K [8].....	42
Figure 5.7 a) Spectrum at the beginning of sintering at 1273 K and 7GPa b) Spectrum taken at the end of the sintering after 60 min soak [8].....	43
Figure 5.8 X-ray spectra taken during isobaric and isothermal hold by 3 min intervals at 1273 K[8].....	44
Figure 5.9 a) Spectrum taken at the end of the cycle b) Spectrum taken at X17-B1 beamline after 240 hours aging [8].....	45
Figure 5.10 X-ray spectrums of MgO-Y ₂ O ₃ systems applied (5.5 GPa, 1273 K, 120 min) thermokinetic cycle a) 50/50 weight % b) 80/20 weight % [7, 9].....	47
Figure 5.11 The defect model displaying the dissolution of Y ³⁺ in cubic MgO structure at high pressure [8].....	49
Figure 5.12 Position dependence spectra, taken along yr axis of the hot stage.....	51
Figure 5.13 Time dependence current draw by 8% Y ₂ O ₃ -ZrO ₂ during flash sintering between 876 °C and 930 °C [10].....	53
Figure 5.14 Variation of lattice parameters of 8 % Y ₂ O ₃ -ZrO ₂ as a function of time during flash sintering under 215 V/cm and 0.15 °C/s [10].....	54
Figure 5.15 Variation of unit cell as a function of time during flash sintering [10].....	55
Figure 5.16 EDXRD spectrum collected at 874 °C, 905 °C, and 923 °C to show expansion due to electric field [10].....	56
Figure 5.17 Peak breadth variations as a function of time during flash sintering [10]....	57
Figure 5.18 EDXRD spectrum collected at RT (green dense), 905 °C, and RT (after sintering) to show expansion due to electric field [10].....	58
Figure 5.19 Electric field effect on thermally activated runaway on flash sintering temperature and current draw.....	59
Figure 5.20 Unit cell variation 8% Y ₂ O ₃ -ZrO ₂ samples as a function of time under different electric field.....	61

Figure 5.21 8% $\text{Y}_2\text{O}_3\text{-ZrO}_2$ samples' peak breadths respond as a function of time under electric and thermal field.....	62
Figure 5.22 SEM images of 8% $\text{Y}_2\text{O}_3\text{-ZrO}_2$ samples after electric and thermal field sintering study.....	63
Figure 5.23 The Williamson-Hall plots for determining the isotropic average crystallite size and microstrain from energy dispersive x-ray diffraction data at selected temperatures during the in-situ densification experiment on 8% $\text{Y}_2\text{O}_3\text{-ZrO}_2$	65
Figure 5.24 The time evolution of the isotropic average Williamson-Hall a) crystallite size, and b) microstrain in the flash densification of 8% $\text{Y}_2\text{O}_3\text{-ZrO}_2$	66
Figure 5.25 Time dependence of the anisotropic (101) and (110) Warren-Averbach a) coherently diffracting domain size, and b) d-spacing variation in the flash densification of 8% $\text{Y}_2\text{O}_3\text{-ZrO}_2$	68
Figure 5.26 SEM images of a) Flash sintered at 900 °C, and b) Sinter forged at 1400 °C samples [84].....	74
Figure 5.27 Unit cell variation of a) Flash sintered sample at 900 °C, and b) Sinter forged sample at 1400 °C [84].....	75
Figure 5.28 Volumetric a) viscoelastic deformation and b) anelastic relaxation at unit cell for FS900 and SF1400 samples	77
Figure 5.29 X-ray spectra at room temperature before and flash densification for a) FS900 sample and b) SF1400 sample.....	78
Figure 5.30 FWHM behavior as a function of time during flash sintering [84].....	79

Introduction and Motivation for the Study

In traditionally terminology, we use the term sintering to define the phenomena by which a solid and high dense (close to theoretical limit) is obtained from particulate matter at typically $2/3$ of absolute melting temperature of system of interest. Densification during sintering involves necking between particles due to mass transport that results in shrinkage, reduction in pore size and population in the system of interest [1-5]. The appertaining scientific literature on sintering is vast as it is deemed a fertile ground for discovery and fundamental research on topics such as linear and nonlinear mass transport and irreversible thermodynamic as a function of a plethora of thermodynamic parameters such temperature, time, pressure, electric field, particle size and particle size distribution to name a few [1-6]. From an engineering perspective, the ultimate goal has always been to attain high density at the lowest temperature and shortest time possible which constitutes in a formidable challenge in materials processing. For this purpose, various methods of attack such as small particle size, applied mechanical pressure (hot pressing sintering) or applied electric field (spark plasma and flash sintering) with/without atmosphere controlled systems has been proposed [7-13].

The main mass transport mechanisms for solid state sintering are evaporation-condensation transport and surface diffusion which results neck formation but not physical shrinkage, and lattice or grain boundary diffusion which results both neck formation and physical shrinkage in inorganic particulate systems [1-5]. All of these mechanisms are thermally activated and time dependent processes as they rely on diffusion. According to Thompson-Freundlich equation, the difference in chemical

potential associated with the excess free surface energy due to surface curvature (solid-vapor interface) is inversely proportional to particle size distribution which eventually determines the thermodynamic driving force in sintering process [14]. The initial particle size of the powder and its distribution is the thermodynamic driving force for sintering which one can vary over an appreciable particle size range and distribution. Additional powder characteristics such as particle size distribution, agglomeration, packing density are other important factors one needs to consider but are not very amenable to vary experimentally [1-5].

The desire to reduce the densification temperature and time of ceramic particulate matter, which would enable one to control processes such as grain growth, reactivity, volatility in straight forward manner while achieving high density, has brought renewed interest to this line of research. That is so because of the advances made in high pressure and electric field assisted sintering of ceramics. The application of such additional thermodynamic driving forces provides additional energy to a particulate system undergoing solid state densification [7-13]. Such increases due to pressure and electric field are normally attributed to stress assisted diffusion and joule heating, respectively [1-13]. However, the recent discovery of a new sintering method called flash sintering has changed the mode and manner of perceived densification in particulate matter [10-12]. It has been shown that sintering in ceramics can be accomplished on time scales that are at least 1-2 orders of magnitude shorter while the temperature is typically 50% of the melting temperature, which, at first glance, is contradictory [10-12]. What is known to date in the newly chartered field of flash sintering hints to processes that are electrochemical in nature to which this study will attempt to shed more light.

2. Scientific Background and Systems of Interest

In this section, a concise description of the scientific background constituting the backbone of this dissertation is presented. This section is of a composite nature as it contains the pertinent elements of a literature review, scientific background leading to this study, and the systems of interest in an integrated fashion.

2.1. High Pressure Sintering

In recent years, one of the important lines of research in materials science is the study of materials under high pressure [15]. That is so because of the potential advantages offered in creating polycrystalline microstructures with ultra-low grain size by high pressure processing. Here, the additional pressure imposed on the specimen reduces the sintering temperature. In so doing, it is hypothesized that such a reduction would lead to smaller grain size as grain growth at high temperatures is avoided [15]. For instance, polycrystalline optical materials with grain size < 100 nm are of great interest as it enables one to obtain good optical and mechanical properties concomitantly [16]. Particularly, there is immense interest for cost-effective polycrystalline solids in IR applications so as to replace sapphire which is a very expensive material. For instance, the ultimate goal is to obtain cost-effective polycrystalline solids which possess outstanding mechanical and thermal properties in addition to good optical transparency at 3-5 micron wavelength (mid-wave IR). Yttria (Y_2O_3) is one such solid, possessing good transparency in the said mid-wave range, but lacks sufficient mechanical strength and thermal resistance [17]. Such challenges lead one to consider composite system in which the desired properties could possibly be tailored. To date, the most viable candidate

system is MgO-Y₂O₃ which is one of the subjects of this dissertation and will be discussed in the ensuing section.

2.2. The MgO-Y₂O₃ Nanocomposite System

Single crystal Al₂O₃ (sapphire) is the unrivaled material of choice in IR applications [18]. In principle, it is possible to obtain transparent ceramic materials with a cubic phase -the desired unit cell symmetry for IR applications. However, sintering studies have shown that the result is typically a polycrystalline solid in which the crystallographic symmetry is not cubic [19]. That is why single crystal Al₂O₃ is so popular in IR applications despite its extremely high price. MgO-Y₂O₃ nanocomposites with grain size around 400 nm have been proposed considering the fact that Y₂O₃ has very good transparency in infrared wavelength range [20]. It was presumed that MgO not only would act as an inert component in regard to IR transparency but also impart high strength to the composite [17].

Cubic MgO is one of the most widely studied oxide materials due to its simplicity and its complete lack of high-pressure allotropes, which is why its equation of state is known with utmost precision [21]. It is also a classical pressure calibration material in high pressure research. MgO is a textbook ionic solid, a linear dielectric which has also served as a prototype system to study electrostriction [15]. Y₂O₃ is a rare earth sesquioxides which has polymorphic phase transitions from cubic to monoclinic at about 13 GPa and from monoclinic to hexagonal at about 24.5 GPa [22, 23]. At room temperature, as shown in Figure 2.1, the sequence of phase transition is not reversible when the pressure is released and there is one transition from hexagonal phase to

monoclinic phase which stays stable even in ambient pressure. Having smaller bang gap than $\alpha\text{-Al}_2\text{O}_3$ is significant physical properties makes Y_2O_3 good candidate for IR applications [24].

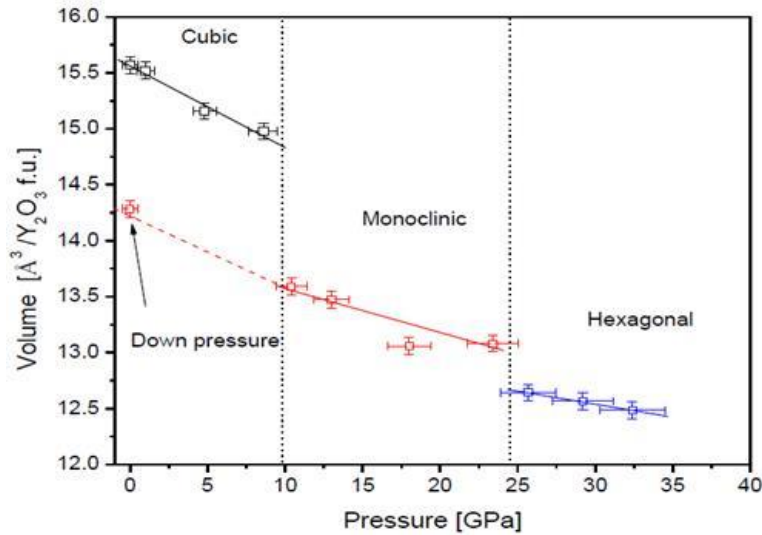


Figure 2.1 Volume-pressure curves of Y_2O_3 with polyphormic phase transition at room temperature [24].

Multiphase composites systems with $\text{MgO-Y}_2\text{O}_3$ ceramic materials may show shows improvement in both optical properties and mechanical properties than their pure forms as shown in Figure 2.2a, and as shown in Figure 2.2b, it is seen that the 85% transmittance in 50/50 vol% $\text{MgO-Y}_2\text{O}_3$ with grain size 200 nm demonstrates that this composite can have sufficient optical transparency in the mid-wave IR [17]. If the mechanical strength can be optimized, the said IR transparency is sufficiently high for this nanocomposite to be implemented in technological applications such as radomes [17]. As shown in Figure 2.2a, $\text{MgO-Y}_2\text{O}_3$ nanocomposites also provide for some degrees of freedom in compositional modifications whereby the mechanical properties can be optimized [17]. For example, the strength of the 50/50 vol % composite is almost two times as much as their pure form, and regarding hardness, all composites display higher

hardness behavior than that of either pure yttria or magnesia. At the same time (see Fig. 2.2b) the optical properties remain unaltered over a wide range of yttria-magnesia ratio which is an immense added bonus from an engineering perspective [17].

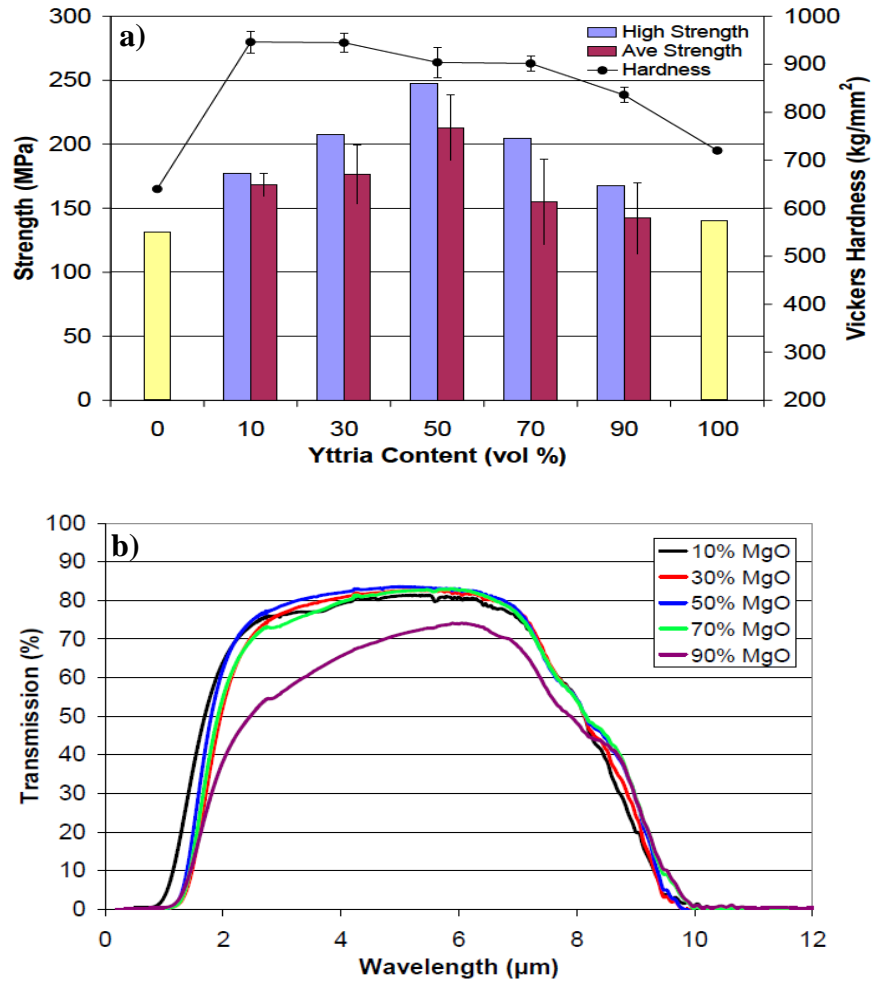


Figure 2.2 a) Strength and hardness of values and b) Transmittance of MgO-Y₂O₃ composite systems in different content values [17].

2.2.1. Optical Properties of Multiphase MgO-Y₂O₃ Composites

In general, polycrystalline ceramics of very high density (>99%) and with a cubic unit cell symmetry are desired for optical applications. Furthermore, the grains size is should, in principle, be smaller than 1 microns so that scattering from grain boundaries is

as minimal as possible, maximizing the optical transparency thereby. However, during high temperature processing such as sintering, high temperature polymorphic (allotropic) forms may form and can then exist metastable at room temperature –a phenomenon that is not desired. That is so because a multi-axial crystal will exhibit birefringence whereas one needs an isotropic optical medium in applications such as IR windows. Since scattering by grain boundaries is huge due to differences of reflective indexing of each constituent in composite system, materials having closer reflective indices are needed to be chosen in a given composite systems. The differences between MgO with reflective index $n=1.36$ @ 600 nm and Y_2O_3 with reflective index $n=1.926$ @600 nm pose substantial limitations on making high transparent composite materials [25]. Especially when the grain size of composite is so close to the wavelength of interest, the scattering becomes even more significant. This mismatching of reflective indexing reduces light transmission gradually in this composite system. However, by decreasing grain size less than wavelength (about $< \lambda/15$), very good transparent materials can be acquired.

Al_2O_3 with reduced grain size to 300 nm is one of the examples reported in the literature as a very light transparent material [26, 27]. While grain growth is promoted by high temperature processing, one desires to work with as small a grain size as possible to obtain good transparency and mechanical strength. However, high sintered density is also a major requirement which, in turn, requires high temperatures. Hence, a compromise is needed which indeed poses a major challenge as alumina is prone to grain growth which is why its single crystal form found lots of traction in IR applications despite high synthesis and processing costs [16, 17].

2.2.2. Grain Size Effect on Phase Transition

In addition to grain size effect on light transmittance of composite, one also needs to consider phase stability and phase transitions under pressure and temperature. Under ambient condition, Y_2O_3 has a cubic structure. However, nanocrystalline Y_2O_3 synthesized with particle size <10 nm by IGC method exhibits monoclinic phase which is also observed in macroscopic Y_2O_3 at high pressures [28, 29]. This phenomena can be explained by The Gibbs-Thomson effect $\Delta p = 2\sigma/r$ (Δp = pressure, σ = surface energy, r = radius of particle). Internal pressure can increase by the curvature of interfacial surface of nanoparticles, for instance; for a particle with 4 nm grain size, 1.5 J/m^2 surface energy could create 1.5 GPa internal pressure that is same order of magnitude as the pressure for monoclinic phase transition [28]. The bottom line is that variation of grain size in composite materials is one of the important considerations for not only good optical aiming, but also to control phase transitions.

2.2.3. Solid Solubility and Grain Growth in Composite Systems

Hot pressing and spark plasma technique are two popular methods for sintering $\text{MgO-Y}_2\text{O}_3$ composites. It is important to attain fully density in such nanocomposites to obtain good mechanical and optical properties as elaborate don in the preceding sections. In $\text{MgO- Y}_2\text{O}_3$ phase diagram as, shown in Figure 2.3, the eutectic point of system is around 2110°C below which there is no solid solubility up to 1700°C [30]. Densification requires some solid solubility, which requires the increase of temperatures in excess of 1700°C . However, grain growth is unavoidable at such high temperatures, which is why pressure assisted techniques become so attractive in this line of research as it potentially

enables one to carry out densification at lower temperatures. However, the behavior of the nanocomposite systems needs to be known as a function of pressure.

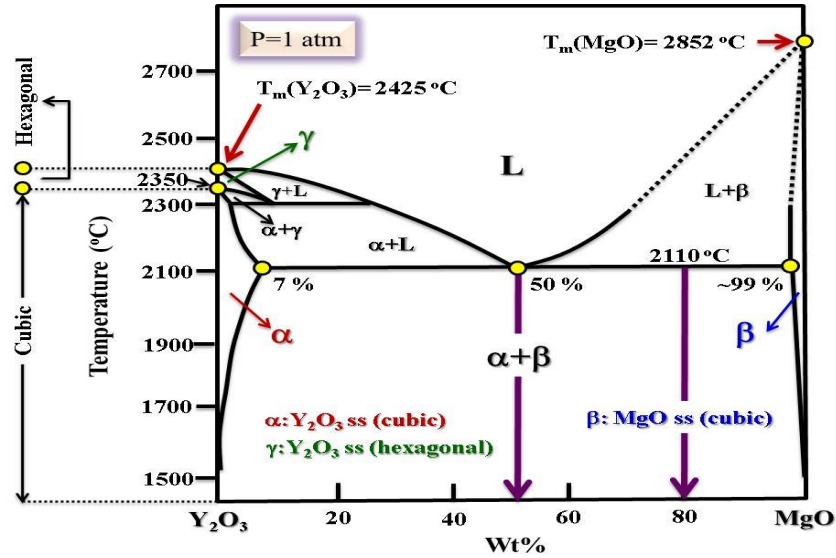


Figure 2.3 The MgO-Y₂O₃ phase diagram showing no solid solubility at <~1700 °C [30].

To acquire fully dense composite material, sintering (densification) study needs to be done at high temperature that causes eventually grain growth of final product [25]. Therefore, one needs to know the phase stability of this system at high temperature and pressures.

2.3. Electric Field Assisted Sintering

In general, the thermodynamic driving force for solid state densification process can be controlled by thermodynamic parameters such as temperature, pressure, and chemical compositions. At first glance, an applied electric or magnetic fields cannot be considered for providing the much needed driving force for solid state densification due to different response of conductive and nonconductive materials. However, the electric

field effect on the thermodynamic driving force for SSD to reduce the sintering temperature and time, where other gradients such as grain growth, reactivity, volatility and such are more difficult to control, has motivated researchers to the development of methods such as spark plasma sintering (SPS) or field assisted sintering technique (FAST) [10-12, 31, 35-39].

FAST/SPS consists of a mechanically loaded system as shown in Figure 2.4, which acts at the same time as high-power electrical circuit [31].

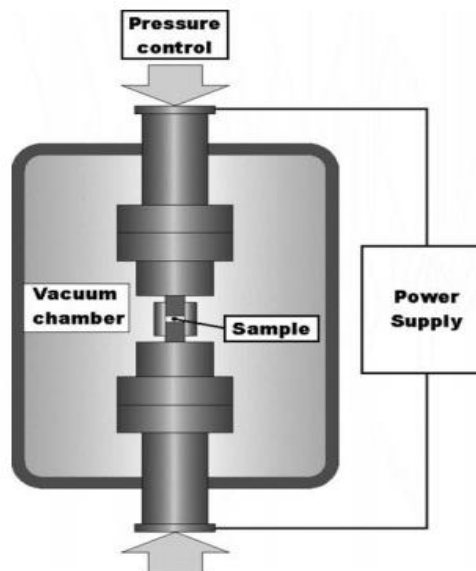


Figure 2.4 The schematic of a FAST/SPS process for the sintering of ceramics [31].

Here, very high current flow is let to pass thorough both graphite die and green dense sample. Due to high conductivity of tool materials, low voltage ($<10\text{V}$) produce very high currents (1 to 10 kA) causing efficient (internal or external) Joule heating of sample. Even in the case of electrically non-conductive sintering powder, heat is quickly and efficiently transferred to the sample which is why FAST has found good traction as a sintering method [31].

Electric field assisted sintering is generally used to sinter refractory ceramics where the electric and the thermal fields are superimposed, resulting densification at lower temperature and time [32-39]. The main purpose in SPS technique is creating internal heat emission inside green dense sample due to localized joule heating which is a more efficient method as compared to other conventional sintering techniques [31]. Sintering at lower temperature and time enables one to prevent grain coarsening. That, in turn, has a positive impact on mechanical and non-mechanical properties as elaborated on earlier.

2.3.1. Flash Sintering

Recently, it has been shown that Joule heating is negligible at low electric field and the applied field activates additional processes increasing mass transport such as surface oxide removal, electromigration and electroplasticity [35]. For instance, the yttria stabilized zirconia system could be sintered up to 97% of theoretical density at 850°C under the application of a nominal 120 V/cm dc electrical field) in seconds instead of hours with conventional densification temperature is >1400°C [35]. In this technique, the electric field is directly applied on desired system by a pair of electrodes, and current is passed through the sample. The instantaneous current draw is observed when the system reaches certain temperature, which is known to scale inversely with the applied electric field magnitude [35-39]. The observed phenomenon is unique because the mass transport rates over the observed time scales are unprecedented.

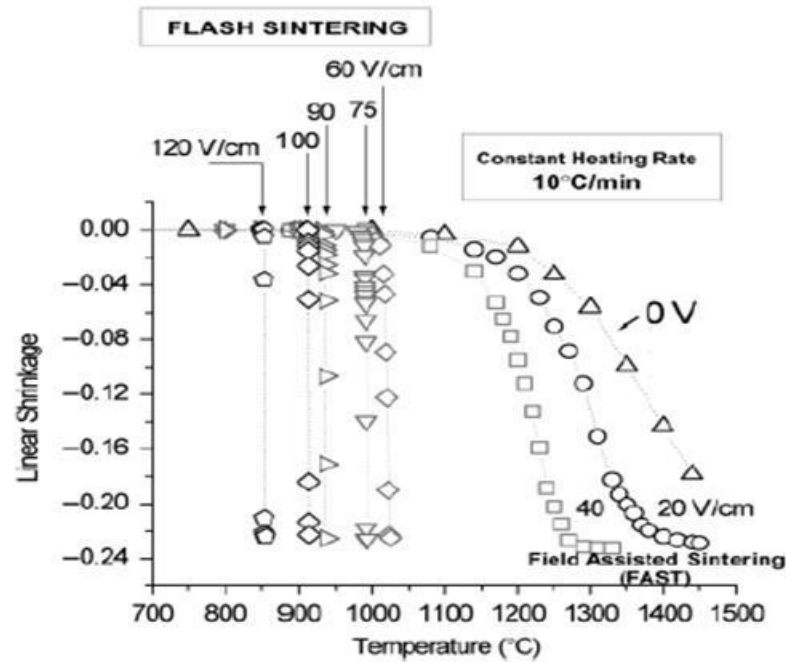


Figure 2.5 Linear shrinkage at different runaway temperatures under varied electric field [35].

Densification of particulate matter using such moderate electric fields has been named flash densification or flash sintering due to the very short time scales involved where the densification occurs in the form of a burst mode. Figure 2.5 depicts the variation of linear shrinkage as a function of temperature [35]. There is, at first, no current draw mechanism observed; however, when the system reached 800-1000 °C, the conductivity of green dense sample increased enormously due to a burst in mass transport, depending on the electric field magnitude. The effect of the applied field on densification is attributed to local melting at grain boundaries to field induced plasticity at high temperatures [38-39]. In the absence of Joule heating, the applied dc electric fields should have an electrostrictive effect on the defect structure in oxides materials because solid state mass transport is ambipolar due to electrostatic charge neutrality considerations [40]. Moreover, space charge could be accumulated on grain boundaries,

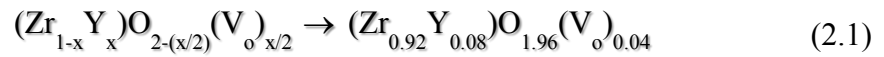
controlling the transport across the boundary [41]. It is beneficial to note that factors such as electric field-defect interactions and electric field localization at interfaces due to difference in conductivity as well as permittivity has to be considered in the densification of ceramics if excessive Joule heating can be controlled. Applying dc electric fields to 8% Y_2O_3 - ZrO_2 (8YSZ), produce very high densification (>95%) at typically half its conventional sintering temperature in few minutes which is comparing with two hours sintering time [35-38]. What is studied to date about flash sintering is macroscopic shrinkage and some Joule heating calculation due to applied fields [35-38]. Here, the in-situ energy dispersive x-ray diffraction (EDXRD) method, which will be well articulated in next section, is utilized to collect data during the burst mode densification step [10]. Due to the high photon energies involved, ultrahigh energy dispersive x-ray diffraction enables us to collect data at 1 sec temporal resolution [10]. This, in turn, enables us to obtain a unit cell scale description of flash sintering which is a study first of its kind.

2.4. The 8% Y_2O_3 - ZrO_2 System

For its hardness, chemical inertness and higher ionic conductivity behavior, Zirconia (ZrO_2) is an important technological solid state electrolyte material that has been exploited in several key industrial applications including solid-oxide fuel cells (SOFC), catalytic sensors, and biomedical [42-47]. One of common feature for pure zirconia is polymorphic phase transition, at ambient pressure, proceeding with monoclinic (stable at the room temperature) to tetragonal (at about 1000 °C) and then to cubic (at about 2370 °C) [48-51]. This feature became one of the obstacle to obtain stable solid zirconia ceramic products via high temperature sintering methods due to the large unit cell volume

variation associated with the transition from tetragonal (8 coordinate Zr^{4+} cations) to monoclinic (7 coordinate Zr^{4+} cations) causing about 9% volumetric expansion [49,51]. Therefore, it is important to stabilize tetragonal or cubic phase of ZrO_2 for high temperature processes at which phase transition can occur, which can cause very high strain and mechanical distortion inside sample [52, 58].

The stabilized tetragonal or cubic phase at room temperature can be acquired in many ways such as using dopant like ceria, calcia and, yttria [45, 52-58]. Mechanical, chemical, and electrical properties of ZrO_2 can be tuned by this approach [52, 54, 59].



To stabilized tetragonal phase of zirconia, doping Y_2O_3 at certain level is needed, and results in oxygen vacancies for charge compensation on anion site [52-61]. Specifically, Zr^{4+} ions in the zirconia unit cell are replaced with Y^{3+} ions which results oxygen vacancies due to three O_2^- ions in Y_2O_3 is exchanged with four O^{2-} ions in ZrO_2 lattice structure [60,61]. These mobile vacancies in fluorite structured Zirconia create very high ionic conductivities even at lower temperature [59, 62, 63]. Considering low temperature and high oxygen ionic conductivity as a biggest challenge in SOFCs, this property of YSZ makes it an outstanding solid electrolyte in solid oxide fuel cell power generators [42, 43]. However, the oxygen vacancy concentration (by doping) cannot be arbitrarily changes as vacancy clustering at high concentrations adversely affects ionic conductivity by oxygen vacancy diffusion [64-67]. The maximum ionic conductivity can be achieved at 8% YSZ at 800- 1000 °C [66, 67]. That is why 8% YSZ was chosen as

one of the system of interest for in this study. As a corollary information, one should note that due to metastable nature of the phases stabilized in YSZ solid solutions, stress induced transformation toughening becomes a strengthening mechanism of ZrO_2 , which reduce the crack propagation under severe conditions by phase transformation which results local volumetric changes [52- 54]. This characteristic property of some YSZ solid solutions should be a concern in densification studies involving applied pressure or electric field as it may trigger such phase transitions.

Figure 2.6 illustrates the x-ray spectrum of tetragonal (P42/nmc) 8% Y_2O_3 - ZrO_2 , taken in X17-B1 beamline in National Synchrotron Light Source (NSLS) at Brookhaven National Laboratory (BNL). This is the system of interest for in situ studies of field assisted sintering. During such experiments, the lattice parameters are monitored as a function of time, temperature and applied electric field magnitude with an unprecedented temporal resolution of 1-2 seconds. Furthermore, anisotropy in peak broadening was also monitored as a function of time, temperature and applied electric field magnitude as oxygen vacancies should in principle have an impact on crystallite size and microstrain.

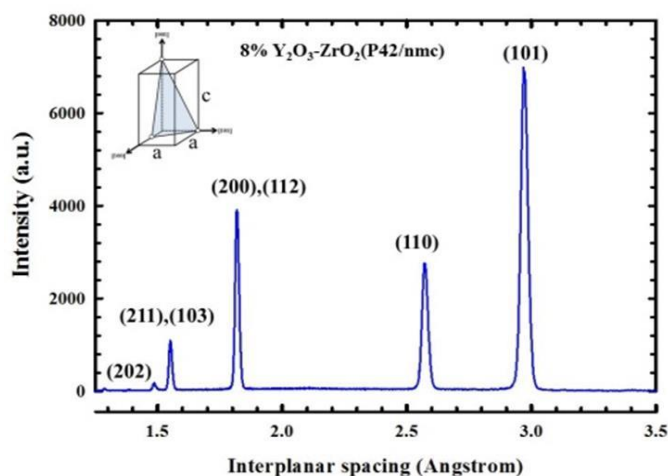


Figure 2.6 X-ray spectrum of tetragonal 8% Y_2O_3 - ZrO_2 .

3. Method of Attack and Experimental Methods

The main experimental tool of analysis in the study was high energy x-ray synchrotron diffraction because of its unrivaled power for in situ work in materials research. Specifically, due to the high brightness of synchrotron radiation, one can carry out diffraction work while imposing a multitude of boundary conditions such as temperature, pressure and electric field, and collect high precision as well as high resolution diffraction data within a timeframes that are otherwise not accessible with conventional diffraction methods. In what follows, succinct description of the methods is provided.

In its conventional definition, x-ray diffraction is due to the scattered incident x-ray photons by the electron density of atoms, the outcome of which is governed by the microsymmetry (space group symmetry) of the atoms arrangements in a given material [68, 69]. In the case of polycrystalline or single crystal materials, the diffraction phenomenon is particularly useful in determining the unit cell volume as the wavelength of the x-ray used is commensurate with the atomic interplanar spacing [68, 69]. The direction of the scattered radiation, which is the experimentally measured quantity in a conventional (Bragg-Brentano) diffraction experiment, is given by the famous Bragg law (see Eq. 3.1) that is depicted in Fig. 3.1. In the Bragg model, which is based on the kinematic theory of x-ray diffraction [70], two photon waves AA' are scattered by the electron density of atomic planes (h k l) and (2h 2k 2l) and exhibit constructive interference at CC' whenever the path difference AB'+B'C is an integral multiple of the wavelength λ resulting in the relation;

$$n\lambda = 2d_{hkl}\sin(\theta_{hkl}), \quad (3.1)$$

where n is the order of the diffraction, d is the interplanar spacing of $\{hkl\}$, and θ_{hkl} is the Bragg angle of the diffracted x-rays from $\{hkl\}$.

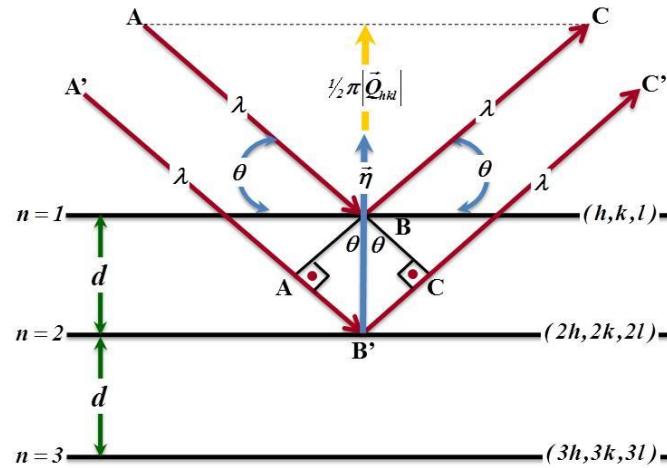


Figure 3.1 Model showing the principle behind Bragg's law: Two photon waves AA' are scattered by the electron density of atomic planes $(h\ k\ l)$ and $(2h\ 2k\ 2l)$ and exhibit constructive interference at CC' whenever the path difference $AB' + B'C$ is an integral multiple of the wavelength λ resulting in the relation $n\lambda = 2d\sin\theta$. (Figure courtesy of E. K. Akdoğan)

As will be discussed further in the next section, the Bragg-Brentano diffraction method has severe limitation in materials research which is why the use of energy dispersive x-ray diffraction method was brought to bear in this study.

3.1. Energy Dispersive X-Ray Diffraction Method (EDXRD)

The energy of a photon is given by the Planck-Einstein equation, as shown below,

[71]

$$E = h\left(\frac{c}{\lambda}\right), \quad (3.2)$$

where the frequency (ν) is related to the wavelength through the Planck's constant (h ; 4.1357×10^{-15} eV.s) and the speed of light (c ; 2.9979×10^8 m/s). By setting $n=1$ in the Bragg's law (see Eq. 3.1.) and combining it with Eq. 3.2, one obtains the governing equation for energy dispersive x-ray diffraction as

$$|\vec{Q}_{hkl}| = \frac{1}{d_{hkl}} = \left(\frac{hc}{2\sin\theta} \right) \frac{1}{E_{hkl}}, \quad (3.3)$$

where $\{hkl\}$ are the Miller indices of family of atomic planes responsible for a given Bragg reflection of interplanar spacing d_{hkl} , $|\vec{Q}_{hkl}|$ is magnitude of the reciprocal vector satisfying the Laue condition for $\{hkl\}$, θ is the Bragg angle that is kept constant in an EDXRD experiment and is typically $3-4^\circ$, and E_{hkl} is the scattered energy from $\{hkl\}$ which is the experimentally measured quantity [68, 73]. As per Eq. 3.3, one measures the magnitude of $|\vec{Q}_{hkl}|$ directly in an EDXRD experiment from which the d_{hkl} is computed very accurately. In this regard, the EDXRD method is superior to conventional Bragg-Brentano methods [68, 73]. That is so because in Bragg-Brentano methods the scattering angle (θ) is related to the interplanar spacing through a trigonometric function (see Eq. 3.1) which, indeed, amplifies the typically large specimen height displacement error in the measurement of θ .

The elastic strain (ϵ), as defined by the change in interplanar spacing (Δd), is obtained by measuring the peak shift (ΔE) of a given (hkl) from the EDXRD patterns according to

$$\varepsilon_{hkl} = \left(\frac{\Delta d_{hkl}}{d_{hkl}^o} \right) = \frac{\Delta E_{hkl}}{E_{hkl}^o}, \quad (3.4a)$$

where

$$\begin{Bmatrix} \Delta d_{hkl} \\ \Delta E_{hkl} \end{Bmatrix} = \begin{Bmatrix} d(\sigma) - d_{hkl}^o \\ E(\sigma) - E_{hkl}^o \end{Bmatrix}, \quad (3.4b)$$

and where the superscript “o” refers to the stress or more generally, perturbation free value [72, 73].

In summary, we conclude from the forgoing discussion that elastic strain measurements involves determining peak shifts under an applied generalized force (temperature, pressure, electric field) resulting in a change in the unit cell volume, relative to the free state (no perturbations) by using a suitable Bragg reflection. In other words, strain measurements by X-ray diffraction in general, and by EDXRD in particular, utilizes the separation of atomic planes as a strain gauge. Therefore, X-ray measurements of strain are highly precise because it entails the measurements of atomic scale changes with a high sensitivity probe. Furthermore, one is able to measure the strain in each phase of a multiphase material. For example, consider a two phase material which has a microstructure similar to marble. If such a material is subjected to a given state of temperature, pressure and electric field, for instance, the strain in each phase of this marble-like material can be determined. This is perhaps the most important advantage of stress/strain measurements using X-ray diffraction as compared to macroscopic strain measurement methods. One may, therefore, notice that X-ray strain measurements constitute the experimental backbone in the in situ analysis of microstructural evolution in material processing. Moreover, it is important to realize that x-ray measurements yield

elastic strain only. The material under investigation might have been strained beyond its elastic limit, thereby exhibiting plasticity as well. If the macroscopic total strain is known then the plastic strain can also be computed by measuring the elastic strain since the strain are additive; $\epsilon_{\text{total}} = \epsilon_{\text{elastic}} + \epsilon_{\text{plastic}}$. However, in this study, no measurement of plastic strains was carried out as all phenomena of interest did not involve any plastic deformation.

3.2 Diffraction work at X17-B1 Beamline at Brookhaven National Labs

About 60% of the EDXRD experiments reported in this dissertation were carried out at X17-B1 beamline located in the National Synchrotron Light Source (NSLS), Brookhaven National Laboratory (BNL), Upton, New York. As shown in Fig. 3.2, high energy photons photon of multiple wavelengths (polychromatic radiation) are created by passing highly energetic photos through a superconducting wiggler which increases their energy up to 200 keV, making it the most energetic beam lime at the NSLS. The penetrating power of the x-rays at the X17-B1 are unrivaled in a sense that one can transmit such high energy x-rays through 2-3 m of aluminum, 5 cm of steel, 1.3 mm tungsten, and 2.5 cm $\text{Y}_2\text{O}_3\text{-MgO}$ composite, to name a few while the attenuation of soft x-rays in such materials are measured in microns. Here, the incident photons are admitted to the sample stage through collimating slits (2 mm thick Thallium plates) by which the spatial resolutions of the data collection is determined as well as the data sampling statistics are adjusted which we will explain in what follows. The sample is placed on a precision sample stage which can be translated in all three principle directions in the 3D Cartesian coordinate system. A cryogenically cooled Ge detector with an energy

resolution of $\sim 300\text{eV}$ is placed on the opposite side of the specimen at a pre-determined Bragg angle ($2\theta \sim 3^\circ$ to 4°) [10, 72, 73].

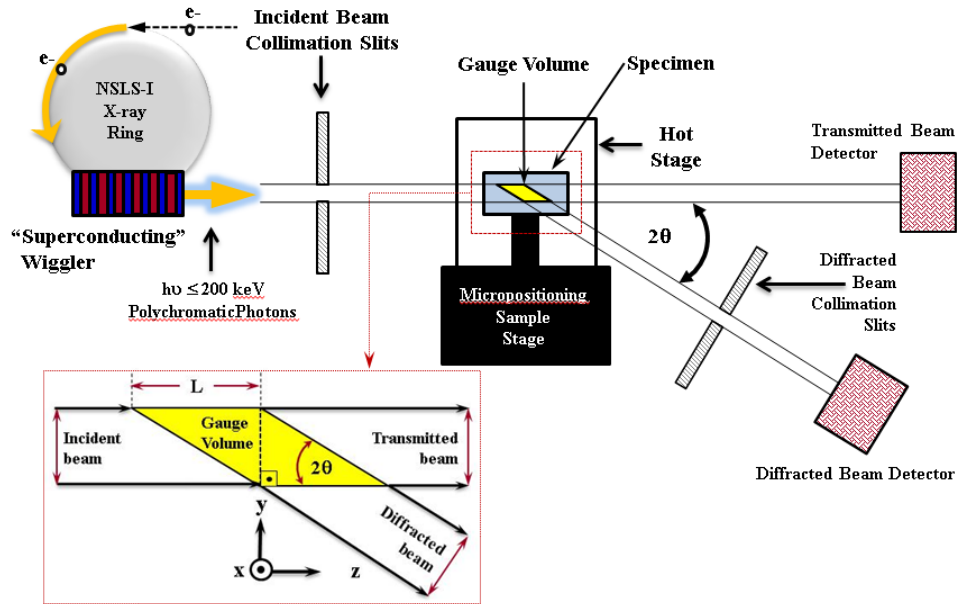


Figure 3.2 Transmission (Laue) mode diffraction with a stationary diffraction volume in space makes the Rutgers approach very suitable for in-situ studies [10, 72, 73].

The method utilized at X17-B1 is essentially a transmission mode diffraction technique (Laue geometry) which is ultimate difference from the other beamlines at NSLS. As shown in Fig. 3.2, the transmitted and diffracted beams form what is called gauge volume (GV). The GV can be visualized as the volume element in which diffraction takes place in conformity with the Bragg's law. The size of the GV can be controlled by two parameters: a) the Bragg angle, and b) the slit sizes. The Bragg angle, which can be set to $3\text{--}12^\circ 2\theta$, determines the length of the GV along the z-direction (see

Fig. 3.2) while the slit sizes determines the dimensions in the x and y-directions. The geometry of the GV is rhombic with a rectangular cross section. Simple geometrical considerations relate the gauge length (GL) to the slit opening S_i and S_d of the incident and diffracted beam collimation slits opening perpendicular to the x-ray beam, and the Bragg angle θ as follows:

$$G_L = \frac{S_i}{\sin(2\theta)} + \frac{S_d}{\sin(2\theta)} \quad (3.5)$$

As can be verified from Fig. 3.2, the G_L determines the GV for a given Bragg angle and it is of primary importance to ensure proper counting statistics in an EDXRD experiment. Namely, the number of grains enclosed in the GV determined the averaging of the diffracted intensities and one typically needs 10000 grains or so for good statistics. In nano grained materials (~100 nm grain size), therefore, the gauge volume can be kept rather small, imparting remarkable spatial resolution to the diffraction technique of the X17-B1 beamline.

3.3. X17-B2 Beamline at Brookhaven National Labs

The experimental setup for the X17-B2 beamline, as depicted in Fig. 3.3, works on the same principles as the X17-B1 beam line. Namely, it is also based on a transmission mode x-ray diffraction method. Here, the maximum photon energies are limited to 100 keV, which is 50% lower than that of the X17-B1 beamline. The photon energies are largely sufficient to harness all the advantages of high energy EDXRD [7-9].

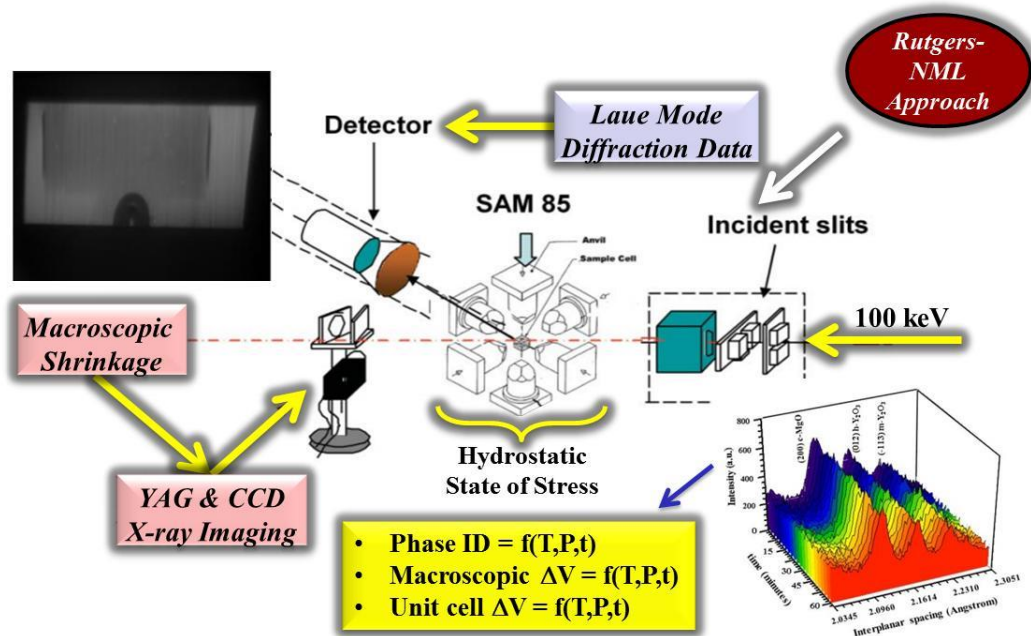


Figure 3.3 The experimental setup in X17-B2 beamline is based on the Laue method. The hydrostatic pressure is imposed on the sample by a diamond anvil apparatus that can also be heated. A CCD camera provides x-ray tomographic capability in tandem to the in situ temperature and pressure X-ray diffraction capability [7-9, 74, 75].

The X17-B2 beamline is a so-called high pressure beamline to conduct studies as a function of time, temperature and hydrostatic pressure. The beamline has a diamond anvil apparatus that sits in the beam path similar to the sample stage in the X17-B1 beamline. Diffraction data is obtained by placing the GV on the body center of the specimen while it is subjected to high pressure, high temperature, or both. The typical Bragg angle used in such experimental work is $2\theta=12^\circ$ [7-9]. This beamline is also equipped with a CCD camera as shown in Fig. 3.3 which enables one to obtain tomographic images of the sample under the imposed boundary conditions as a function of time in addition to the diffraction data [7-9, 74, 75].

3.4. Data Analysis of EDXRD Experiments

A typical time-resolved and representative X-ray spectrum of the $\text{Y}_2\text{O}_3\text{-MgO}$ system, which was collected at the X17-B2 beamline with a Ge detector, is shown in Figure 3.4. Here, the diffracted intensity is plotted as a function of interplanar spacing (as obtained via Eq. 3.4a) and time. Such time resolved experiments with various time resolutions were carried out as a function of temperature and pressure at X17-B2 beamlines, and as a function of temperature and electric field at the X17-B1 beamlines.

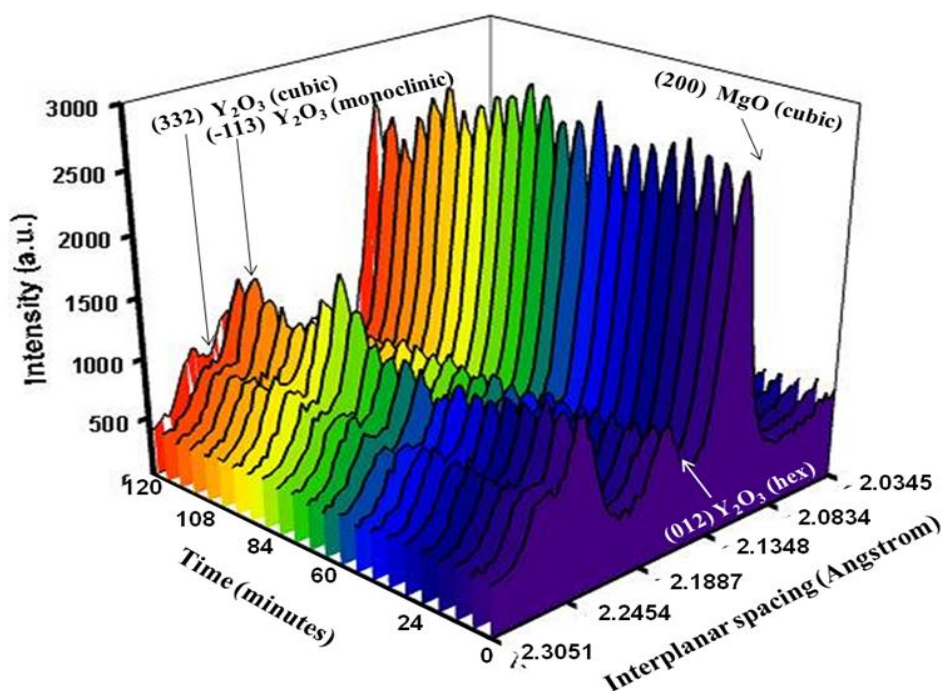


Figure 3.4 Typical EDXRD spectrum, collected in X17-B1 and X17-B2 [7-10].

The data, acquired in such EDXRD experiments provides two valuable sets of information as a function of time and at a given temperature and pressure or temperature and electric field once peak positions are carefully determined by peak deconvolution:

(1) The shift in peak position gives the change in unit cell volume, which may or may not be defined as an elastic strain, according to

$$\varepsilon_{hkl} = \left(\frac{\Delta d_{hkl}}{d_{hkl}^o} \right) = \frac{\Delta E_{hkl}}{E_{hkl}^o} = - \frac{C_{hkl} - C_{hkl}^o}{C_{hkl}^o} \quad (3.6)$$

where C is the channel number corresponding to the peak with Miller indices (hkl) as determined by the Ge detector. Here, C-data is the raw data prior to energy calibration. The superscript “o” has its usual meaning as defined earlier in Eq. 3.4b.

(2) The peak breadth after fitting with a pseudo-Voigt profile shape function [76], gives information about non-uniform behavior inside lattice such which go by the name coherently diffracting domain size and micro-strain (a.k.a. d-spacing variation). Peak broadening was used in the analysis of electric field effects on 8%Y₂O₃ doped ZrO₂ where the first line of attack was the modified Williamson-Hall (W-H) method [77] in conjunction with the all observed reflections' peak position and profile parameters. The peak widths (β) of the reflections were obtained by peak fitting of a pseudo-Voigt profile shape function (PSF), which was then plotted as a function of energy (E^2).

$$\beta_{hkl} = \left(\frac{K(0.5hc)}{\langle L \rangle \sin(\theta)} \right) + (2 \langle u \rangle E_{hkl})^2, \quad (3.7)$$

where K is the Scherrer's constant (~0.94 for equiaxed crystallites) [68], $\langle L \rangle$ is the volume weighted average crystallite size, θ is the Bragg angle which is typically 1.5° in this study, $\langle u \rangle$ is the so-called volume weighted average microstrain (a.k.a. d-spacing variation), and E_{hkl} is the centroid coordinate of the peak of interest as determined by peak fitting with the said PSF. The correction for instrumental broadening was made

using LaB₆ data by following standard procedures [76]. As per Eq. (3.7), the intercept of the β^2 vs. E^2 plot yields $\langle L \rangle$, while the slope gives $\langle u \rangle$ which suggests that the crystallite size and microstrain. The modified Williamson-Hall crystallite size and microstrain analysis used herein, on the other hand, represents isotropic averages which precludes the analysis of anisotropy. To assess anisotropic effects, we utilized the parameterized Warren-Averbach (W-A) method as the second and main method of attack, and applied it on the desired reflections to monitor the evolution of the coherently diffracting domain size (CDDS; $\langle L_{hkl} \rangle$), d-spacing variation (DSV; $\langle u_{hkl} \rangle$), and the anisotropy thereto appertaining [78-79]. Also, the use of the W-A method enabled us to verify the findings of the Williamson-Hall analysis as well. In the application of the W-A method, the (101) and (110) peaks were fitted with a pseudo-Voigt profile shape function from which the peak width (β) and the so-called mixing parameter (η) was obtained. The Lorentzian (β_L) and Gaussian (β_G) contributions to the measured β was obtained from [80];

$$\left(\frac{\beta_L}{\beta} \right) = 0.017475 + 1.5000484\eta - 0.534156\eta^2 \quad (3.8)$$

$$\left(\frac{\beta_G}{\beta} \right) = 0.0184446 + 0.812692\sqrt{(1 - 0.998497\eta)} - 0.659603\eta + 0.44542\eta^2 \quad (3.9)$$

After obtaining the Lorentzian and Gaussian contributions to the peak breadth, the $\langle L_{hkl} \rangle$ and $\langle u_{hkl} \rangle$ was computed from the Scherrer equation and the expression for microstrain which we produce for continuity in what follows [80];

$$\langle L_{hkl} \rangle = \frac{Khc}{2(\beta'_L)_{hkl} \sin(\theta)} \quad (3.10)$$

and

$$\langle u_{hkl} \rangle = \frac{(\beta'_G)_{hkl}}{2E_{hkl}} \quad (3.11)$$

where K , h , c , θ and E are as defined before (see Eqs. 3.1-3.3 and 3.7). Here, the primes on β_L and β_G represent the peak widths that were corrected for instrumental broadening following Ref. [80] and using a LaB_6 standard. According to the Warren-Averbach formalism, the CDDS is the characteristic length of the defect-free region in the $[hkl]$ along which it is measured in a crystalline solid exhibiting finite size broadening. [78-80] Implicitly and as per this formalism, the CDDS also represents the mean separation between defects or defect clusters in the $[hkl]$ along which it is measured with no specific reference to the type of crystalline defects responsible for such broadening unless there is plausible *a priori* knowledge of the dominant defect(s). The upper limit for CDDS measurement by x-ray diffractometry is ~ 120 nm, which is also the limiting value of the mean separation of defects and defect clusters that can be measured by x-ray diffractometry [76-79]. On the other hand, the d-spacing variation (DSV; a.k.a. microstrain) is due to localized (non-uniform) chemical and structural perturbations arising from phenomena such as chemical composition fluctuations, strain field around solute atoms, vacancies and their clusters, dislocations, stacking faults to name a few [80].

3.5. Energy Calibration for EDXRD

The Figure 3.4 depicts the data, taken in the Rutgers EDXRD experiment, which is the intensity of the diffracted reflection as a function of channel number. Each channel

number in Germanium detector represents a certain energy point which then needs to be calibrated and reflected into an energy scale for further calculation. The range of channel numbers is from 0-8192 corresponding to an energy range of 0-200 keV. $K\alpha_1$, $K\alpha_2$ and $K\beta_1$ lines of X-ray absorption (fluorescence lines) standards are used for calibration of the channel numbers against the energy scale for the < 40 keV range, while the diffraction peaks of the standards are used for calibration in the >40 keV range. (see Fig. 3.5a as an example).

Calibration of the channel numbers against the energy scale is accomplished by measuring the $K\alpha_1$, $K\alpha_2$ and $K\beta_1$ lines of X-ray absorption standards such as Gold (Au), Silver (Ag), Platinum (Pt), Cerium (Ce), and diffraction standards such as Cerium oxide CeO_2 , Steel (Fe), Copper (Cu) and Gold (Au), respectively. Such a calibration results in a linear calibration curve relating energy to channel number is shown in the figure below. [10]. The LaB_6 standard also served as a line broadening standard. The instrumental broadening for the set-up used in this study is dominated by the detector and is $\sim 1\%$ which is measured as $(\Delta E/E_0)$, where ΔE is the width of the peak of interest at 50% of maximum intensity and E_0 is the centroid coordinate of the peak [81]. By calibration method, we are able to eliminate the instrumental errors. As a result of calibration, a linear calibration curve represents that energy is proportional channel number as shown in the Figure 3.5b.

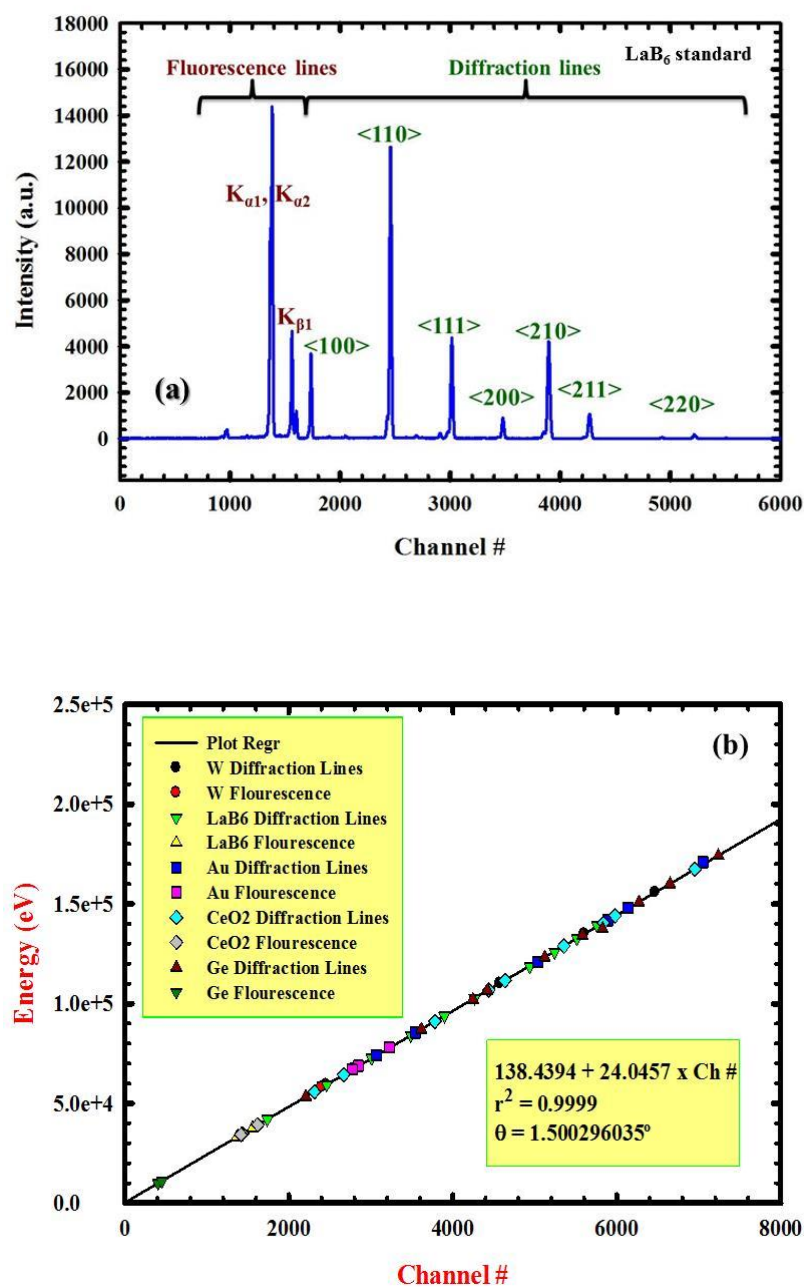


Figure 3.5 a) EDXRD of LaB₆ standard, and b) linear regression for obtaining the energy calibration for EDXRD experiments [10].

4. Experimental Setups

In this section, experimental setups that were used in mounting the specimens of interest onto or into the diffraction stages of the beamlines X17-B1 and X17-B2 are presented. The mode and manner in which the experimental setups were used are of utmost importance in the in situ studies of pressure temperature and electric field effects on the materials behavior which is why a separate section is dedicated in this dissertation.

4.1. Diamond Anvil Apparatus Setup for High Pressure and Temperature Study (X17-B2 beamline)

The specimen holder used for high pressure work is shown in Fig. 4.1. The sample holder is indeed an integrated system by itself, consisting of BN inner chamber holding the specimen to which is attached a thermocouple. A graphite carbon sleeve, which is the heating element of the specimen holder, surrounds the BN sample holder. The graphite sleeve is surrounded by an alumina jacket. The assembly is capped with alumina plugs which are separated by a gold foil from the specimen on both ends. The assembly is embedded in a BN-epoxy composite cube and is then placed into the diamond anvil apparatus [82, 83]. The load that can be applied to the diamond anvil apparatus is rated as 60 tons. For the specimen sizes used in this work 1 mm diameter cylinder of 3 mm height, we were able to go to 5-7 GPa while the sample was heated to 1000 °C. The state of stress created by the diamond anvil apparatus is called nominal hydrostatic compression [7-9]. By using this set-up, time-resolved diffraction experiments at high pressures and temperatures were conducted.

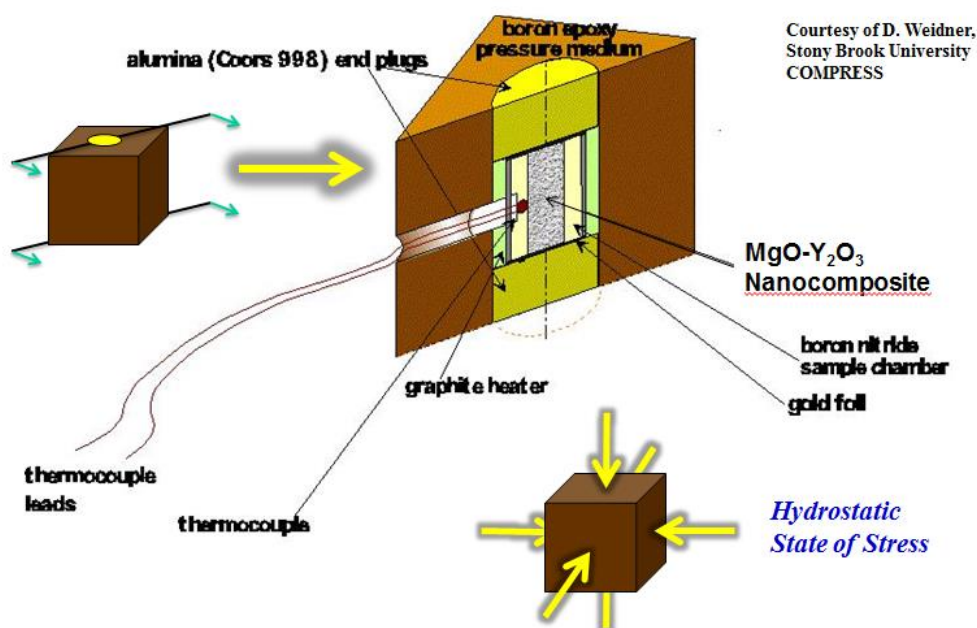


Figure 4.1 Schematic of the sample holder setup used in X17-B2 for high pressure and high temperature experiments [82, 83].

4.2. Setup in Parallel Plate Capacitor Geometry for High Temperature and Electric Field Studies (X17-B1 beamline)

For studies requiring the application of an electric field, an in-house custom-made (see Figure 4.2) hot stage (HS) was fabricated enabling one to heat the sample while applying a dc electric field in the parallel plate geometry [10, 84]. The HS is comprised of a spring loaded ceramic (insulator) specimen holder that is resistively heated to which are attached leads that are used to apply the electric field. The said HS enclosure is mounted on the positioning stage (see Fig. 4.1) and exposed to the beam. The GV is then carefully placed on the body center of the specimen and then is resistively heated with a nominal heating rate of 9 °C - 20 °C per minute [10, 84]. Meanwhile, an applied dc electric field, varied between 100-300 V/cm magnitudes, is imposed on the specimen. The temperature and leakage current of the specimen were monitored. While the system

temperature is let go up to 1000 °C, depending on the experiments, the x-ray data is collected every 1 or 2 seconds intervals.

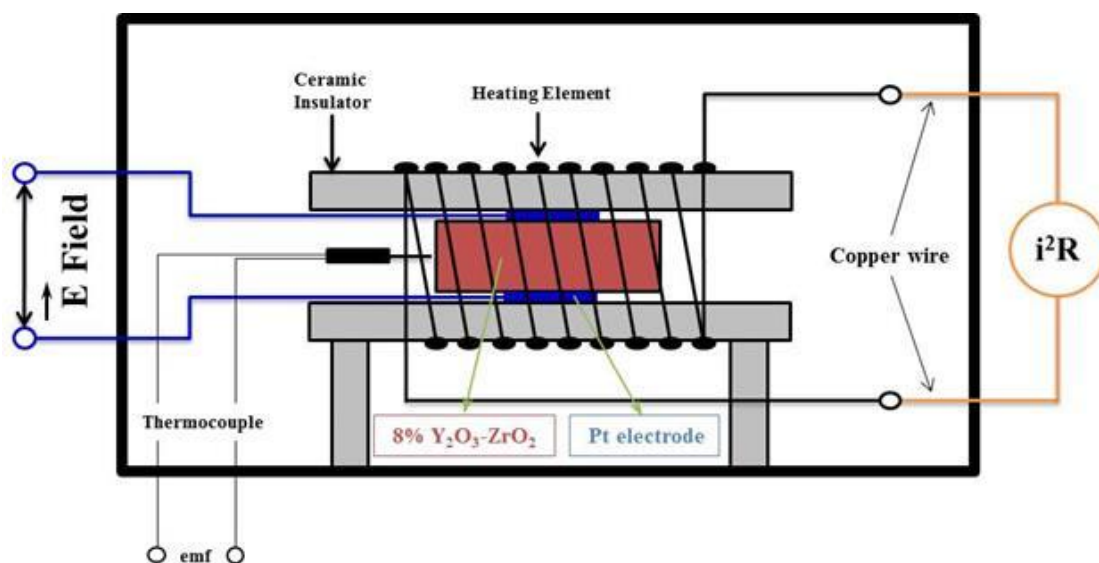


Figure 4.2 The schematic of the hot stage used in X17-B1 for high temperature and low electric field experiments [10, 84].

5. Experiments and Results

The experimental results will be presented in two sections: Section 5.1 presents the results on high pressure studies on the MgO-Y₂O₃ nanocomposite system, while Section 5.2 pertains to the studies on electric field effect in the Y₂O₃-ZrO₂ system.

5.1. High Pressure and Temperature Densification Study

5.1.1. Preamble

The experiment is performed by using a diamond anvil apparatus [82, 83] with high energy polychromatic x-ray radiation at which photon energy goes up to 100 keV at the X17-B2 beamline of the National Synchrotron Light Source (NSLS) in Brookhaven National Laboratory (BNL). The Bragg angle is set to $2\theta=6.62^\circ$. High purity commercial MgO and Y₂O₃ powder (as shown in Figure 5.1, average particle size about 90 nm) were very homogeneously mixed in different content 50/50 (MgO/ Y₂O₃) weight percent and 80/20 (MgO/ Y₂O₃) weight percent by Raytheon Company [7-9].

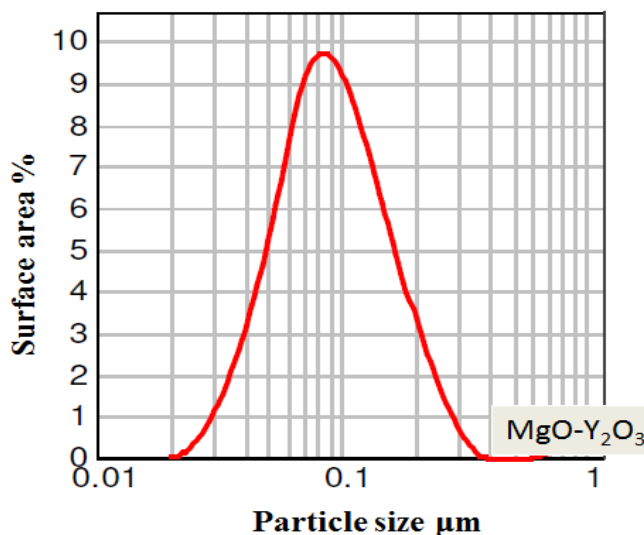


Figure 5.1 Particle size distribution of MgO-Y₂O₃ powder used in high pressure studies.

The nanopowders are packed inside a special specimen (see Sect. 4.1 for its description) and then placed in a diamond anvil apparatus as explained earlier. The MgO phase of the nanocomposite was used as a pressure standard for pressure calibration [87]. Two compositions, 50/50 weight % and 80/20 weight % content MgO-Y₂O₃, were studied at 5.5 GPa hydrostatic pressure as shown Figure 5.2 (black line). The thermal cycle used is displayed in the schematic by the following steps: (i) process 1-2 is isothermal compression to 298 K , 5.5 GPa; (ii) process 2-3 is isobaric heating to 1273 K , 5.5 GPa; (iii) process 3-4 is isothermal and isobaric exposing at 1273 K, 5.5 GPa, 120 min for sintering; (iv) process 4-5 is isobaric cooling to 298 K, 5.5 GPa ; (v) process 5-6 is isothermal decompression to ambient conditions. Another 50/50 weight % MgO-Y₂O₃ nanocomposite was studied at 7 GPa for 60 minutes (blue line) [7-9].

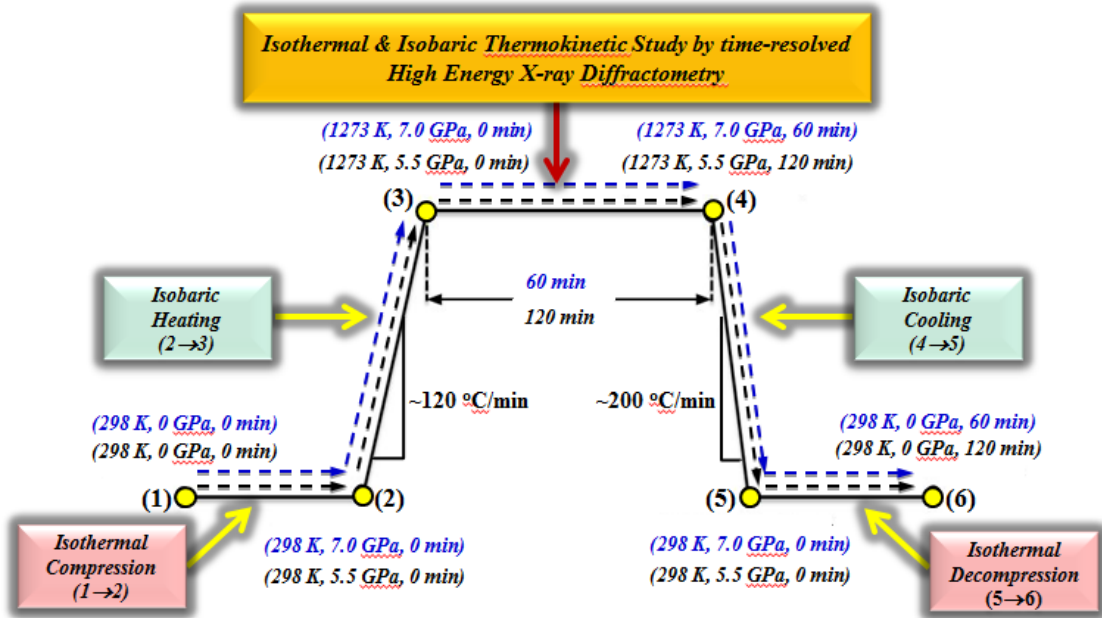


Figure 5.2 Schematic of thermal cycle used in studying pressure effects on the phase stability in the MgO-Y₂O₃ binary nanocomposite system [7-9].

At each point in the thermal cycle, diffraction data was collected, while a total of 20 scans were taken with equal intervals over a span of 120 min and 60 min at 1000 °C, respectively. To observe the microscopic linear changing of samples during thermal cycle, x-ray tomographic images were also recorded. As also shown in Figure 5.2, the specimens were cooled to room temperature relatively fast (~ 200 °C/min).

5.1.2. Experimental Results

Here, the results organized in two sections: Firstly, the results on the thermokinetics of densification are presented. Secondly, the results on the phase evolution in the MgO-Y₂O₃ nanocomposite system is shown.

5.1.2.1. Thermokinetic Densification

To analyze the effect of pressure and temperature on the MgO-Y₂O₃ in the context of densification, we followed the cubic MgO (200) reflection as a function of time at 1000 °C and at a given pressure from which the time-resolved lattice parameter and the unit cell volume were obtained. As shown in Figure 5.3, there is 0.8% macroscopic linear shrinkage, which corresponds 2.4% volumetric shrinkage [86], in the 50/50 MgO-Y₂O₃ system at 1000 °C under 5.5 GPa within 120 minutes. The macroscopic shrinkage is accompanied by an anomalous 0.84% volumetric expansion of the cubic MgO unit cell while we did not observe discernable changes in the Y₂O₃ unit cell volume. Hence, one concludes that some Y₂O₃ is dissolved in MgO under high pressure and temperature [7].

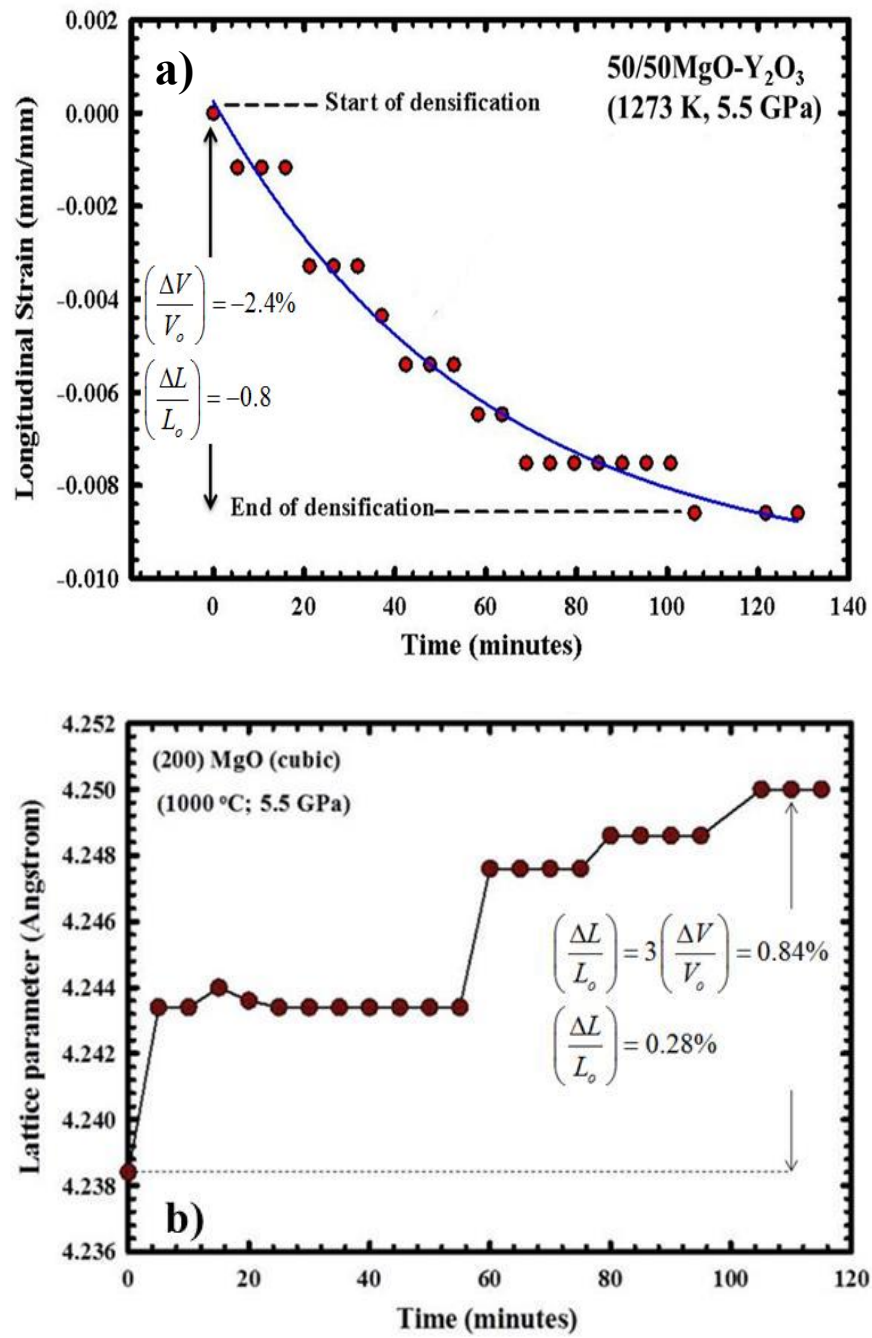


Figure 5.3 a) Microscopic shrinkage during isothermal and isobaric soak, b) Variation of cubic MgO lattice with time for 50/50 MgO-Y₂O₃ sample [7].

As shown in Figure 5.4, when the same experiment for the 50/50 MgO-Y₂O₃ system is repeated at 7 GPa for a period of 60 minutes, one observes a volumetric densification shrinkage of 3.3 % which is an ~30% increase as compared to the shrinkage at 5.5 GPa. At the unit cell level, the expansion of the cubic MgO unit cell is 1 % while the Y₂O₃ unit cell volume remains constant [8] (see Figure 5.4).

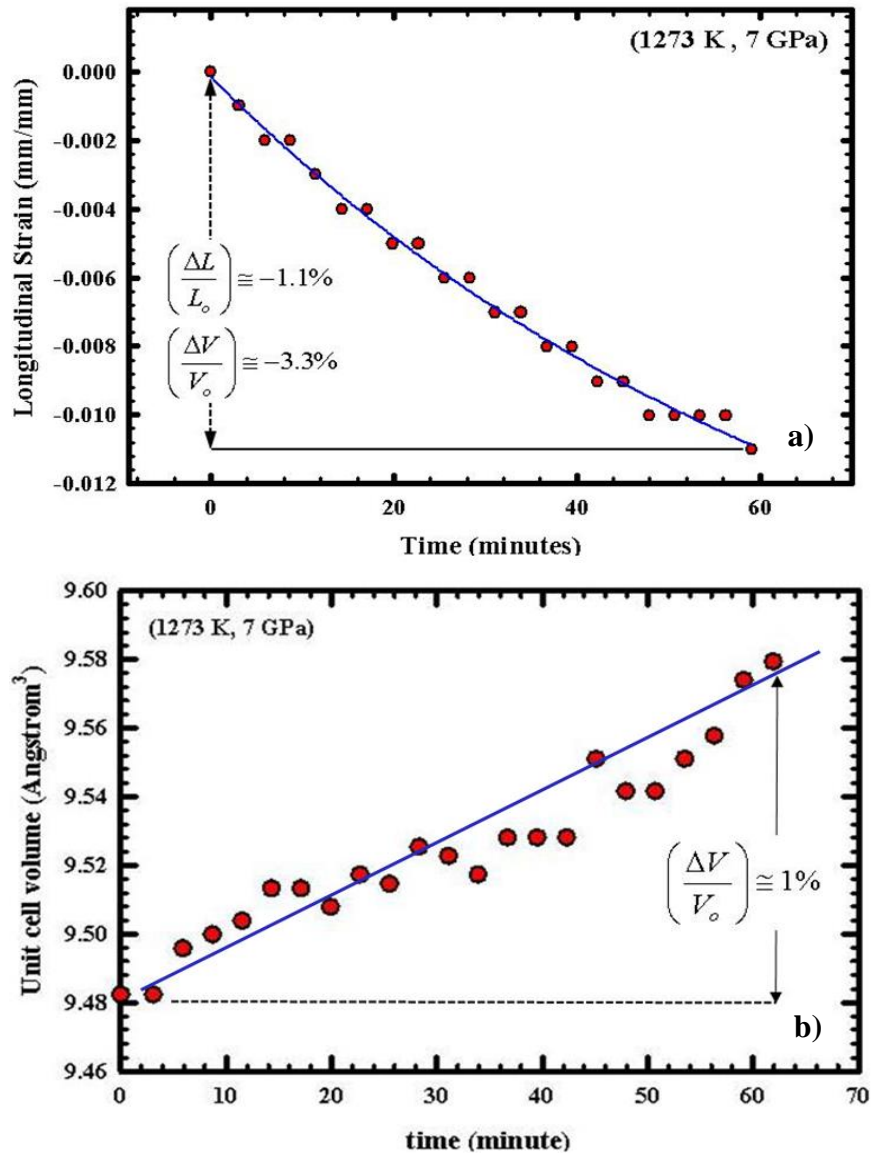
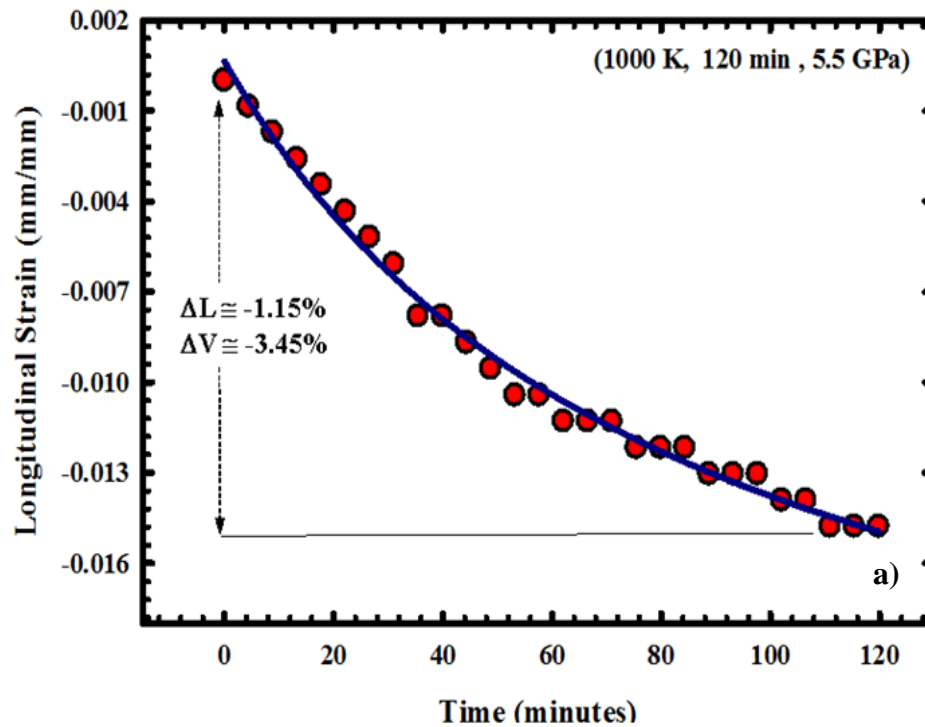


Figure 5.4 a) Microscopic shrinkage during isothermal and isobaric soak b) Increase in cubic MgO lattice parameter for 50/50 MgO-Y₂O₃ sample under 7 GPa and 1273 K [8].

Figure 5.5 shows the variation of linear macroscopic shrinkage in 80/20 MgO/Y₂O₃ composite sample which reaches 1.15% to which corresponds 0.87% volumetric expansion strain in the cubic MgO unit cell. Again, one observes no change in the Y₂O₃ unit cell volume [9].

As it was shown in Figures 5.3 and 5.4, the 50/50 MgO/Y₂O₃ sample at 7 GPa has higher macroscopic shrinkage than the sample 50/50 MgO/Y₂O₃ sample at 5.5 GPa, showing that increasing pressure effects densification process. Another remarkable effect on densification process is behavior of different composition content of composite materials, for instance the 80/20 MgO/Y₂O₃ sample at 5.5 GPa shows less shrinkage than the 50/50 MgO/Y₂O₃ sample at 5.5 GPa during densification.



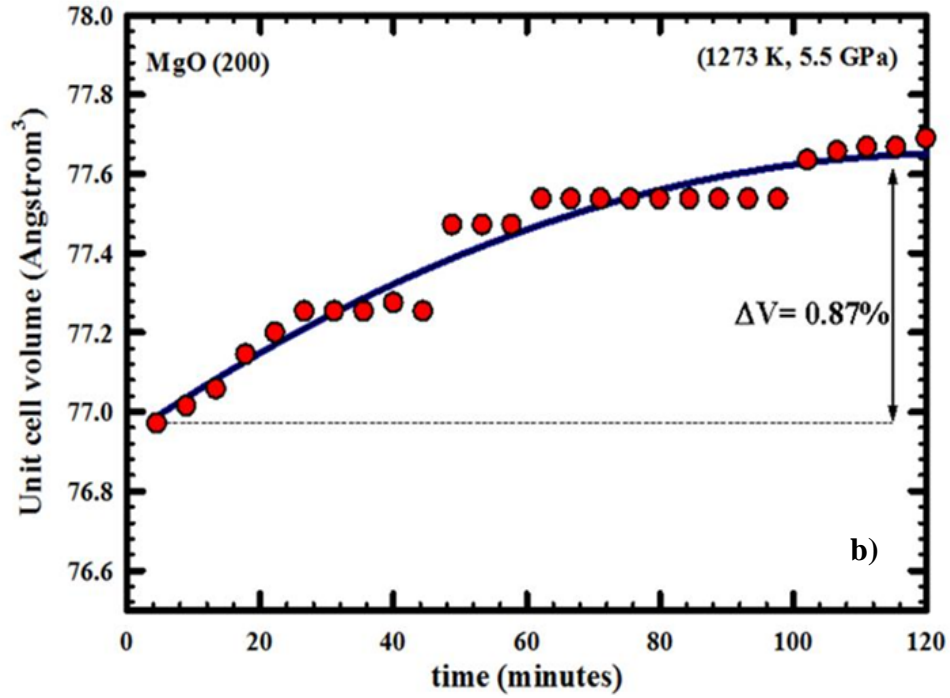


Figure 5.5 a) Microscopic shrinkage b) Volumetric expansion in cubic MgO unit cell under 5.5 GPa and 1273 K for 80/20 MgO-Y₂O₃ sample [9].

Table 5.1 summarized the results obtained in the high pressure studies on the MgO-Y₂O₃ system. The data shows a very curious result: When all samples are cooled to room temperature and decompressed to 1 atm, the volumetric strain in MgO phase of composite materials remains around 0.68%. This shows that a metastable solid solution can be isolated at room temperature due to sluggish precipitation kinetics [7-9].

Table 5.1 Tabulated data calculated by considering cubic MgO(200) peak of first virgin sample as a reference point [7-9].

Composition & Pressure	After sintering		After cooling to RT & decompression	
	Linear Strain in MgO @ 1273 K	Volumetric Strain in MgO @ 1273 K	Linear Strain in MgO @ 298 K 1 atm	Volumetric Strain in MgO @ 298 K 1 atm
50/50 @ 5.5 GPa	0.28%	0.83%	0.22%	0.67%
50/50 @ 7.0 GPa	0.33%	~1.0%	0.23%	0.68%
80/20 @ 5.5 GPa	0.33%	~1.0%	0.23%	0.68%

5.1.2.2. Phase Evolution of MgO-Y₂O₃ System

The phase evolution of MgO-Y₂O₃ nanocomposite system will be elaborated on next. Figure 5.6a shows the X-ray spectrum at room temperature and 1 atmosphere where MgO of Fm-3m and Y₂O₃ of Ia-3 space group symmetry are observed [8]. After applying 7 GPa hydrostatic pressure on sample at room temperature, peaks belonging to monoclinic and hexagonal phases of Y₂O₃ appear while cubic Y₂O₃ and MgO reflections are still observed as shown in Figure 5.6b [8, 87].

As the temperature is increased to 1273 K at 120 K/min, the four-phase co-existence first observed at (293 K, 7GPa) does not change (See Figure 5.7a) [8]. Moreover, increasing temperature results crystallinity because the peaks of all phases become sharper. The increase in crystallinity also implies that the monoclinic and hexagonal volume amounts are increased in this composite system.

During isobaric and isothermal hold at (1273 K, 7 GPa), x-ray spectra were obtained in 3 min intervals, during which no changes in the phase assemblage is observed (See Figure 5.8) [8]. No additional phase and no relative intensity changes are obtained in densification process. The temperature is decreased to 298 K by 200K/min intervals. After cooling and decompressing the system to (298 K, 1 atm), four-phase coexistence is still observed. The results show that the thermokinetic cycle used in this study yields metastable four phases coexistence in MgO-Y₂O₃ nanocomposite system. According to the Gibbs phase rule ($F + P = C + 2$ with F =degree of freedom, P =number of phases, C =number of components) [88] a system with 4 co-existing phases should have zero degrees of freedom because $P=4$ and $C=2$ [89]. However, the change in temperature and pressure does not yield any appearance or disappearance of any new phases even after 240 hours aging period (as determined by additional x-ray work at the X17-B1 beamline with photon energy up to 200 keV; see Fig. 5.9) which leads one to conclude that the four-phase equilibrium is kinetically stabilized at room temperature [8].

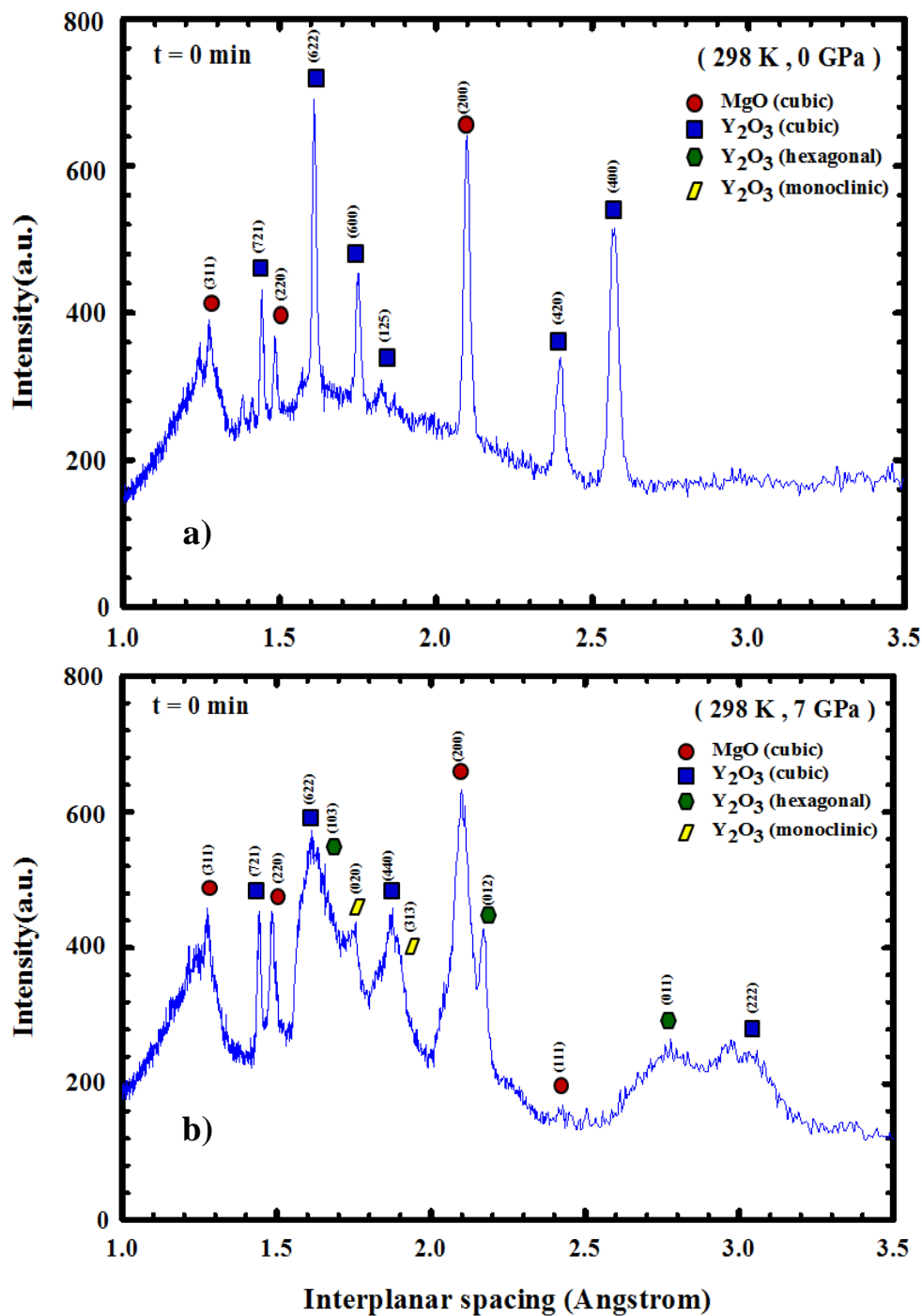


Figure 5.6 a) Initial spectrum from pure MgO-Y₂O₃ at ambient condition b) X-ray spectrum after applying 7 GPa at 298 K [8].

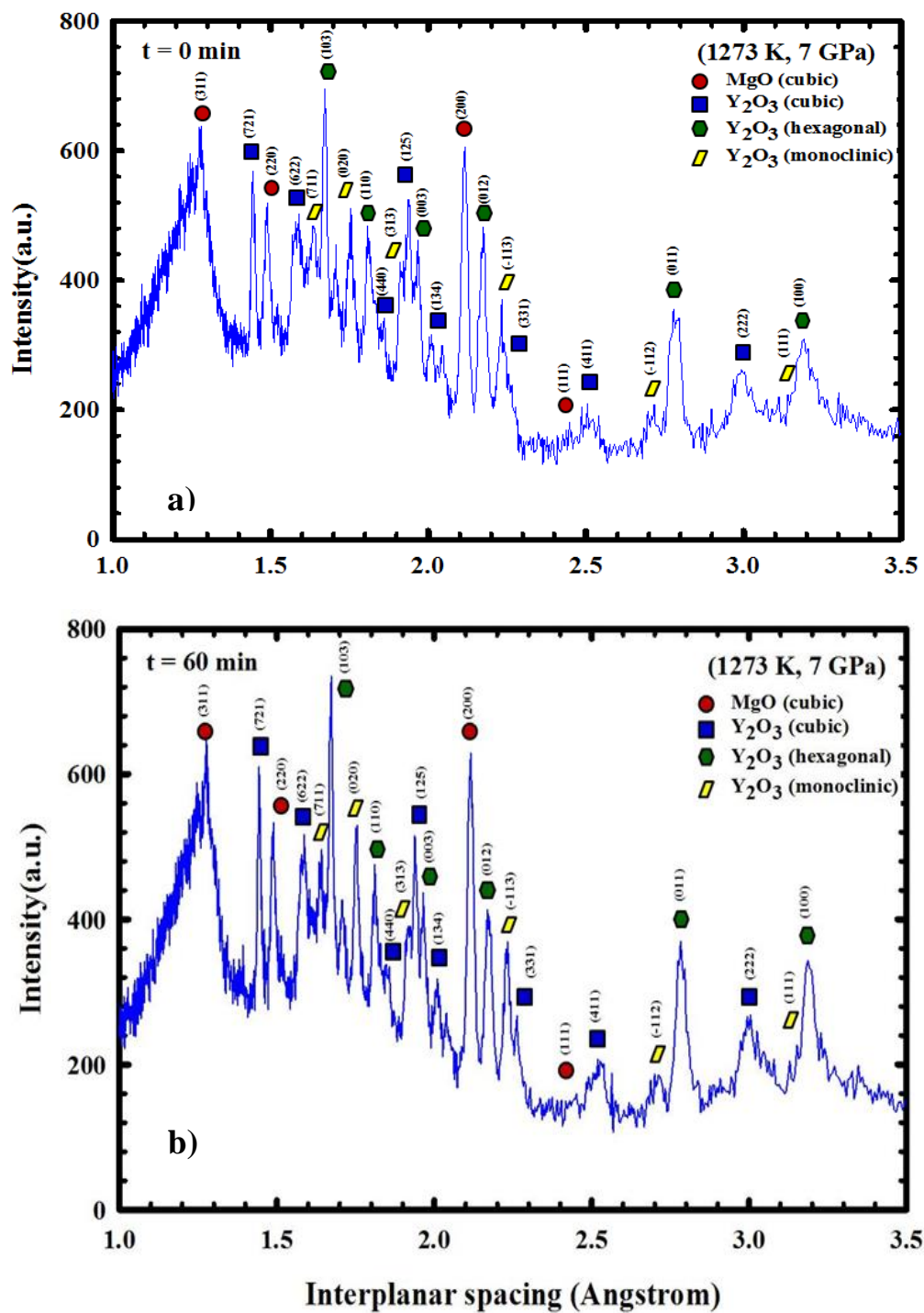


Figure 5.7 a) Spectrum at the beginning of sintering at 1273 K and 7 GPa, b) Spectrum taken at the end of the sintering after 60 min soak [8].

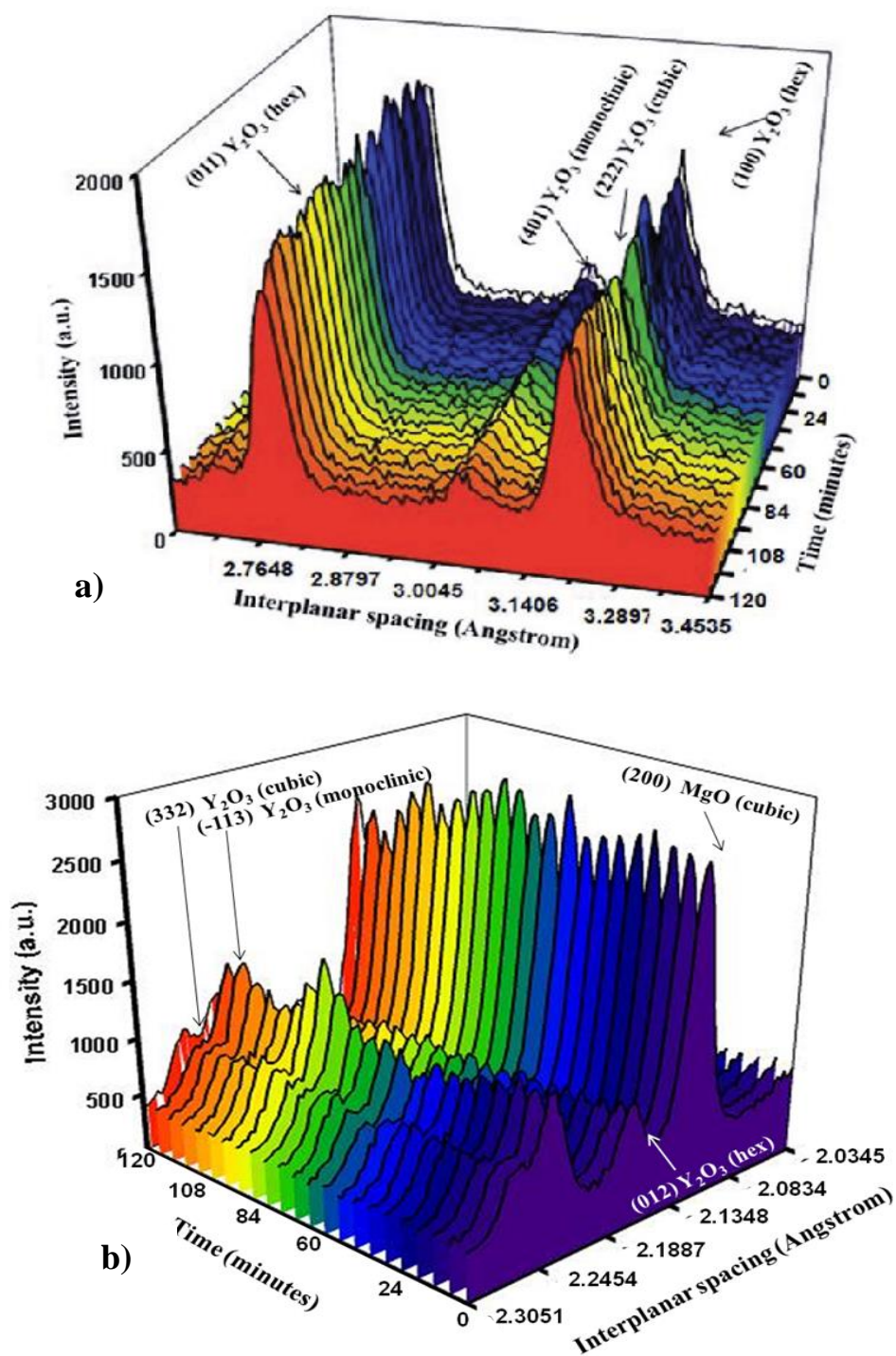


Figure 5.8 X-ray spectra taken during isobaric and isothermal hold with 3 min intervals at 1273 K [8].

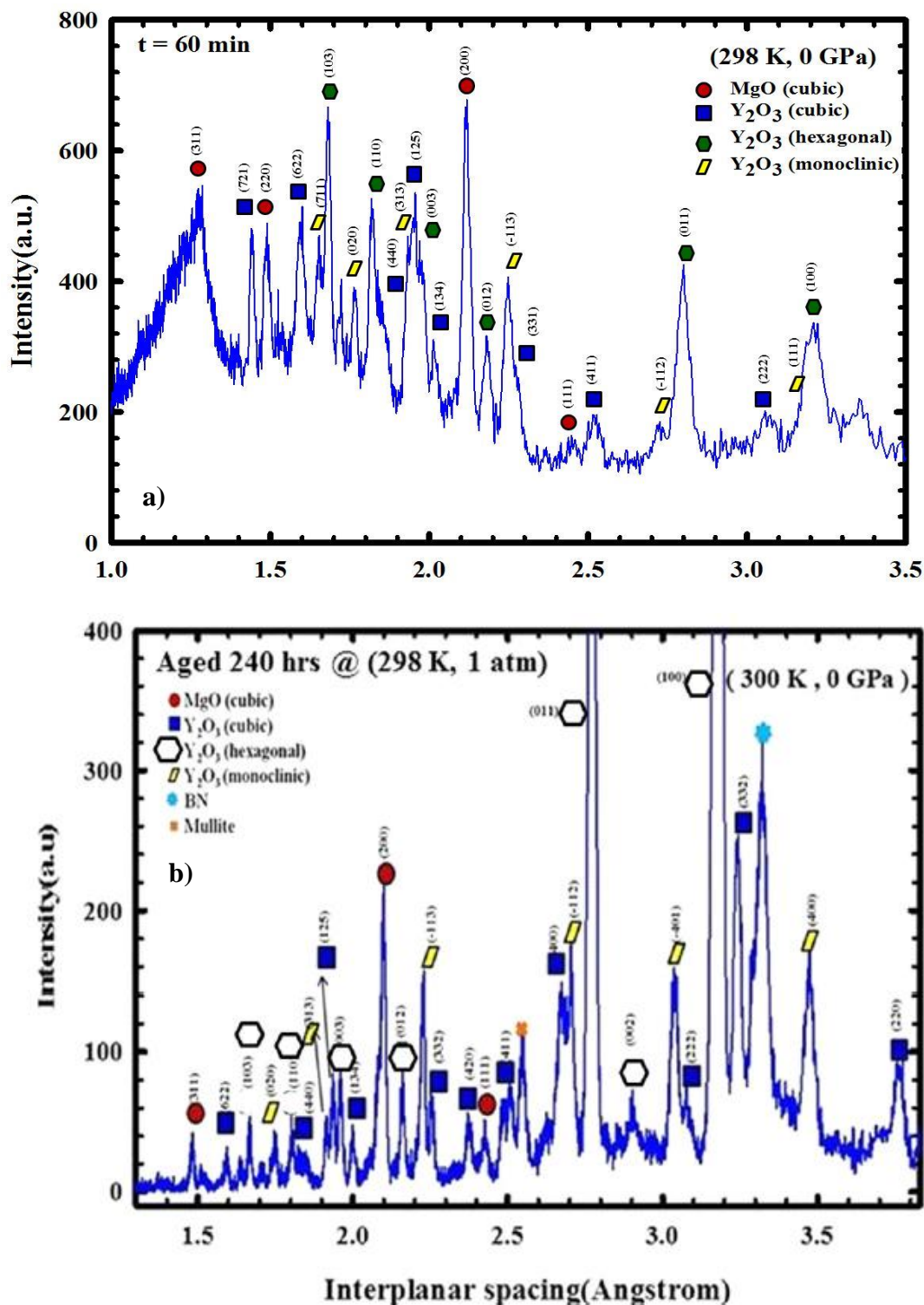


Figure 5.9 a) Spectrum taken at the end of the cycle b) Spectrum taken at X17-B1 beamline after aging for 240 hours [8].

As shown in Figure 5.10a and 5.10b, all four phases remains metastable at the end of the thermokinetic cycle in the 50/50 system [7, 9]. For the 80/20 sample, the intensity of the Y_2O_3 phase peaks lower but here, the four-phase metastable equilibrium is also retained. In light of foregoing results, the thermokinetic cycle used in this study shows that solid solubility can be forced upon a system which shows no solubility otherwise. And once such forced solubility is induced, it remains metastably at room temperature. What is peculiar is that the pressure induced allotropic transformations also remain metastably at room temperature [7-9].

5.1.2.3. Theoretical Discussion of Thermokinetic Densification Results

The volume increasing in MgO unit cell cannot be explained by thermal expansion considerations because the experiments were carried out under isobaric and isothermal conditions. According to the MgO- Y_2O_3 phase diagram, there is no solid solubility up to 1700 K. However, the results do indicate that Y^{+3} can be dissolved in MgO under high pressure despite large high ionic radii differences between Y^{+3} (89pm) and Mg^{+2} (66pm) [90]. It is obvious that the high pressure and high temperature condition utilized in this study was able to force Y^{+3} into the MgO, resulting in ~1% volumetric expansion. Since the residual volumetric expansion at room temperature and 1 atmosphere pressure is still substantial (~0.7%), one should consider the forced solid solubility as quenched-in from 1273 K to 298 K in the MgO- Y_2O_3 [7-9].

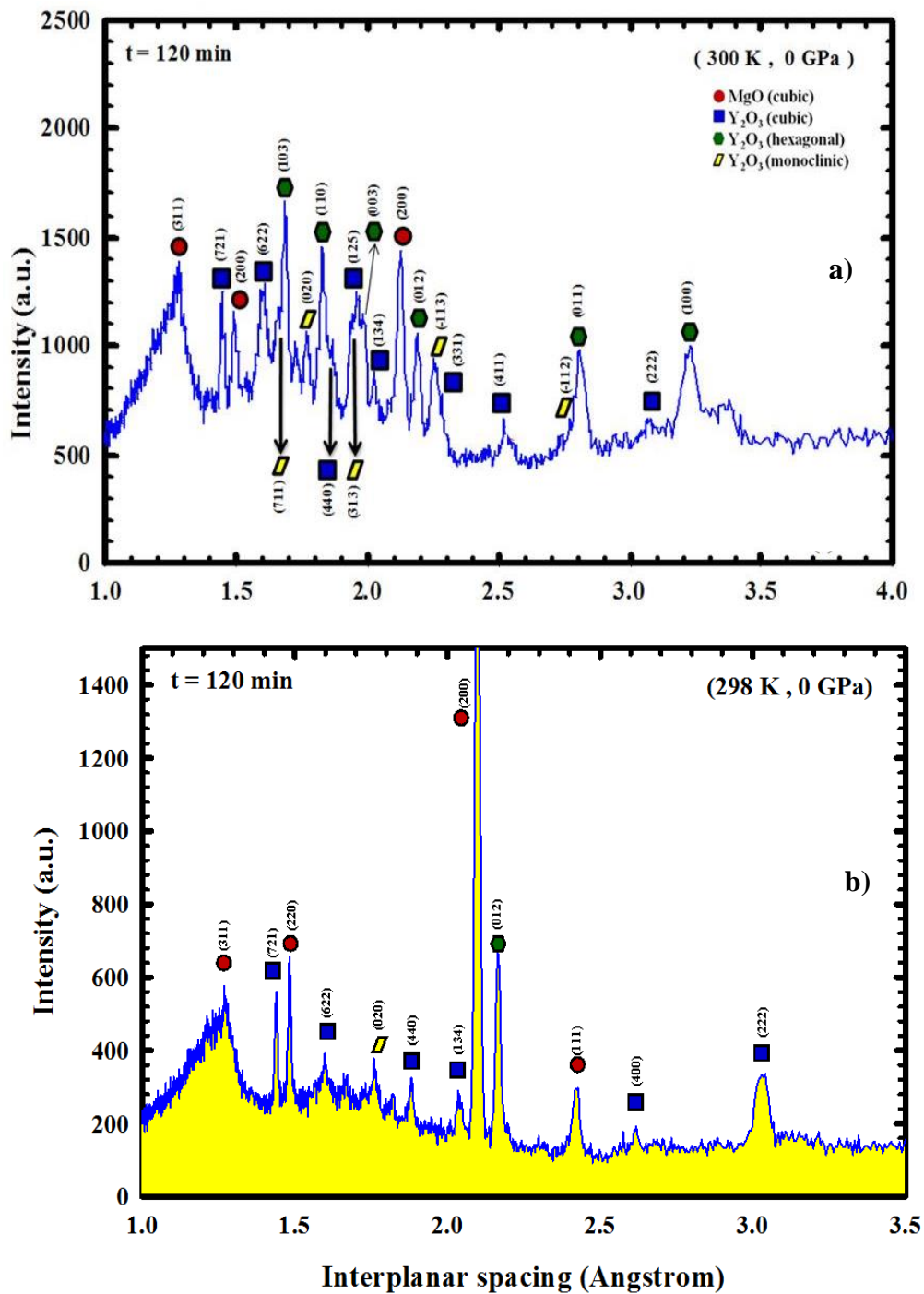


Figure 5.10 X-ray spectra of the MgO- Y_2O_3 systems after the (5.5 GPa, 1273 K, 120 min) thermokinetic cycle: a) 50/50 weight % b) 80/20 weight % [7, 9].

According to thermodynamics of solutions, the partial molar Gibbs free energy of mixing $\Delta\bar{G}_i^m$ for a given constituent in solution is [86, 89];

$$\Delta\bar{G}_i^m = N_A k_B T \ln(a_i) \quad (5.1)$$

where k_B is Boltzmann constant, N_A is Avogadro's number, T is the absolute temperature, and a_i is the chemical activity of species i in the solution of interest (here, i is Y_2O_3 with MgO as the matrix). The pressure and temperature dependence of $\Delta\bar{G}_i^m$ is expressed in its most general form as;

$$\Delta\bar{G}_i^m = \Delta\bar{V}_i^m dP - \Delta\bar{S}_i^m dT \quad (5.2)$$

where $\Delta\bar{V}_i^m$ is partial molar volume and $\Delta\bar{S}_i^m$ is entropy of mixing. The isothermal pressure dependence of can be extracted from Eq. (2) by following;

$$\left(\frac{\partial\Delta\bar{G}_i^m}{\partial P}\right)_T = \Delta\bar{V}_i^m \quad (5.3)$$

by combining Eqs. (1) and (3), the following integral equation can be acquired [84, 86, 87];

$$\int_{a_i@P_0}^{a_i@P} \partial\ln(a_i) = \left(\frac{1}{N_A k_B T}\right) \int_{P_0}^P \Delta\bar{V}_i^m \partial P \quad (5.4)$$

which is integrated once, gives the pressure dependence of activity a_i ;

$$a_i(P) = \exp\left(\frac{\Delta\bar{V}_i^m}{N_A k_B T}\right) \quad (5.5)$$

where $P_0 = 1$ atm and with consideration $P \gg P_0$, $\Delta P \cong P$ can be assumed. According to phase diagram, under ambient condition, dissolving Y_2O_3 in MgO is considered to be none which means activity $a_i(P_0)=1$. After the dissolution of Y^{+3} in MgO unit cell during 60 min densification process, the pressure dependence of chemical activity has to be

$a_i(P) < 1$. By assuming $\Delta \bar{V}_i^m$ is not a function of pressure, we infer that $\Delta \bar{V}_i^m < 0$ per Eq. 5.3, so that one has $\bar{V}_i < \bar{V}_i^0$ because $\Delta \bar{V}_i^m = \bar{V}_i - \bar{V}_i^0$ [86, 89], which indicates that partial molar volume (\bar{V}_i) of Y_2O_3 dissolved in MgO lattice smaller than in its pure form \bar{V}_i^0 . Since MgO has a close packed face centered cubic structure, Y^{3+} dissolution should be on substitutional sites and not on interstitial sites [91]. Due to charge neutrality conditions, substitution of Y^{3+} at Mg^{2+} sites should create vacancies [92]. Then, the following defect formula has to hold

$$(Mg_{1-(3x/2)}^{2+}, Y_x^{3+}, V_{x/2}^{Mg}) O, \quad (5.6)$$

where x mole fraction of Y^{3+} , and V^{Mg} is Mg^{+2} vacancy.

In light of the foregoing discussion, the following phenomenological model is proposed for the observed unit cell expansion of MgO. Figure 5.11 [8] shows that the interaction between Mg^{2+} and O^{2-} is absent whenever a Mg^{2+} vacancy is present due to substitution of Y^{3+} . The electrostatic interaction between O^{2-} ions appears due to the vacancy (see Fig. 11 below for $\alpha_1 - \alpha_4$) where O^{2-} quartets need to repel per Coulomb's law [93].

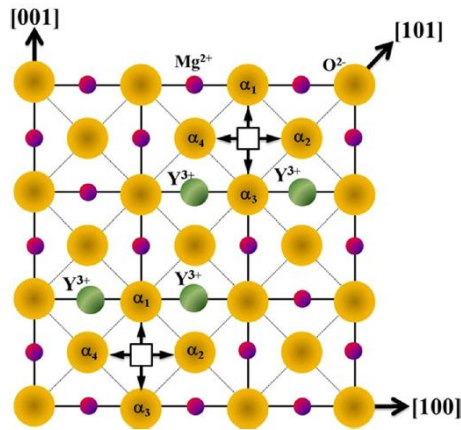


Figure 5.11 The defect model for Y^{3+} dissolution in cubic MgO structure at high pressures [8].

The expansive volumetric strain (u_{elec}) due to local electric field and the elastic volumetric misfit strain (u_{sub}) due to substitution of larger Y^{3+} ions with smaller Mg^{2+} ions can be counted as causes for the volumetric expansion in MgO unit cell. In addition to these strains, the MgO- Y_2O_3 system undergoes volumetric shrinkage (about 3%) during isobaric and isothermal hold, so other elastic strains can be included in the analysis: Elastic strains (u_{sin}) due differential sintering mismatch, strain ($u_{\Delta\alpha}$) due to thermal expansion coefficient mismatch, and strain ($u_{\Delta K}$) due to bulk moduli (K) mismatch [8]. In a multiphase system, differential sintering mismatch becomes pronounced when each phase has substantially different grain size. That is so because the excess surface free energy, which is inversely proportion with grain size, is the driving force for sintering. The contribution of u_{sin} to all obtained strain can be omitted for the MgO- Y_2O_3 system because it consists of a mono-modal particle size distribution centering around 90 nm median particle size [8].

The differences of thermal expansion coefficient between MgO ($\alpha_{\text{MgO}} = 16.0 \times 10^{-6} \text{ K}^{-1}$) and Y_2O_3 ($\alpha_{\text{Y}_2\text{O}_3} = 8.1 \times 10^{-6} \text{ K}^{-1}$) [94] is substantial. Therefore, the thermal expansion coefficient mismatch produces compression effect on MgO unit cell even though volumetric expansion is observed on it. Furthermore, the dK/dT (K: bulk modulus) values for MgO and Y_2O_3 are -31.5 and - 17.0 MPa/C, respectively, which gives a bulk modulus mismatch ~15% ($K_{\text{MgO}} = 149.5$ and $K_{\text{Y}_2\text{O}_3} = 132.5$ GPa at 1273 K), which should place MgO under tension. As all strains are additive [95], the contributions can be summed up as $u_{\Sigma} = u_{\text{sub}} + u_{\text{elec}} + u_{\Delta\alpha} + u_{\Delta K}$ with $(u_{\text{sub}} + u_{\text{elec}}) > (u_{\Delta\alpha} + u_{\Delta K})$ [8].

5.2. Electric Field Assisted Densification Study

In this section, the results pertaining to the electric field effects on the flash sintering of 8 % $\text{Y}_2\text{O}_3\text{-ZrO}_2$ (8YSZ) will be presented. Figure 5.12 represents the spectrum taken along the vertical axis (yr) of the hot stage used in X17-B1 beamline with 100 μm step size (see Fig. 4.2) to set the gauge volume exactly at the body center of the sample [7-10]. The yr axis is perpendicular to the surface of the specimen that has the geometry of a pellet. The spectra at the top and bottom of sample is belong to ceramic insulator plates and in between there is the specimen. There platinum electrodes also contribute 2 major reflections as they are few hundred microns in thickness with two major reflections [10, 84]. The spectra at the very middle of Figure 5.12 belong to 8 % $\text{Y}_2\text{O}_3\text{-ZrO}_2$ sample where one observes all major reflections.

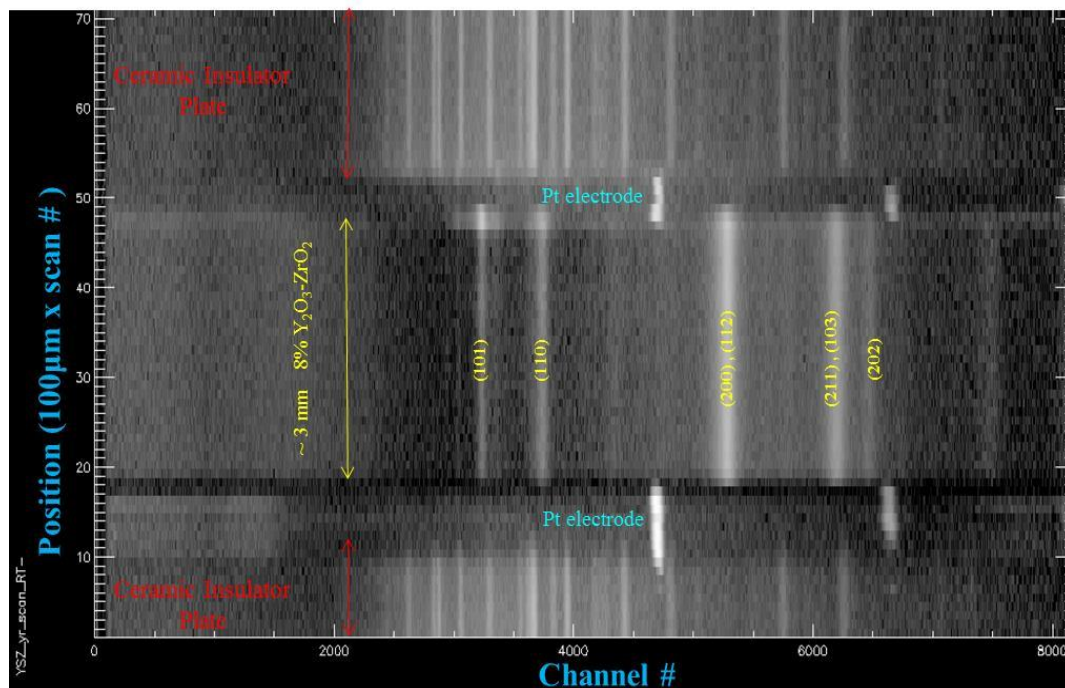


Figure 5.12 Position dependence spectra, taken along yr axis of the hot stage.

Here the gauge volume was placed to the body center of the 8 % $\text{Y}_2\text{O}_3\text{-ZrO}_2$ sample and data was collected with 1 sec intervals during nonisothermal (with 0.15 $^\circ\text{C}/\text{sec}$) sintering study under 215 V/cm dc. Such a high temporal is unprecedented and led to the collection of >3000 spectra in a single experiment that is a record in the NSLS and outperforms any other study in the realm of flash sintering [7-10]. The specimen seen in Fig. 5.12 is 12 mm diameter disc with 2.7 mm thickness that was prepared by uniaxial cold pressing without binder. Initial particle size of green dense sample is around 200 nm and exhibits tetragonal unit cell symmetry [10].

Figure 5.13 depicts the current response of the system under an electric field of 215 C/cm as it is heated with a heating rate of 0.15 $^\circ\text{C}/\text{sec}$). One observes no current draw is observed until the system temperature reached 876 $^\circ\text{C}$. After this point, one observes a leakage current thorough the sample (~ 0.3 A) in Fig. 5.13. As the system temperature is increased further, the amount of current draw increases and reaches a maximum of 3 amps at 905 $^\circ\text{C}$ [10]. The maximum current draw at 905 $^\circ\text{C}$ results in an instantaneous power absorption of 513 W/cm^3 [96]. The time space from 876-905 $^\circ\text{C}$ is only 199 seconds. The rapid draw to 905 $^\circ\text{C}$ is accompanied by a rapid increase in the density of the specimen from 55 % to 97 %, after which the current draw is stops.

What is peculiar about the observed behavior is actually the shortness of the sintering time and not the reduction in sintering temperature. It is possible to reduce the sintering temperature of a given ceramic by liquid phase sintering which is accomplished by forming a small amount of liquid phase at the particle-particle contacts. However, no liquid phase sintering process results in the reduction in the sintering temperature by at least one order of magnitude as is the case in flash sintering, i.e. 1400 $^\circ\text{C}$ / 120 min) vs.

905 °C / 3 min. Therefore, we cannot explain the observed sintering behavior by simple mechanisms such as Joule heating even if we ascribed high internal temperatures to the specimens [97]. Therefore, one is led to believe that the current draw resulting in a peak power density of 513 W/cm³ at 905 °C is coupled to mass transport that is of electrochemical origin such as electromigration in addition to typical Fickian diffusion.

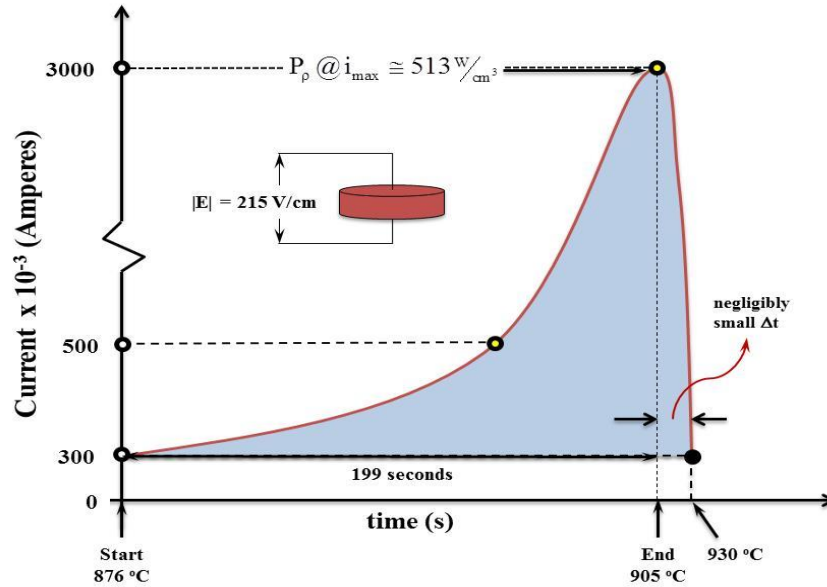


Figure 5.13 Time dependence current draw by 8% Y₂O₃-ZrO₂ during flash sintering between 876 °C and 930 °C [10].

In Fig. 5.14, the behavior of lattice parameters of the tetragonal unit cell is depicted while the specimens were heated with 0.15 °C/sec, and under an electric field of 215 V/cm in the parallel plate capacitor geometry. The monotonous increase in the tetragonal lattice parameter up to ~820 °C is due to thermal expansion [10]. A small singularity, which is a deviation from the thermal expansion background, is seen $t > 820$ °C reaching its maximum at 847 °C. Here the current draw is 0.1 Amperes. This hump corresponds to a spontaneous anelastic expansion. In other words, the expansion is the

natural response of the system. One also notes that the system spontaneously relaxes to the baseline for $T > 847^\circ\text{C}$. Another singularity is observed when the system reached 876°C . Here, there is rapid rise in the current draw to 3 A that is accompanied with an anomalous increase unit cell parameter at 905°C . The density of the system reaches 97% at 905°C . For $T > 905^\circ\text{C}$ the current is cut off by the power source used and the system relaxes anelastically to the thermal expansion baseline under zero electric field [10].

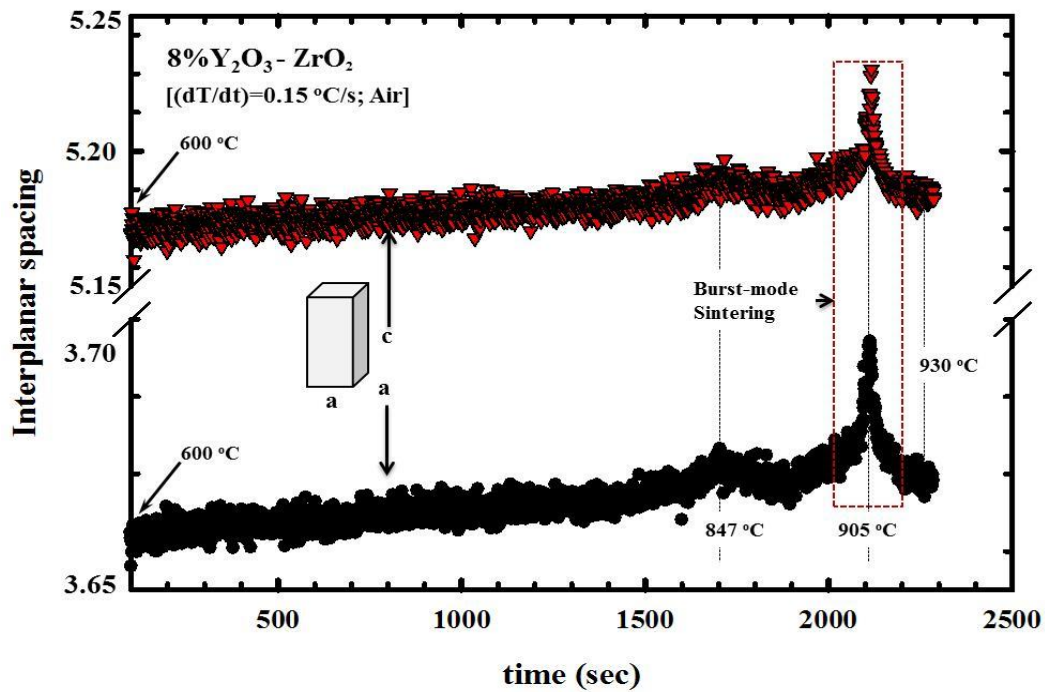


Figure 5.14 Variation of lattice parameters of 8 % $\text{Y}_2\text{O}_3\text{-ZrO}_2$ as a function of time during flash sintering under 215 V/cm and 0.15 $^\circ\text{C/s}$ [10].

The variation of the unit cell volume as a function of time is shown in Fig. 5.15. The current induced unit cell expansions corresponding to the observed singularities at 847 and 905°C are 0.45 and 2.35%, respectively. Firstly, one should refrain from calling

the expansion as volumetric elastic strains because the expansion takes place while charge is flowing through the system, and hence, it is not in equilibrium. Secondly, the reported unit cell expansions are above the thermal expansion baseline which makes them a function of the current passing through the system only. Thirdly, the expansion is a transient phenomenon and so is the densification. The system never reaches steady state which is no Joule heating is observed.

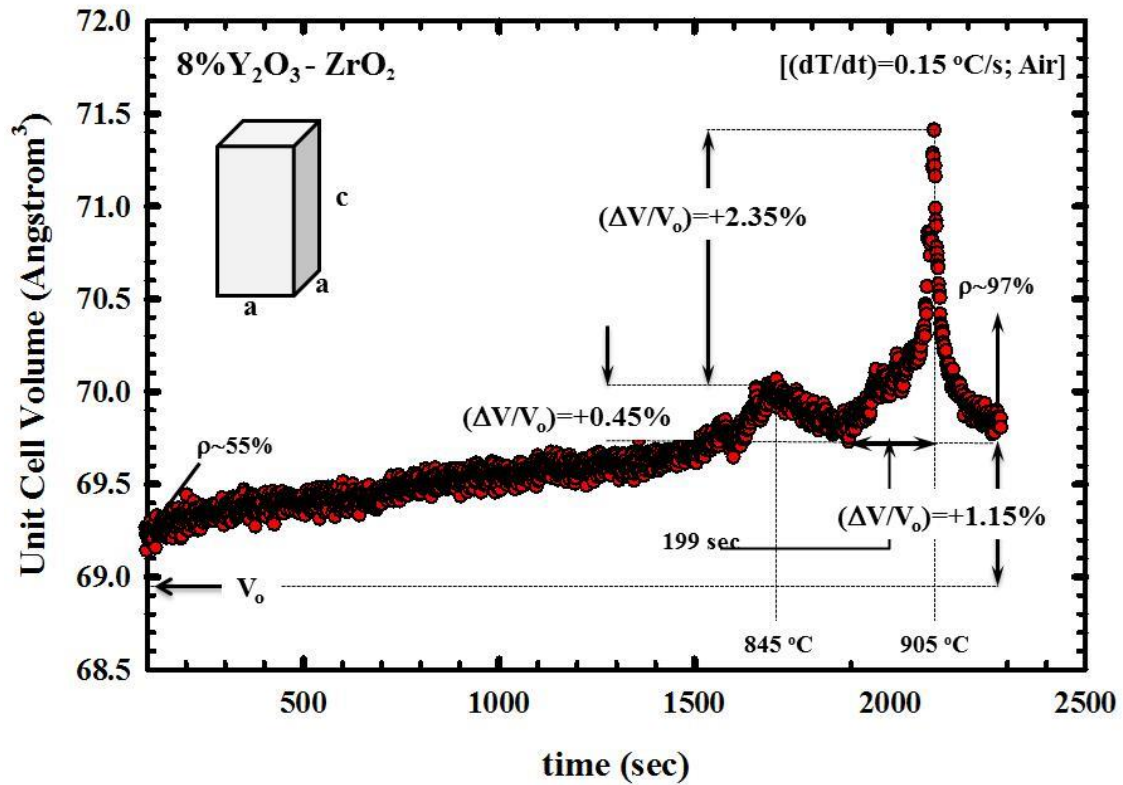


Figure 5.15 Variation of unit cell as a function of time during flash sintering [10].

Figure 5.16 depicts spectra collected from different points at vicinity of the (200)/(112) peak cluster [10]. A close examination of these peaks indicates that there is a shift $\langle 200 \rangle$ and $\langle 112 \rangle$ crystallographic direction when the electric field is applied, but as soon as the electric field is cut off, the peaks relax back their original positions. There is no polymorphic phase transition observed during this phenomenon as shown in Figure 5.16. Therefore, one has to conclude that the observed anomalous unit cell expansion is not due to a phase transition where there is a change in molar volume of the system.

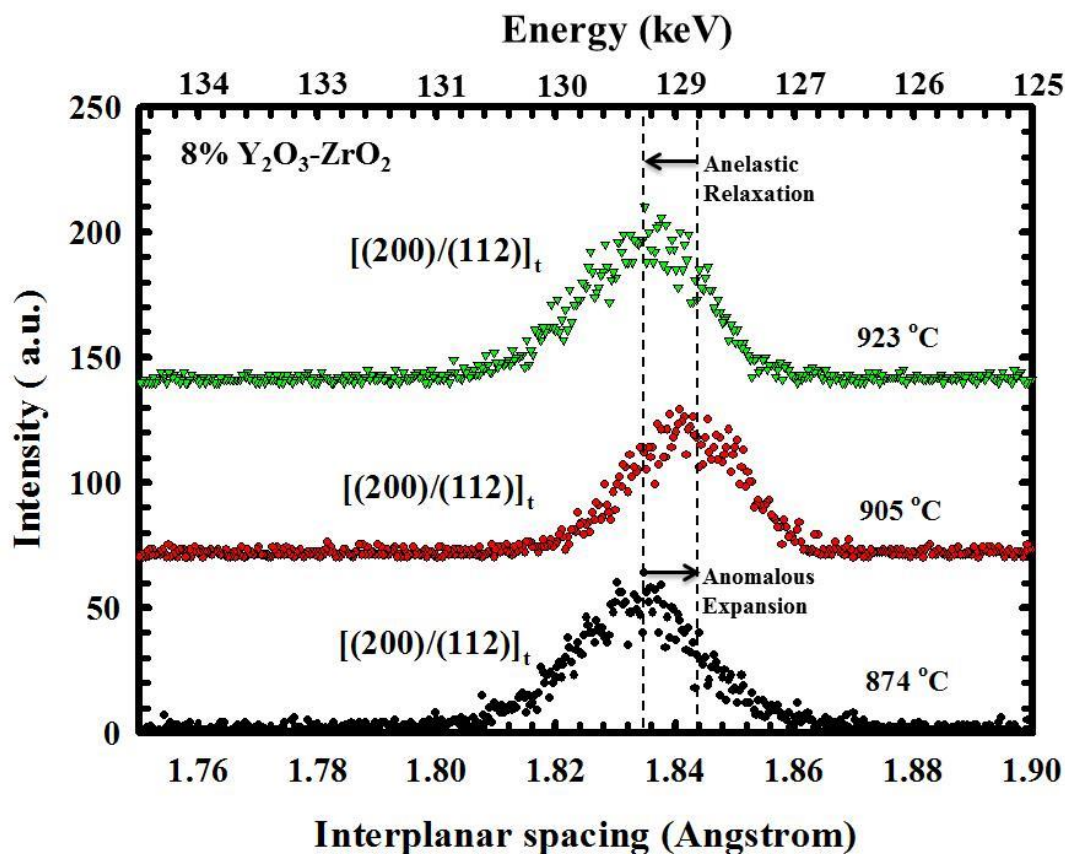


Figure 5.16 EDXRD spectrum collected at 874 °C, 905 °C, and 923 °C to show expansion due to electric field [10].

Figure 5.17 shows the variation line broadening data under 215 V/cm electric field with 0.15 °C heating rate as a function of time [10]. The existence of any distinctive behavior at the FWHM indicates that defect process is occurred as time dependence under the applied electric field when the system reaches 905 °C at which we also observe charge and mass transport phenomena, concurrently [10]. The system's governing defects are oxygen vacancies. Therefore, one expects that electronic behavior and mass transport phenomena are coupled in conjunction with defect process during flash densification process due to singularity seen at peak breadth [10].

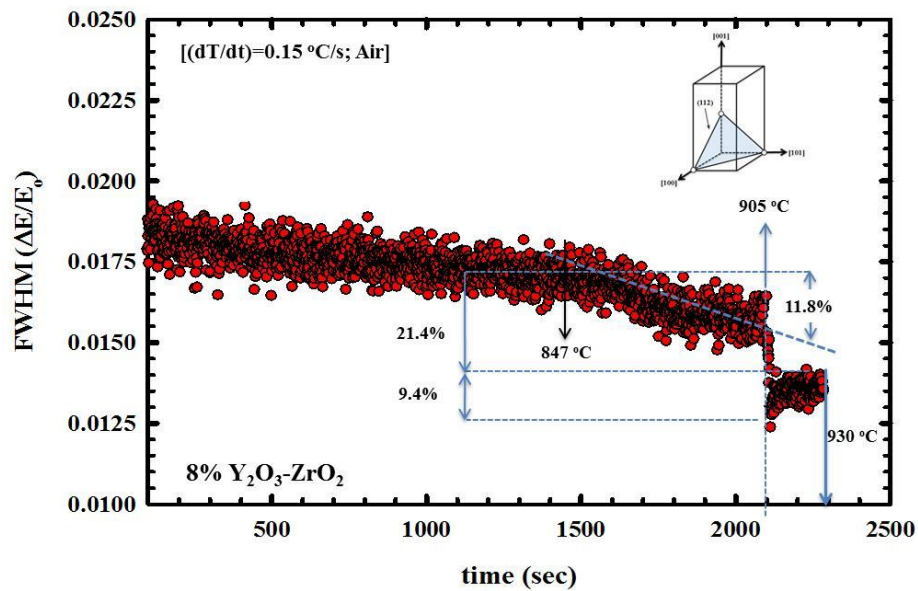


Figure 5.17 Peak breadth variations as a function of time during flash sintering [10].

To understand the physical meaning of peak breadth behavior in x-ray crystallography, line broadening analyses were carried out that will be presented in the Section 5.2.2.

As elaborated on in the foregoing discussion, once the flash sintering cycle is terminated 905 °C under 215 V/cm electric field, a 97% dense was obtained. A comparison of the x-ray spectra taken at room temperature before and after flash sintering, the peak intensity increases almost forty percent as the peak breadth decreases ~50% percent as shown in Figure 5.18 [10]. The pattern taken at room temperature after flash densification becomes sharper with high peak intensity which is indicative of high density and crystallinity. Given these experimental findings, one has to conclude that what is observed is a new phenomenon with results in the densification of a crystalline material under electrochemical transport mechanisms of an unknown nature. Here, the mode in which densification occurs is in the form of a burst [10, 84, 97]. Hence, the term burst mode densification might very well be more appropriate to define the transient phenomenon which is called flash sintering.

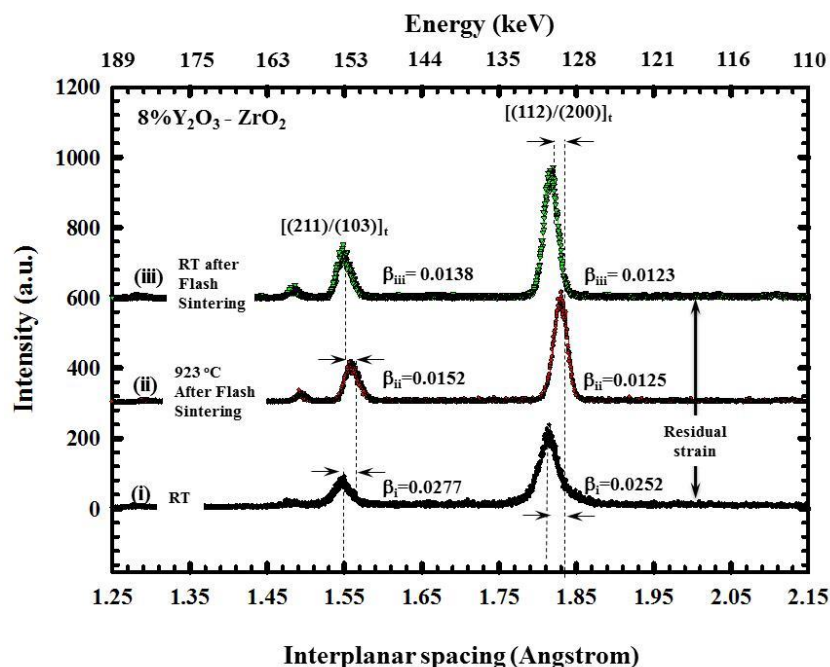


Figure 5.18 EDXRD spectrum collected at RT (green dense), 905 °C, and RT (after sintering) to show expansion due to electric field [10].

5.2.1. Electric Field Effect on Burst mode Densification Temperature and Process

Burst mode densification experiment at temperatures ranging between 800 °C – 900 °C were performed with identical samples on which different electric fields are applied. As the electric field on sample is increased, the burst temperature decreased, shown in Figure 5.19. During burst mode densification, current draw mechanism is observed spontaneously and we let the system reach the max current draw itself. The amount of current draw through samples is a function of the magnitude of the electric field. The maximum current draw was found to occur under 183 V/cm at 841 °C. The data in hand suggests that 183 V/cm is best for burst mode densification electric field at 841 °C. While the exact mechanism of the observed optimum value is not known, one is inclined to think that at 841 °C, resistances of the specimen matches the internal resistance of the power source enabling maximum power transfer from the source to the system.

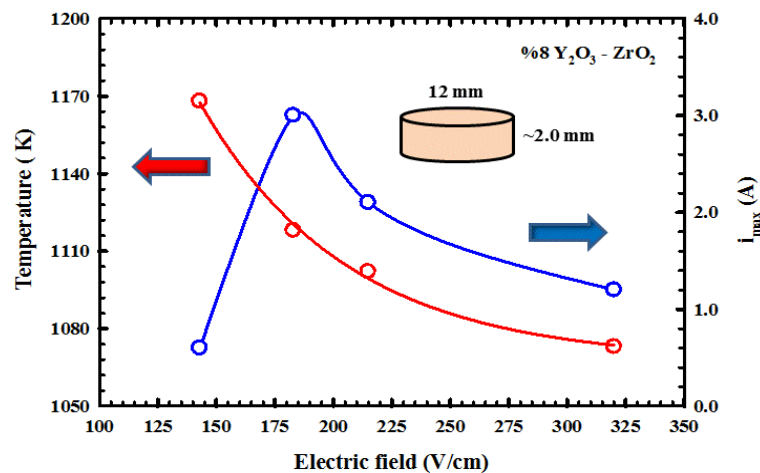


Figure 5.19 Electric field effect on thermally activated runaway on flash sintering temperature and current draw.

However, this resistance matching hypothesis has its weakness as the time frame for densification is considered. We do not see any discernible variation in the sintering time with electric field magnitude for as long as the field is high enough to induce the burst.

The variation of the tetragonal unit cell volume of 8% $\text{Y}_2\text{O}_3\text{-ZrO}_2$ with applied electric field magnitude is shown Figure 5.20. Here, the specimens were heated to 900 °C with a heating rate of 20 °C/min. At all applied field magnitude, there are some common trends in the material's response: (1) monotonic increase due to thermal expansion, (2) transient anelastic anomalous unit cell expansion take places in ~25- 35 sec, concurrently happening with current draw mechanism, (3) anelastic relaxation takes ~100 sec right after transient phenomena, (4) the monotonic increase for all samples match volumetric thermal expansion which was calculated as $3.08 \times 10^{-6} \text{ }^\circ\text{C}^{-1}$ in the RT-900C range, and (5) at least one major singularity is observed in the variation of time dependent unit cell volume at different temperatures as a function of electric field for all samples.

The expansion at the unit cell volume becomes maximum at the temperature 841 °C with 183V/cm electric field where the current draw also becomes a maximum with 3 A. The lowest current draw was observed with 0.8 amps at 892 °C under 143 V/cm to which corresponds the lowest unit cell expansion. The observed increase in temperature is only 40-50 °C which is why Joule heating is no considered here. What is peculiar is that the unit cell expansion scale directly with the current passing through the system up to a certain optimum electric field. This suggests that the electric field cannot be arbitrarily increased in an effort to decrease the onset temperature of flash sintering. In fact, if the electric field were arbitrarily increased one would induce Joule heating in the system and the process would be nothing but a spark plasma sintering process. Hence,

flash sintering differs in a sense that it occurs over a narrow range of electric field and precedes Joule heating which is a steady state phenomenon. As a result, one is led to conclude that flash sintering is a transient state phenomenon preceding Joule heating.

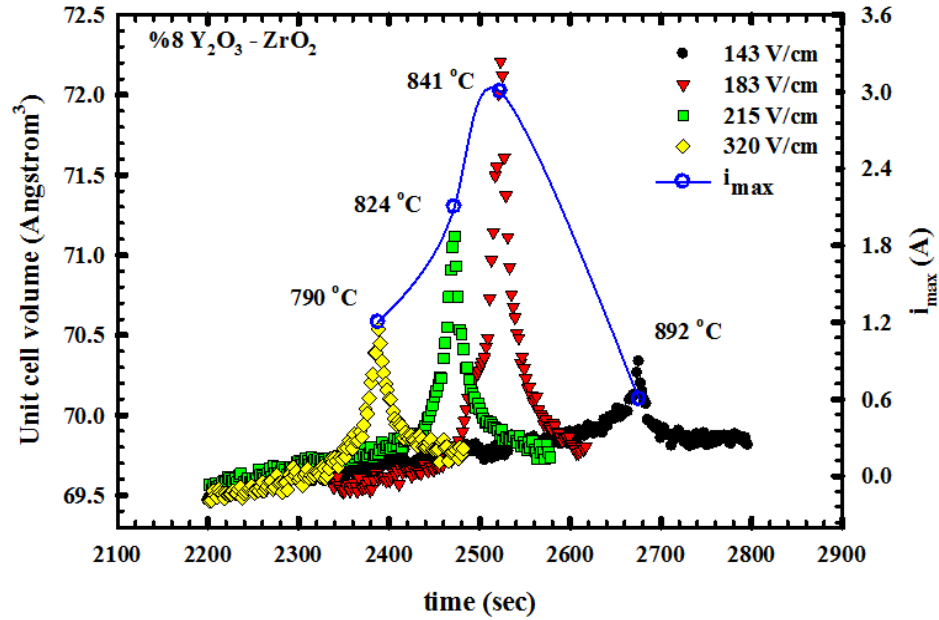


Figure 5.20 Unit cell variation 8% $\text{Y}_2\text{O}_3\text{-ZrO}_2$ samples as a function of time under different electric field.

The variation of the $\langle 101 \rangle$ peak width with time and as a function of electric field is depicted Fig. 5.21. At all electric field magnitudes, three apparent stages are observed. In the first stage, a slight monotonous decrease with increasing temperature is seen. The second stage depicts a singularity in the peak width as defined by a sharp decrease when there is current draw. In the third stage, the monotonic behavior continues.

According to theory of kinematical scattering, two factors cause X-ray diffraction peaks to broaden; crystallite size or lattice defects [79, 98]. During densification process under thermal and electric field, mass transport in the system is controlled by the

migration of oxygen vacancies. Hence, the clustering, de-clustering, and changes in concentration are expected to have a signature in the peak width which we indeed observe (see Fig. 5.21). Therefore, the instantaneous change at the peak width during densification process under thermal and electric field should be attributed to both crystallite size increase and defects rearrangements which are consequences of mass transport in a solid electrolyte [10]. What is most significant is the fact that the

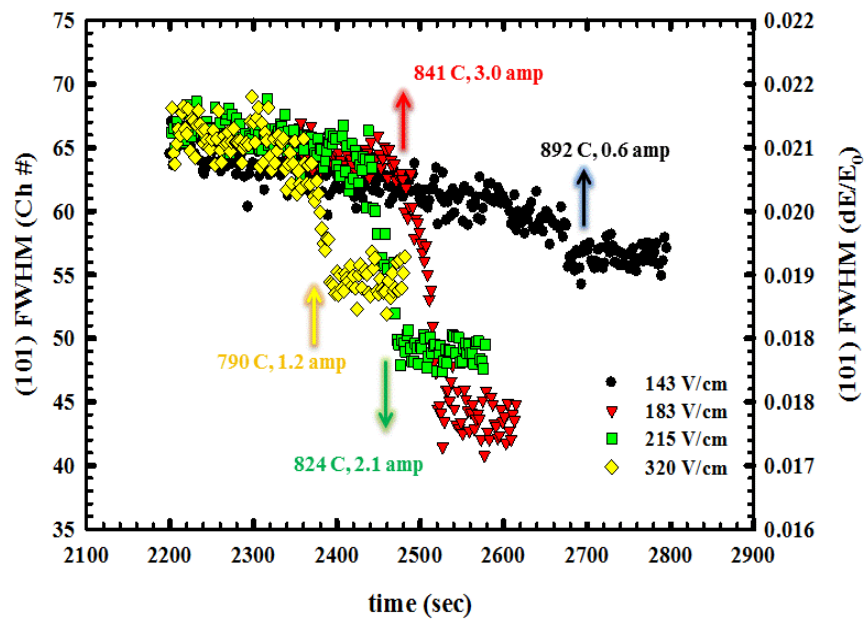


Figure 5.21 8% $\text{Y}_2\text{O}_3\text{-ZrO}_2$ samples' peak breadths respond as a function of time under electric and thermal field.

anomalous volumetric expansion and changes in peak width occur exactly over the same temperature range. The decrease in peak width is proportional to the current draw through the system. The maximum decrease in peak width coincides with the maximum current draw (3 A) at 841 °C under 183 V/cm electric field. This suggests that there is a direct correlation between oxygen vacancy transport under the applied electric field in burst

mode densification. However, the reduction in the time scale for densification remains a mystery.

Analysis of SEM micrographs leads one to conclude that the system which received 3 A current is the densest sample with ~97 % density (see Figure 5.22). As seen at the micrograph, which was taken on fracture surface, grain boundary formation has occurred and the system has ~200 nm with a monodisperse distribution.

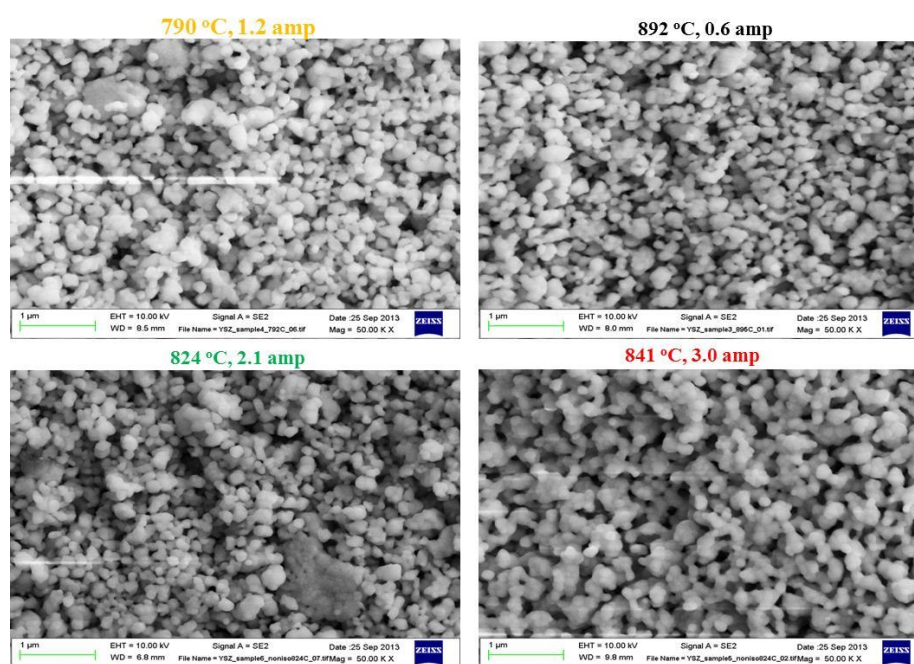


Figure 5.22 SEM images of 8% $\text{Y}_2\text{O}_3\text{-ZrO}_2$ samples after electric and thermal field sintering study.

Table 5.2 summarizes the results obtained of the study on the electric field effects on flash sintering. By using the thermal expansion data, the corresponding fictitious temperature that would cause the observed anomalous expansion is also computed and included in the table. For instance for the 183 V/cm specimen, the internal temperature needs to rise to over 2000 K to reproduce the observed unit cell volume expansion which

is unrealistic. What is perhaps most peculiar is that the flash sintering time seems to be invariant with respect to the applied field magnitude. Moreover, the sintered density varies over a small margin, although the maximum density corresponds to the case where maximum power absorption takes places.

Table 5.2 Tabulated data of flash sintered 8YSZ samples, showing experimental parameters and results.

Sample (E field)	Current Draw(amp)	Burst Temperature (°C)	Volumetric Strain due to Burst mode (RT ref. point)(%)	Calculated Temperature due to Thermal Expansion(ΔT)	Calculated Temperature due to Thermal Expansion	Density (%)
143 V/cm	0.6 amp	892 °C	3.93	1293 K	1318 °C	~95
183 V/cm	3.0 amp	841 °C	6.71	2204 K	2229 °C	~97
215 V/cm	2.1 amp	824 °C	5.09	1674 K	1699 °C	~96
320 V/cm	1.2 amp	792 °C	4.23	1392 K	1417 °C	~95

5.2.2. Line Profile Analysis of Flash Sintering

As the first method of attack, we have used the modified Williamson-Hall method in conjunction with the (101), (110), (112), (200), (103) and (211) reflections' peak position and profile parameters. The peak widths (β) of the reflections were obtained by peak fitting of a pseudo-Voigt profile shape function (PSF), which was then plotted as a function of energy (E^2). As shown in Figure 5.23, the EDXRD variant of the Williamson-Hall equation (See Eq. 1) was then fitted to the data. The correction for instrumental broadening was made using LaB_6 data (see bottom of Figure 5.23) by following standard procedures [76]. As per Eq. (1), the intercept of the β^2 vs. E^2 plot yields $\langle L \rangle$, while the slope gives $\langle u \rangle$. Here, $\langle L \rangle$ and $\langle u \rangle$ were determined at various temperatures during the time evolution of the system under simultaneous applied thermal and electric fields on

the ramp up to 905 °C as well as on the ramp down from 905 °C during which the sample was cooled under zero field.

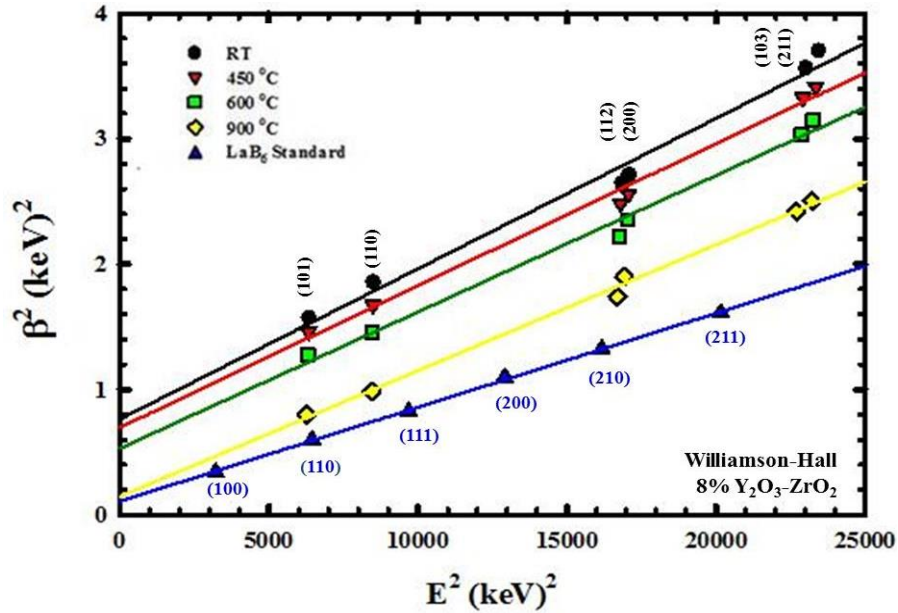


Figure 5.23 The Williamson-Hall plots for determining the isotropic average crystallite size and microstrain from energy dispersive x-ray diffraction data at selected temperatures during the in-situ densification experiment on 8% Y_2O_3 - ZrO_2 .

In Figure 5.24, the evolution of the Williamson-Hall crystallite size is presented at selected times in the ramp-up (0-6000 seconds range). As we reported in the preceding sections, the burst type densification ultimately takes place under nonisothermal conditions over the 876-905 °C intervals in 199 seconds (not 4 shown) at which point the apparent density reached 97% of the x-ray density (measured by the Archimedes method) [10]. The said densification is accompanied by a sharp rise in crystallite size from ~25 nm at (RT, $E=0$ V/cm) to ~120 nm at (905 °C, 215 V/cm), which is followed by relaxation to 40 nm as the temperature is decreased back to RT under zero electric field as per the Williamson-Hall analyses presented herein. Concomitantly, one observes a

decrease in the microstrain from 0.34% at (RT, $E=0$ V/cm) to $\sim 0.25\%$ at (905 °C, 215 V/cm), which is followed by a rebound to

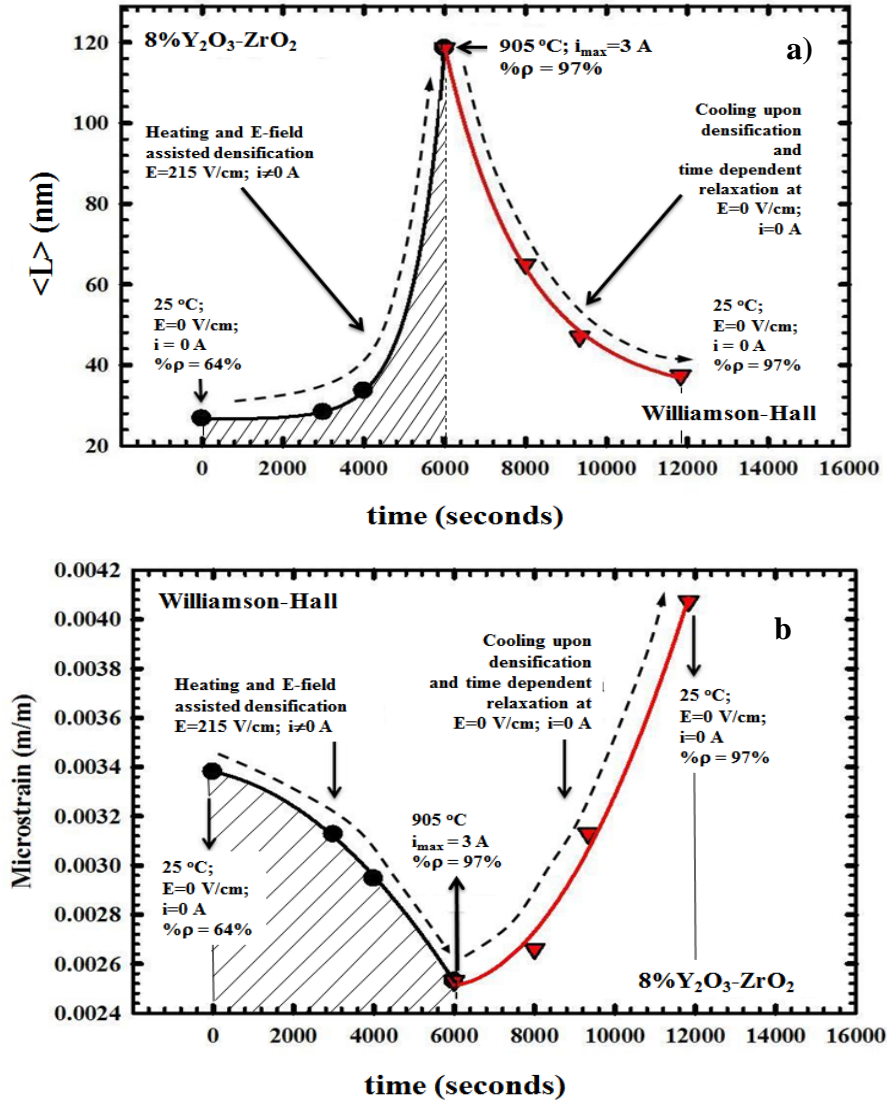


Figure 5.24 The time evolution of the isotropic average Williamson-Hall a) crystallite size, and b) microstrain in the flash densification of 8% $\text{Y}_2\text{O}_3\text{-ZrO}_2$.

0.41% at RT upon cooling under zero applied electric field (see Figure 5.24). The $\text{Y}_2\text{O}_3\text{-ZrO}_2$ system has tetragonal unit cell symmetry [10] which suggests that the crystallite size and microstrain may indeed exhibit anisotropy. The modified Williamson-Hall

crystallite size and microstrain analysis used, on the other hand, represents isotropic averages which precludes the analysis of the said anisotropy. Hence, the parameterized Warren-Averbach method was brought to bear as the second and main method of attack, and applied it on the (101) and (110) reflections to monitor the evolution of the coherently diffracting domain size [78, 79] (CDDS; $\langle L_{hkl} \rangle$), d-spacing variation [78, 79] $\langle u_{101} \rangle$ (DSV; $\langle u_{hkl} \rangle$), and the anisotropy thereto appertaining. In so doing, we were also able to verify the findings of the Williamson-Hall analysis as well. The (101) and (110) peaks were fitted with a pseudo-Voigt profile shape function from which the peak width (β) and the so-called mixing parameter (η) was obtained. The Lorentzian (β_L) and Gaussian (β_G) contributions to the measured β was obtained from equation 3.7 and 3.8. The $\langle L_{hkl} \rangle$ and $\langle u_{hkl} \rangle$ was computed from the Scherrer equation and the expression for microstrain which we produce for continuity. Here, the primes on β_L and β_G represent the peak widths that were corrected for instrumental broadening following Ref. [78] and using a LaB6 standard. Figure 5.25 depicts the variation of $\langle L_{101} \rangle$ and $\langle L_{110} \rangle$ of the Y_2O_3 - ZrO_2 system as a function of time in the presence of superposed thermal and electric fields (0-6000 s) and thermal field alone (6000-12000 s).

At (RT, $E=0$ V/cm), the $\langle L_{101} \rangle$ is ~ 32 nm and $\langle L_{110} \rangle$ is ~ 21 nm, which increase to 88 nm and 128 nm at (905 °C, 215 V/cm), respectively. The anisotropy is most pronounced at 905 °C, i.e. $[\langle L_{101} \rangle : \langle L_{110} \rangle] \sim 3/2$ at which point the density of the system reached 97% as reported earlier[10]. Upon removing the electric field and letting the system to cool to RT, a time-dependent relaxation of $\langle L_{101} \rangle$ and $\langle L_{110} \rangle$ back to their original state is observed within experimental scatter (see Figure 5.25a). On the other hand, the $\langle u_{101} \rangle$ and $\langle u_{110} \rangle$ decrease from 0.72% and 0.64% at (RT, $E=0$ V/cm) to

0.44% and 0.52% at (905 °C, 215 V/cm), respectively, as depicted in Figure 5.25b. The anisotropy $\{\langle u_{101} \rangle : \langle u_{110} \rangle\}$ is ~ 1.15 at (RT, $E=0$ V/cm), which decreases to ~ 0.85 at (905 °C, 215 V/cm). Upon removing the electric field and letting the system to cool to

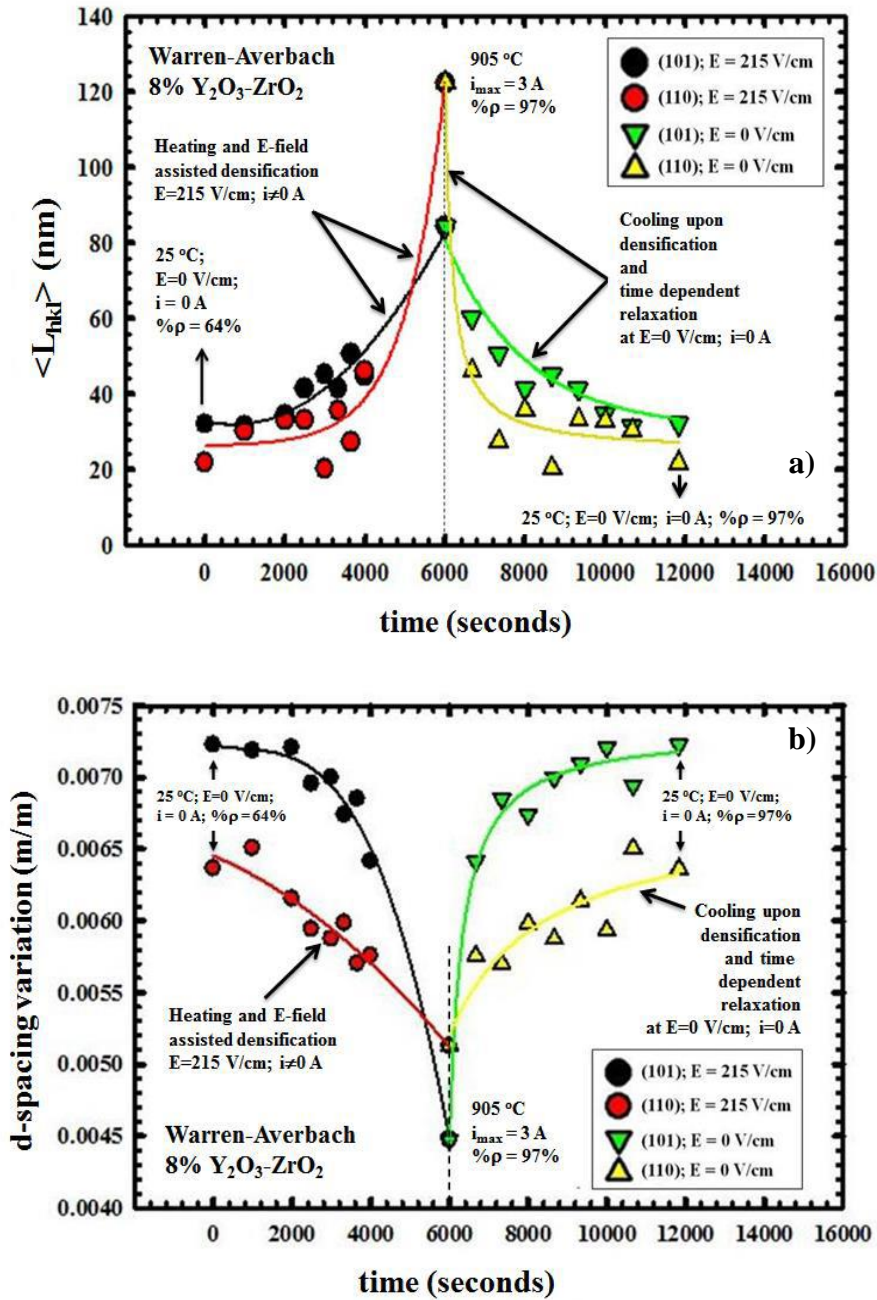


Figure 5.25 Time dependence of the anisotropic (101) and (110) Warren-Averbach a) coherently diffracting domain size, and b) d-spacing variation in the flash densification of 8% Y₂O₃-ZrO₂.

RT, a time-dependent recovery of the ($\langle u_{101} \rangle$, $\langle u_{110} \rangle$) back to their original state is observed within experimental scatter (see Figure 5.25b). According to the Warren-Averbach formalism, the CDDS is the characteristic length of the defect-free region in the [hkl] along which it is measured in a crystalline solid exhibiting finite size broadening. [78-80] Implicitly and as per the said formalism, the CDDS also represents the mean separation between defects or defect clusters in the [hkl] along which it is measured with no specific reference to the type of crystalline defects responsible for such broadening unless [35] there is plausible a priori knowledge of the dominant defect(s). The upper limit for CDDS measurement by x-ray diffractometry is ~150 nm, which is also the limiting value of the mean separation of defects and defect clusters that can be measured by x-ray diffractometry [68,79]. On the other hand, the d-spacing variation (DSV; a.k.a. microstrain) is due to localized (nonuniform) chemical and structural perturbations arising from phenomena such as chemical composition fluctuations, strain field around solute atoms, vacancies and their clusters, dislocations, stacking faults to name a few [80]. It follows from the preceding elaboration that the observed abrupt and reversible changes in CDDS and DSV are manifestations of abrupt and reversible changes in defect processes during the time evolution of densification in 8YSZ under superimposed thermal and electrical fields (see Figure 5.24, 5.25). Specifically, the data in hand shows the applied field increases the separation between defects or defect clusters in the vicinity of 905 °C due to the applied field, as evidenced by the increase in CDDS, and the higher the temperature the larger the spacing between them. Meanwhile, the local perturbations caused by defect or defect clusters are suppressed by the applied field, as evidenced by the decrease in DSV, and the higher the temperature the smaller the local

perturbations. One can attribute such changes in CDDS and DSV to the interaction of the applied electric field with defects or defect clusters in the ZrO_2 structure because they are otherwise completely absent over the temperature range of interest when no field is imposed. In what follows, we shall examine the salient defect processes and their ramifications in the context of ZrO_2 crystallo-chemistry.

The system of interest is a polycrystalline ceramic oxide (ZrO_2) accommodating an acceptor dopant (Y^{3+}) on the Zr^{4+} site of the cubic fluorite structure, where charge neutrality is maintained by oxygen vacancies (Vo) per $[(\text{Zr}_{1-x}\text{Y}_x)\text{O}_2 - (x/2)(\text{Vo})_{x/2}]$ and oxygen vacancy clusters[61]. Ionic conduction and mass transport in 8YSZ is governed by the ambipolar migration [10] of oxygen vacancies under an applied field [99, 100]. However, oxygen vacancy depletion in the immediate vicinity of grain boundaries is known to give rise to back-to-back Schottky barriers in 8YSZ, hindering oxygen transport through grain boundaries up to temperatures as high as 600 °C with no applied electric field [100]. The space charge region has been reported to vary from 1-7 nm in thickness which increases with decreasing grain and/or particle size [99]. Appreciable oxygen vacancy transport is observed in this system at temperatures exceeding 800 °C regardless of the mechanism of transport, i.e. bulk vs. grain boundary, and densification over 95% is observed in particulate systems ($\leq 1\text{ }\mu\text{m}$ average particle size) for $>1400\text{ }^\circ\text{C}$ and > 60 minutes in the absence of an applied electric field[11, 13]. As shown by Akdoğan et al. [10], the densification temperature is decreased by $\sim 500\text{ }^\circ\text{C}$ and the densification time is reduced by one order of magnitude when an electric field $> 200\text{ V/cm}$ is applied. No appreciable joule heating during flash densification in the vicinity of $905\text{ }^\circ\text{C}$ (time frame is too short) due to the applied electric field ($\Delta\Psi$) is observed [10].

Hence, we postulate the sole effect of $\Delta\Psi$ in a solid electrolyte such as 8YSZ to be the enhancement of the chemical potential for (μ_v) as per ;

$$\mu_v = \mu^* + qF\Psi \quad (5.1)$$

where;

$$\mu^* \sim \mu^0 + RT\ln(C_v) \quad (5.2)$$

μ^0 , standard chemical potential; μ^* chemical potential due to vacancy concentration C_v ; T temperature; R , gas constant; q , charge; F , the Faraday constant and Ψ , electrical potential. As such, the thermodynamic driving force for ambipolar diffusion of oxygen vacancies is increased by $qF\Psi$ the ramifications of which should be, in principle, a decrease in densification temperature –an experimental fact which this study has shown [10]. As is well known, densification in a particulate system requires a finite mass flux across particle-particle contacts to cause necking and eventual elimination of pore space between particles [4]. In the case of the 8YSZ particulate system, the mass flux needed for densification pertains to the diffusion of oxygen vacancies [99] under applied simultaneous electric and thermal fields. Following the foregoing line of reasoning, we propose the following kinetic model which consists of two steps in series: i) Diffusion of oxygen vacancies to particle-particle contacts, and ii) tunneling through the Schottky barriers at particle-particle contacts, where the applied electric field is the driving force for both processes. Here, step (i) represents the pile-up of oxygen vacancies against the Schottky barriers at particle-particle contacts which is essentially the redistribution of oxygen vacancies from the interior of the particle to the particle subsurface. Under such circumstances the mean separation between oxygen vacancies or

vacancy clusters has to increase and become approximately commensurate with the physical particle size. For instance, the (101) CDDS at 905 °C is ~128 nm which compares favorably (so does the Williamson-Hall crystallite size) with the ~250 nm physical size of the particle. As discussed extensively by Goff et al. [61] oxygen vacancies actually form clusters in 8YSZ. Therefore, it is most probable that the CDDS reported in this study represents the mean separation of oxygen clusters. Indeed, the DSV data supports the vacancy cluster hypothesis because the magnitude of the applied field in the vicinity of the flash densification temperature seems to be sufficient to induce dissociation of oxygen vacancies reducing the local perturbation thereby as evidenced by the decrease in DSV at 905 °C. Upon removal of the electric field and cooling down to room temperature, the vacancies repartition between the bulk of the particle and the space charge layer, and cluster to assume their original disordered state to attain thermodynamic stability.

5.2.3. Electric Field Effect on Sintered Specimens

In this experimental study, effects of superimposed thermal and electric field on sintered 8% yttria doped zirconia (8YSZ) samples which are flash sintered sample (FS900) at 900 °C and sinter forged sample (SF1400) at 1400 °C, resulted particle size of 250 nm and 1 μ m, and density of $\sim \geq 97$ % and, $\sim \geq 99$ % respectively, was studied under 100 V/cm dc electric field and 12 °C/min heating rate, using time-resolved in-situ high temperature energy dispersive x-ray diffractometry with a polychromatic 200 keV synchrotron probe [84]. As seen Figure 4.2 (HS graph) both samples, in separate experiments, are placed into HS enclosure which is mounted on the positioning stage (see Figure 3.2) and exposed to the beam. The GV is carefully placed on the body center of

the specimen. The temperature and leakage current of the specimen are monitored. X-ray spectra are collected every 2 sec until densification was complete as soon as the temperature reached 600 °C. The described experiment resulted in the collection of 2300 x-ray spectra. Diffraction data were also collected at RT before, immediately after and at RT after densification [84].

Figure 5.26 depicts the fracture surfaces of the FS900 and SF1400 specimens after the in-situ EDXRD experiment. The FS900 sample (see Figure 5.26a), which was sintered at 900 °C, shows a mono disperse average grain size of ~200 nm. Since the grain size of the FS900 sample after flash sintering was also ~200 nm, one concludes that no grain growth has taken place under the application of a 100 V/cm electric field in conjunction with a nonisothermal annealing process at 20 °C/min heating rate up to 700 °C. On the other hand, the SF1400 sample (see Figure 5.26b), which was initially sinter forged at 1400 °C, exhibits massive grain size (~1000-3000 nm) and indeed a bimodal grain size distribution. Since the grain size and grain size distribution of the SF1400 sample after sinter forging was also massive (~1000-3000 nm) and bimodal, respectively, we, again, conclude that no grain growth has taken place under the application of a 100 V/cm electric field in conjunction with a nonisothermal annealing process at 20 °C/min heating rate up to 700 °C. Furthermore, no liquid phase formation was observed in either the microstructure of FS900 and SF1400 samples after the said nonisothermal annealing under the said applied electric field.

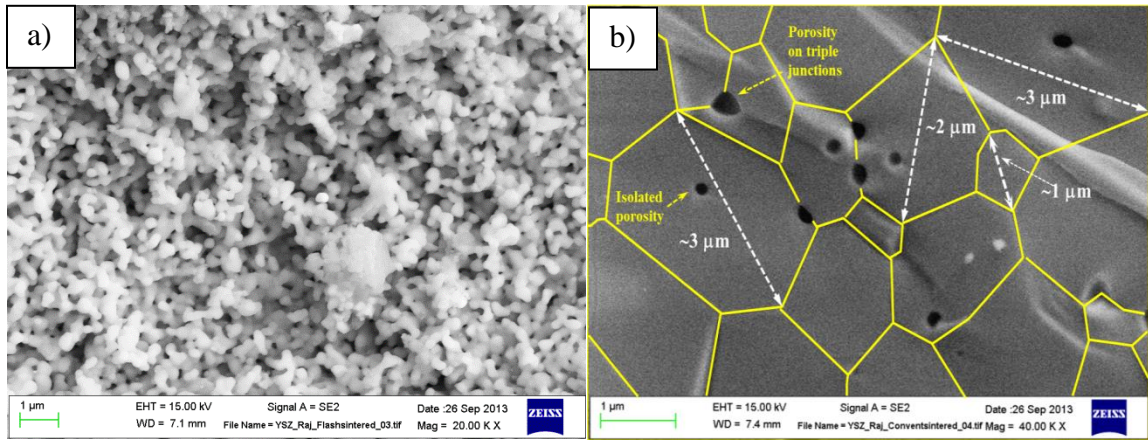


Figure 5.26 SEM images of a) Flash sintered at 900 °C, and b) Sinter forged at 1400 °C samples [84].

It follows from the SEM analysis of the in situ EDXRD experiment that the superposition of an electric field (100 V/cm) and a thermal field (20 °C/min from RT-700 °C) produces no observable phenomena such as additional densification or grain growth both of which are diffusion controlled processes from a thermokinetics perspective [10, 84].

Figure 5.27 shows the variation of the tetragonal unit cell in FS900 and SF1400 samples with time when they are heated with a constant heating rate of 20 °C/min to 700 °C while maintaining an electric field magnitude of 100 V/cm on them in the parallel plate capacitor geometry. As shown in Figure 5.27, one observes a monotonic increase in unit cell volume up to 600 °C which is due to thermal expansion. A simple linear regression yields a volumetric thermal expansion coefficient (α_v) of $3.04 \times 10^{-6} \text{ } ^\circ\text{C}^{-1}$ from which one obtains the linear expansion coefficient (α_L) as $1.01 \times 10^{-6} \text{ } ^\circ\text{C}^{-1}$ using the binomial approximation, $\alpha_v \approx 3\alpha_L$.

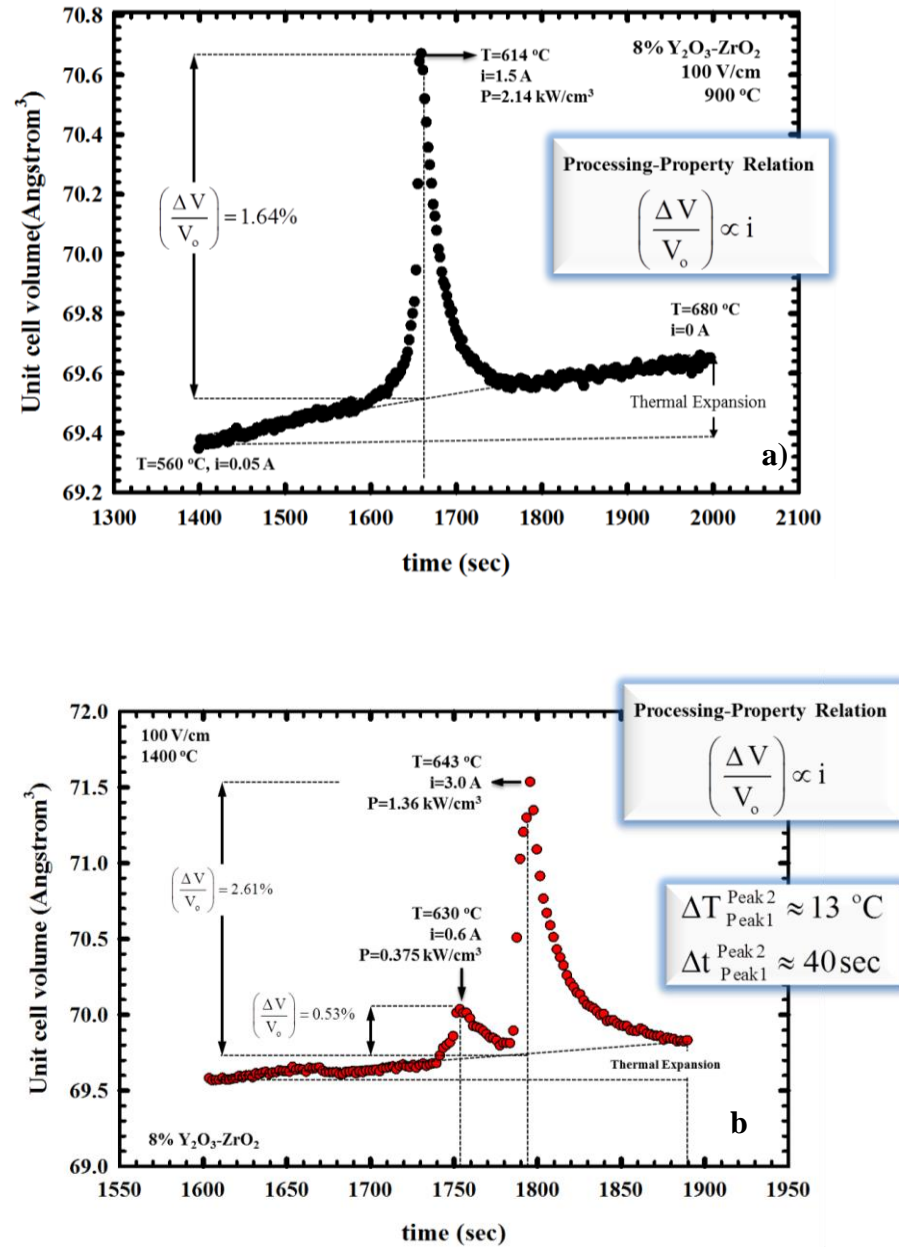


Figure 5.27 Unit cell variation of a) Flash sintered sample at 900 °C, and b) Sinter forged sample at 1400 °C [84].

The said temperature marks the onset of a precipitous tetragonal unit cell expansion. The unit cell expansion in the FS900 sample reaches a maximum value of 1.64% at 614 °C in 20 seconds where the instantaneous volumetric power absorption is 2.14 kW/cm³ (maximum instantaneous current draw is 1.5 Amperes). No discernible temperature

increase due to current draw was observed during the ascent to 614 °C. At 614 °C and $i_{\max}=1.5$ Amp the current was cut off and the system was left to relax while being heated at 20 °C/min. The unit cell relaxation in the FS900 sample under zero current took place 100 seconds and reached the baseline which corresponds to pure thermal expansion. On the other hand, two singularities in the unit cell volume of the SF1400 sample were observed. The first (minor) singularity occurs at 630 °C at which point the current draw peaks at 0.6 A which results current draw and 0.53% volumetric expansion, and the second and major singularity occurs at 643 °C with 3.0 amp current draw and 2.41% volumetric expansion at the tetragonal unit cell.

A closer look at the ramp up to max expansion for both samples shows clear viscoelastic response during current draw from zero to max values as shown in Figure 5.28a. For all samples, initially, unit cell expansion due to thermal field was observed. This is followed by a steep increase in current draw that reaches the maximum volumetric expansion. The timeframe for the observed anomalous behavior is 20 sec for FS900 and 25 sec for SF1400. That is to say, the volumetric expansion is time dependent and hence anelastic. All samples also exhibit anelastic relaxation under zero field once flash sintering is complete as depicted in Fig. 5.28b. This process takes place ~120 seconds.

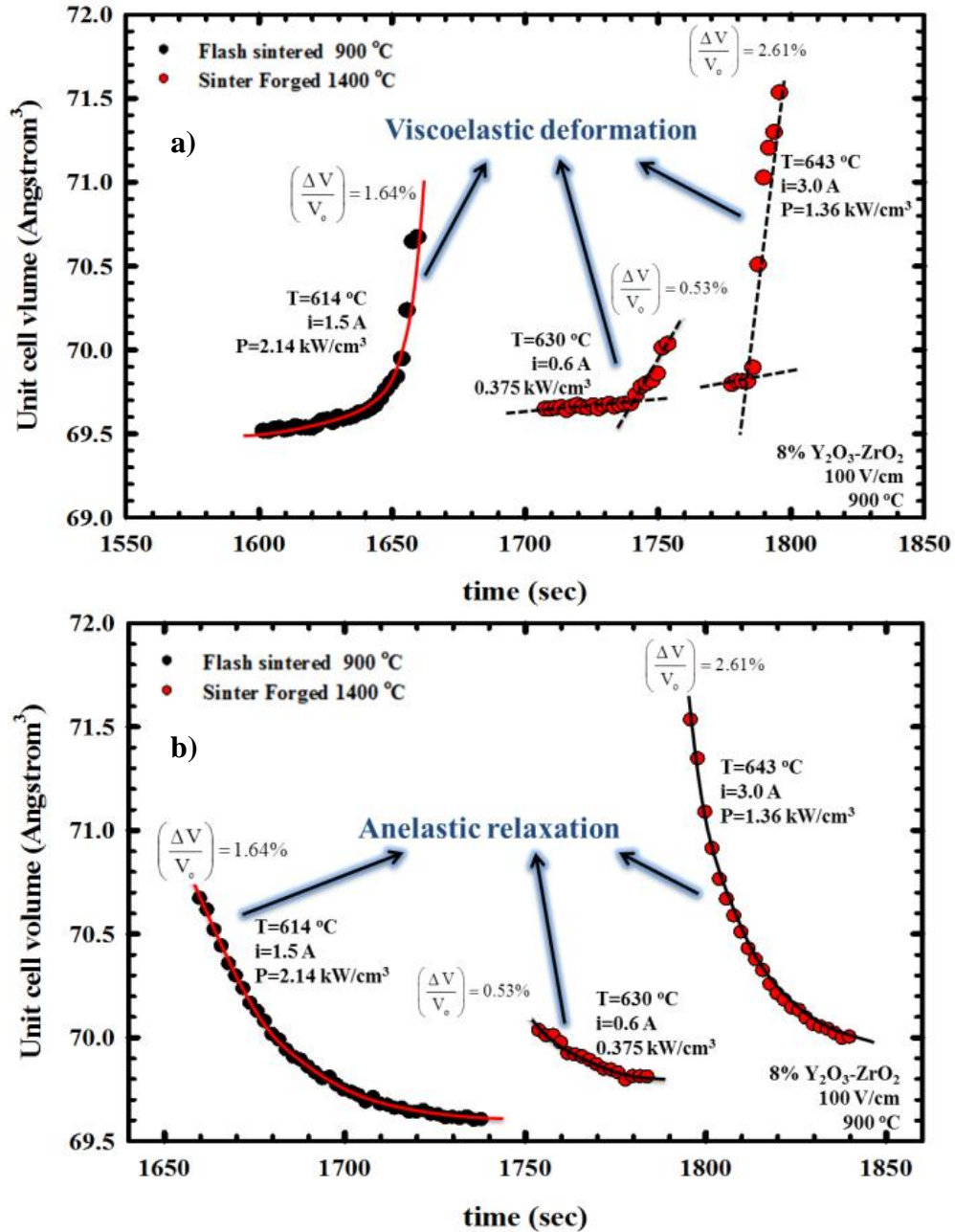


Figure 5.28 Volumetric a) viscoelastic deformation and b) anelastic relaxation at unit cell for FS900 and SF1400 samples.

The variation of interplanar spacing with time at RT's before and after flash sintering, and at the temperatures when current draw occurs, is shown in Figure 5.29. The linear expansion, observed with 1.5 amp current draw at 614 °C (see Figure 5.29 a), is

about 1.13 % which includes the expansion due to thermal field. As shown Figure 5.29 b, the shift of the (100) peak is 0.72 % from RT to 630 °C with 0.6 A, and 1.43% expansion at 643 °C with 3 amp. In both cases, there is no discernible residual strains left after the thermal cycle is complete as can be verified by comparing the spectra for the before and after traces at RT.

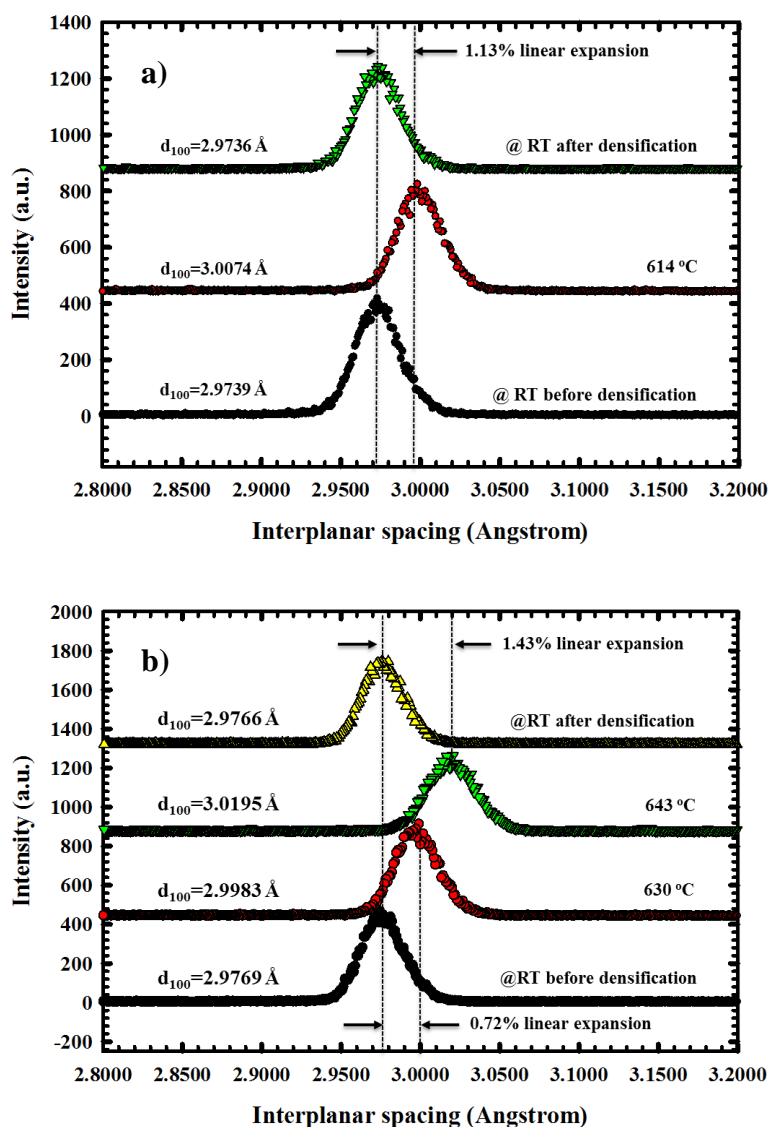


Figure 5.29 X-ray spectra at room temperature before and flash densification for a) FS900 sample and b) SF1400 sample.

Figure 5.30 presents the variation peak (112) with time for both systems. The lack of any distinctive behavior of the FWHM indicates that no defect process can be discerned once densification has occurred previously. The system's governing defects are oxygen vacancies, but, since no discernible behavior is observed, we assert that electronic behavior and mass transport phenomena are decoupled after densification process while they are not in flash sintering of particulate matter.

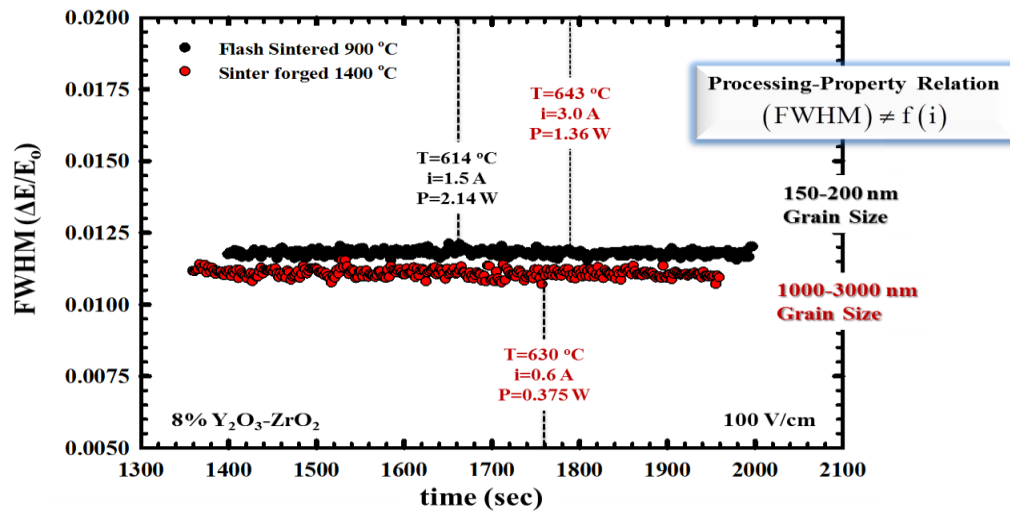


Figure 5.30 FWHM behavior as a function of time during flash sintering [84].

Burst mode densification or flash sintering in ionic conductor oxides reduce the sintering temperature and keep the grain size small [10, 35-39]. The abnormal and instantaneous current draw is clearly linked to the precipitous densification of the system of interest over a narrow temperature and in very short periods of time [10-13, 35-39]. Joule heating was proposed as a simple explanation to explain flash sintering phenomena [10, 35-39]. But a close look suggests otherwise. In general, sintering of this solid state electrolyte requires 1-2 hours at 1400-1600 °C [10, 35-39]. However, according to recent

study based on black body radiation, it is known that joule heating due to current flow in flash sintering is not the root cause of the observed ultrafast densification [10, 94]. Most importantly, sintering within the timeframes observed in this study require the temperature to border the melting temperature of the material. Hence, the Joule heating hypothesis is a very weak one [86, 88, 89].

6. Conclusion

In this two pronged study, the effects of pressure and electric field on the MgO- Y_2O_3 and Y_2O_3 - ZrO_2 systems were studied, respectively. Due to the high temporal resolution of high energy EDXRD, it was possible to measure crystallochemical changes accompanying the combined effects of temperature and pressure, or temperature and electric field that is otherwise not possible with conventional experimental methods, including Bragg-Brentano diffraction. In so doing, some very fundamental discoveries were made that challenge our current understanding of solids in general and ceramic oxides in particular.

The findings of the high pressure studies reveal the following:

(1) Conventional criterion for solid solubility such as electronegativity, valence and ionic size has validity at low pressure only. As the Y^{3+} solubility on Mg^{2+} sites have shown, when the system is forced to high metastability, one can induce solid solubility. Pressure induced dissolution of Y^{3+} in MgO may be considered spontaneous under ultrahigh pressures. However, the metastability is retained at room temperature and 1 atmosphere which suggests that the phase separation kinetics is very sluggish not only at low temperatures but also at low pressures.

(2) The observed 4-phase coexistence in the MgO- Y_2O_3 system shows that pressure induced allotropic transformations, which are displacive phase transitions, can be stabilized at room temperature as well. What is peculiar is that there is essentially no temperature effect on the pressure induced phase transitions as shown in the phase equilibria at 1000 °C which is identical to that at room temperature. While the small

particle/grain size seems to play a role in mediating the phase transitions, dedicated studies are needed to reveal finite size effects.

(3) The most important outcome of the high pressure work is the fact that high pressure provides for fertile ground in the synthesis of microstructures that is not attainable by utilizing thermal activation alone.

The findings of the electric field assisted sintering (flash sintering and/or burst mode densification) studies reveal the following:

(1) There is a densification method which precedes electric field assisted methods that rely on Joule heating (a steady state phenomenon). This densification method is called flash sintering and/or burst mode densification which is a transient state phenomenon.

(2) Burst mode densification takes place at typically 60% of the normal sintering temperature. Yet, its most striking feature is the ultralow sintering times as low as 5-10 seconds which is at least 1 order of magnitude lower than any competing fast sintering method such as spark plasma sintering.

(3) Beginning with the onset of the flash sintering temperature up to the flash sintering temperature, the system is under nonequilibrium conditions as there is charge flow through it. This, in turn, should be considered as a transient perturbation to the charge distribution in the unit cell. Hence, consideration of equilibrium properties such as thermal expansion and elastic strains should be refrained upon.

(4) The observed increase in mass transport could very well be due to the increase in unit cell dimensions. An increase in oxygen vacancy diffusivity (the rate limiting

species) can be possible either by a reduction in the activation energy for oxygen diffusion or by a current dependent increase in the pre-exponential factor, or possible both. The changes in the pre-exponential factor and/or the activation energy should be due to the observed lattice expansion; i.e. diffusivity should be much higher in an open structure.

(5) The drastic reduction in sintering time with decreasing sintering temperature – normally two mutually exclusive factors- suggest that densification is due to electrochemical forces in addition to the conventional driving forces such as excess surface energy due to small particle size as well compositional gradients in defect concentration and such.

This study has claimed some uncharted territory by bringing to bear in situ ultrahigh energy EDXRD in the study of temperature, pressure and electric field effects with unprecedented temporal resolution. This, indeed, shows the importance of probes with which real processing conditions can be simulated and analyzed as exemplified by ultrahigh energy EDXRD. Therefore, a natural extension of this study would be to carry out electrical measurements such as impedance spectroscopy during flash sintering while collecting X-ray data so that a full quantitative description of interface and bulk phenomena can be provided.

REFERENCES

1. J. K. MacKenzie and R. Shuttleworth, *Proc. Phys. Soc.*, B 62, 833 (1949).
2. W. D. Kingery and M. Berg, *J. Appl. Phys.* 26, 1205 (1955).
3. J. E. Burke and J. H. Alexander, *Sintering; Treatise on Solid State Chemistry* (Edited by N.B. Hannay, Plenum Press, New York, 1976).
4. R. L. Coble, *J. Appl. Phys.* 32, 793 (1961).
5. A. P. Greenough, *Nature* 166, 904 (1950).
6. G. C. Kuczynski, *Acta Metall.* 4(1), 58 (1956).
7. E. K. Akdoğan, İ. Şavklıyıldız, B. Berke, Z. Zhong, L. Wang, and T. Tsakalakos *Appl. Phys. Lett.* 99, 141915 (2011).
8. E. K. Akdoğan, İ. Şavklıyıldız, B. Berke, Z. Zhong, L. Wang, D. Weidner, M. C. Croft, and T. Tsakalakos, *J. Appl. Phys.* 111, 053506 (2012).
9. İ. Şavklıyıldız, E. K. Akdoğan, Z. Zhong, L. Wang, D. Weidner, M. C. Croft, and T. Tsakalakos, *J. Appl. Phys.* 113, 203520 (2013).
10. E. K. Akdoğan, İ. Şavklıyıldız, H. Biçer, W. Paxton, F. Toksoy, Z. Zhong and T. Tsakalakos *J. Appl. Phys.* 113, 233503 (2013).
11. R. Raj, M. Cologna, and J. S. C. Francis, *J. Am. Ceram. Soc.* 94(7), 1941 (2011).
12. M. Cologna, A. L. G. Prette, and R. Raj, *J. Am. Ceram. Soc.* 94(2), 316 (2011).
13. T. B. Holland, U. Anselmi-Tamburini, and A. K. Mukherjee, *Scripta Materialia* 69(2), 117 (2013).
14. R. M. German, *Crit. Rev. Solid State Mater Sci.* 35, 263 (2010).
15. T. S. Duffy, R. J. Hemley, and H.K. Mao, *Phys. Rev. Lett.* 74(8), 1371 (1995).
16. D. C. Harris, *Materials for IR Windows and Domes*, SPIE Press Monographs Vol. PM70, edited by D. C. Harris (SPIE, Bellingham, WA, 1999), pp. 17–22.
17. T. Stefanik, R. Gentilman, P. Hogan, *Materials for IR Windows and Domes*, *Proc. of SPIE* Vol. 6545, 65450A, (2007).
18. A. Krell, G. M. Baur, and C. Dahne, *Proceedings of SPIE* 5078, 199-207 (2003).

19. D. Jiang, A. Mukherjee, Proc. of SPIE Vol. 7030 703007, (2008).
20. B. H. Kear, R. Sadangi, V. Shukla, T. Stefanik, and R. Gentilman, Proc. of SPIE 5786, 227-233 (2005).
21. A. B. Belonoshko, S. Arapan, R. Martonak, and A. Rosengren, Phys. Rev. B 81, 054110 (2010).
22. L. Wang, W. Yang, Y. Ding, Y. Ren, S. Xiao, B. Liu, S. V. Sinogeikin, Y. Meng, D. J. Gostzola, G. Shen, R. J. Hemley, W. L. Mao, and H. Mao, Phys. Rev. Lett. 105, 095701 (2007).
23. L. Wang, Y. Pan, Y. Ding, W. Yang, W. L. Mao, S. V. Sinogeikin, Y. Meng, G. Shen, and H. Mao, Appl. Phys. Lett. 94, 061921 (2009).
24. Y. Xu, Z. Gu, AND W. Y. Ching, Phys. Rev. B 56 , 23, (1997).
25. D. Jiang, A. Mukherjee, J. Am. Ceram. Soc., 93 [3] 769–773 (2010).
26. A. Krell, P. Blank, H. W. Ma, T. Hutzler, M. P. B. van Bruggen, and R. Apetz, J. Am. Ceram. Soc., 86 [1] 12–8 (2003).
27. R. Apetz and M. P. B. van Bruggen, J. Am. Ceram. Soc., 86 [3] 480–6 (2003).
28. G. Skandan, C. M. Foster, H. Frase, M. N. Ali, J. C. Parker, H. Hahn, *Nanostruct. Mater.* 1 (4), 313-322 (1992).
29. W. Krauss, R. Birringer, *Nanostruct. Mater.* 9 (1-8), 109-112 (1997).
30. American Ceramic Society, National Institute of Standards and Technology. *Phase Equilibrium Diagram Database 3.1.0*. Wiley-Blackwell, Malden, MA, 2003.
31. Z. A. Munir, U. Anselmi-Tamburini, M. Ohyanagi, J Mater. Sci. 41, 763 – 777 (2006).
32. J. S. C. Francis, M. Cologna, R. Raj, J. Eur. Ceram. Soc. 32 (2012) 3129–3136.
33. R. Orru, R. Licheri, A. M. Locci, and A. C. Giacomo-Cao, Mater. Sci. Eng. R 63, 127 (2009).
34. S. Grasso, C. Hu, G. Maizza, B. Nam Kim, and Y. Sakka, J. Am. Ceram. Soc. 94(5), 1405 (2011).
35. M. Cologna, B. Rashkova, and R. Raj, J. Am. Ceram. Soc. 93(11), 3556 (2010).

36. R. Muccillo, E.N.S. Muccillo, J. Eur. Ceram. Soc. 33 (2013) 515–520.
37. M. Cologna, J. S. C. Francis, and R. Raj, J. Eur. Ceram. Soc. 31, 2827 (2011).
38. M. Cologna and R. Raj, J. Am. Ceram. Soc. 94(2), 391–395 (2011).
39. J. S. C. Francis and R. Raj, J. Am. Ceram. Soc. 95(1), 138 (2012).
40. M. N. Rahaman, Ceramic Processing and Sintering, 2nd ed. (CRC Press, New York, 2003).
41. A. R. Von Hippel, Dielectrics and Waves (Artech House, Norwood, MA, 1955).
42. J. Zhu, M.S.M. Mujeebur Rahuman, J.G. van Ommen, L. Lefferts, Applied Catalysis A259, (2004), 95–100.
43. Jianjun Zhu, Jan G. van Ommen, Arie Knoester, Leon Lefferts, Journal of Catalysis 230, (2005), 291–300.
44. Q. Minh, J. Am. Ceram. Soc. 76 [3], 563-88 (1993).
45. E.C. Subbarao, “Science and Technology of Zirconia”, Advances in Ceramics, Vol. 3. Edited by A. H. Heuer and L. W. Hobbs. (The American Ceramic Society, Columbus, Ohio, 1981).
46. C.T. Grain, J. Am. Ceram. Soc. 50 (1967) 288.
47. F.F. Lange, J. Am. Ceram. Soc. 61 (1978) 85.
48. R. W. G. Wyckoff, *Crystal Structures* (Interscience, New York, 1963), Vol. 1.
49. G. Teufer, Acta Crystallogr. 15, 1187 (1962).
50. M. Yoshimura, Am. Ceram. Soc. Bull., 67, 1950, (1998).
51. M. Wilson, U. Schönberger, M. W. Finnis, Phys. Rev. B. 54, 9146-9161 (1996).
52. D.L. Porter, A.H. Heuer, J. Am. Ceram. Soc. 62 (1979) 298.
53. T.W. Coyle, W.S. Coblenz, B.A. Bender, Am. Ceram. Soc. Bull. 62 (1983) 966.
54. J.G. Duh, H.T. Dai, W.Y. Hsu, J. Mater. Sci. 23 (1988) 2786.

55. D.K. Hohnke, in: P. Vashishta, J.N. Mundy, G.K. Shenoy (Eds.), *Fast Ion Transport in Solids*. Elsevier, North Holland, pp. 669–672, (1979).
56. T.K. Gupta, J.H. Bechtold, R.C. Kuznickie, L.H. Cadoff, B.R. Rossing, *J. Mater. Sci.* 12 (1977) 2421.
57. M. Yashima, H. Takanhashi, K. Ohtake, T. Hirose, M. Kakihana, H. Arashi, M. J. Yoshimura, *J. Am. Ceram. Soc.* 57, 289, (1996).
58. B. H. O'Connor and T. M. Valentine, *Acta Crystallogr., Sect. B: Struct. Crystallogr. Cryst. Chem.* 25, 2140, (1969).
59. J.-H. Lee, S.M. Yoon, B.-K. Kim, J. Kim, H.-W. Lee, H.-S. Song, *Solid State Ionics* 144 (2001) 175–184.
60. S.-M. Ho, *Mater. Sci. Eng.* (1982), 54, 23.
61. J. P. Goff, W. Hayes, S. Hull, M. T. Hutchings and K. N. Clausen, *Phys. Rev. B*, (1999), 59, 14202.
62. J. E. Bauerle and J. Hrizo, *J. Phys. Chem. Solids*, (1969), 30, 565.
63. Y. Suzuki, T. Takahashi and N. Nagae, *Solid State Ionics*, (1981), 3(4), 483.
64. F.F. Lange, G.L. Dunlop, B.I. David, *J. Am. Ceram. Soc.* 69 (1986) 237.
65. T. Sato, S. Ohtaki, T. Endo, M. Shimida, *J. Mater. Sci. Lett.* 5 (1986) 1140.
66. C. León, M. L. Lucia, and J. Santamaria, *Phys. Rev. B* 55, 882, (1997).
67. J. D. Solier, I. Cachadiña, and A. Dominguez-Rodriguez, *Phys. Rev. B* 48, 3704 (1993).
68. H. P. Klug and L. E. Alexander, *X-Ray Diffraction Procedures: For Polycrystalline and Amorphous Materials* (John Wiley & Sons, New York, 1974).
69. A. Guinier, *X-ray Diffraction: In Crystals, Imperfect Crystals, and Amorphous Bodies* (Dover Publications, Mineola, NY, 1994).

70. B.E. Warren, X-ray Diffraction, (Dover Publications, Inc., New York, 1990).
71. C. Kittel, Introduction to Solid State Physics, (John Wiley & Sons, New York, 2005).
72. M. Croft, I. Zakharchenko, Z. Zhong, Y. Gurlak, J. Hastings, J. Hu, R. Holtz, M. DaSilva, and T. Tsakalakos, J. Appl. Phys. 92, 578 (2002).
73. M. Croft, V. Shukla, E. K. Akdoğan, N. Jisrawi, Z. Zhong, R. Sadangi, A. Ignatov, L. Balarinni, K. Horvath, and T. Tsakalakos, J. Appl. Phys. 105, 093505 (2009).
74. L. Li, D. J. Weidner, J. Chen, M. T. Vaughan, M. Davis, and W. B. Durham, J. Appl. Phys. 95(12), 8357–8365 (2004).
75. Y. Wang, W. B. Durham, I. C. Getting, and D. J. Weidner, Rev. Sci. Instrum. 74, 3002 (2003); B. S. Li, J. Kung, and R. C. Liebermann, Phys. Earth Planet. Inter. 143, 559–574 (2004).
76. R.A. Young, Ed., *The Rietveld Method* (Oxford University Press, New York, 1993).
77. G.K William, W. H. Hall, Acta Metallurgica, 1, 22 (1953).
78. B.E. Warren, B.L. Averbach, J. Appl. Phys., 23, 497 (1952).
79. M. A. Krivoglaz, *Theory of X-ray and Thermal Neutron Scattering by Real Crystals* (Plenum Press, New York, 1969).
80. E. J. Mittemeijer, U. Welzel, Z. Kristallogr., 223, 552-560 (2008).
81. Y. Wang, J. Zhang, L. L. Daemen, Z. Lin, Y. Zhao, and L. Wang, Phys. Rev. B 78, 224106 (2008).
82. L. Li, D. J. Weidner, J. Chen, M. T. Vaughan, M. Davis, and W. B. Durham, J. Appl. Phys. 95(12), 8357 (2004).
83. Y. Wang, W. B. Durham, I. C. Getting, and D. J. Weidner, Rev. Sci. Instrum. 74, 3002 (2003).
84. İ. Şavklıyıldız, E. K. Akdoğan, H. Biçer, T. E. Özdemir, Z. Zhong and T. Tsakalakos, J. Am. Ceram. Soc. (in review) (2015).

85. K. Jin, X. Li, Q. Wu, H. Geng, L. Cai, X. Zhou, and F. Jing, *J. Appl. Phys.* 107, 113518 (2010).
86. R. A. Swalin, *Thermodynamics of Solids* (John Wiley & Sons, New York, 1972).
87. Powder diffraction file numbers used in this study are as follows (M:MgO, Y₂O₃:Y): cubic-M 97-30-9863, cubic-Y 97-001-6394, hexagonal-Y 97-016-0204, and monoclinic-Y 97-016-0219. Data from the International Centre for Diffraction Data (2011).
88. H. B. Callen, *Thermodynamics and an Introduction to Thermostatistics*, 2nd ed. (John Wiley & Sons, New York, 1985).
89. C. H. P. Lupis, *Thermodynamics of Materials* (Elsevier, New York, 1983).
90. R. D. Shannon, *Acta Crystallogr. A* 32, 751 (1976).
91. Q. S. Wang and N. A. W. Holzwarth, *Phys. Rev. B* 41, 3211 (1990).
92. R. E. Eitel, C. A. Randall, T. R. Shrout, P. W. Rehrig, W. Hackenberger, and S.-E. Park, *Jpn. J. Appl. Phys.* 40, 5999 (2001).
93. J. A. Stratton, *Electromagnetic Theory*, 1st ed. (McGraw-Hill, New York, 1941).
94. W. D. Kingery, H. K. Bowen, and D. R. Uhlmann, *Introduction to Ceramics*, 2nd ed. (Wiley, New York, 1976).
95. L. D. Landau, L. P. Pitaevskii, E. M. Lifshitz, and A. M. Kosevich, *Theory of Elasticity*, 3rd ed., *Theoretical Physics Vol. 7* (Butterworth-Heinemann, Oxford, UK, 1986).
96. R. P. Feynman, R. B. Leighton, and M. Sands, *The Feynman Lectures on Physics: Electromagnetism and Matter* (Addison-Wesley Publishing Co., Reading, MA, 1964), Vol. II.
97. Rishi Raj, *J. Am. Ceram. Soc.* 32 (2012) 2293–2301.
98. T. Ungar, H. Mughrabi, M. Wilkens, and A. Hilscher, *Phil. Mag. A* 64(2), 495 (1991).

99. O. J. Dura, M.A. Lopez de la Torre, L. Vasquez, J. Chaboy, R. Boada, A. Rivera-Calzada, J. Santamaria, C. Leon, Phys. Rev. B 81, 184301 (2010).
100. X. Guo, Scripta Materialia, 65, 96-101 (2011).